TEMPERATURE-DEPENDENT ELECTROCHEMICAL IMPEDANCE SPECTROSCOPY (EIS) OF LITHIUM THIONYL CHLORIDE AND LI-ION BATTERIES

A DISSERTATION SUBMITTED TO

THE GRADUATE SCHOOL OF ENGINEERING AND SCIENCE

OF BILKENT UNIVERSITY

IN PARTIAL FULFILLMENT OF THE REQUIREMENTS FOR

THE DEGREE OF

DOCTOR OF PHILOSOPHY

IN

CHEMISTRY

By

Gökberk Katırcı

May 2024

Temperature-dependent Electrochemical Impedance Spectroscopy (EIS) of Lithium Thionyl Chloride and Li-ion Batteries
By Gökberk Katırcı
May 2024

We certify that we have read this dissertation and that in our opinion it is fully adequate, in scope and in quality, as a dissertation for the degree of Doctor of Philosophy.

Burak Ülgüt(Advisor)

Emrah Özensoy

Damla Eroğlu Pala

Şefik Süzer

Mark Orazem

Approved for the Graduate School of Engineering and Science:

Orhan Arıkan
Director of the Graduate School

ABSTRACT

TEMPERATURE-DEPENDENT ELECTROCHEMICAL IMPEDANCE SPECTROSCOPY (EIS) OF LITHIUM THIONYL CHLORIDE AND LI-ION BATTERIES

Gökberk Katırcı
Ph.D. in Chemistry
Advisor: Burak Ülgüt
May 2024

Batteries are one of the most researched and developed energy storage systems in recent years due to their utilization in portable and mobile devices. Therefore, operando and in-situ characterization of batteries should be properly performed to understand the electrochemical processes. For this purpose, Electrochemical impedance spectroscopy (EIS) and its complementary techniques have been utilized in this thesis to investigate various electrochemical systems.

This thesis starts with a detailed electrochemistry review, which is necessary for understanding the discussions. Then, experimental and technical details regarding the measurement practices are presented. The initial transient occurrence with a simplified Randles cell and using both experimental and simulation data eventually shows that the initial transients are observed in every measurement and simulation scenario. Even with the real-life dummy cells made of resistors and capacitors, the initial transients are present and cannot be eliminated completely. Thereafter, the temperature-dependent EIS studies are presented, including the temperature-dependent EIS of symmetric and complete cells as well as the spiral/bobbin architectures of Lithium Thionyl Chloride ($Li/SOCl_2$) batteries. The evaluation and comparison of the impedance response of different cell geometries and architectures with the consideration of Arrhenius relations. The Arrhenius

relations are utilized for the determination of the activation energies of electrochemical processes detected by EIS. Thus, the result concludes that the activation energies are dependent on the SoC of the battery, temperature, and chemistry, and these parameters are investigated in detail. Following, another study with similar chemistry, $Li/SOCl_2/SO_2Cl_2$ batteries, is investigated in terms of EIS and Non-linear Harmonic Analysis (NHA), which shows the relation between the Kramers Kronig (KK) compatibility and NHA based on this cell chemistry. The proper way of measuring this chemistry is also presented with experimental details, which necessitates changing the impedance parameters to acquire linear and reproducible results. Lastly, in the appendix, my personal interest in electric guitar pickups is investigated, and the single-coil and humbucker structures are compared in terms of their impedance responses.

Keywords: impedance spectroscopy, metallic lithium anodes, non-linear harmonic analysis, Li-ion battery.

ÖZET

LITYUM TIYONÜL KLORUR VE LI-ION PILLERIN SICAKLIGA BAGLI ELEKTROKIMYASAL EMPEDANS SPEKTROSKOPISI INCELENMESI

Gökberk Katırcı
Kimya, Doktora
Tez Danışmanı: Burak Ülgüt
Mayıs 2024

Piller ya da bataryalar, geçtiğimiz yıllarda sıkça araştırılan ve geliştirilen, taşınabilir ve portatif cihazlarda kullanılan enerji depolama sistemleridir. Velhasıl, pillere kullanım sırasında ve çalışır vaziyette teşhis ve tanı konulması azami derecede önem arz etmektedir. Dolayısıyla, deneysiz bir elektrokimya düşünülemez; ilm-i kimya, tecrübelerle müsbet bir sahta nüfuz eder. Bu vesile ile, elinizdeki tezde Elektrokimyasal Empedans Spectroskopisi'ne (EIS) dayanan yöntemler kullanılmıştır. Elektrokimyasal Empedans Spektroskopisi, yerinde tetkik yapabilen, tahrip edici etkisi bulunmayan bir teşhis ve tanımlama yöntemidir.

Bu tez, içerisinde anlatılan tartışmaların ve konuların iyice anlaşılmasını sağlamak amacıyla, elektrokimya alanının etraflıca bir tekrarı ile başlamaktadır. Buna müteakip, yapılan ölçüm ve cihazlara ait deneysel ve teknik detayları içeren bir kısım bulunmaktadır. Devamındaki kısımlarda ise, çoğunlukla evveliyatında yayınlanmış çalışmaları içeren bölümler bulunmaktadır. Bu bölümler ilk olarak empedans ölçümlerinin başlangıçlarda geçici olarak görünen bir deneysel olguyu ele almaktadir. Bu olayda hem deneysel veri hem de teorik simülasyonlardan faydalanılmıştır. Neticede, bu olgunun her daim mevcut olduğunu ve farklı senaryolarda dahi engellenemeyeceğinin sonucuna varılmıştır. Bunu takip eden kısımda ise sıcaklığa bağlı empedans deneyleri ve sonuçlarına yer verilmiştir. Bu çalışmalar mütenasip (simetrik) ve tam çalışır piller ile lityum

tiyonül klorür pilleri ile icra edilmiştir. Bu sonuçta pillerde gerçekleşen ve empedans spektroskopisi ile ölçülebilen işlemlerin aktivasyon enerjileri Arrhenius denklemleri kullanılarak hesaplanmıştır. Ayrıca, farklı hücre mimarilerinden de yararlanılarak elektrokimyasal işlemler birbirlerinden ayrılmış ve incelenmiştir. Böylelikle, pillerin içerisinde gerçekleşen farklı olaylar incelenmiştir.Bir sonraki bölümde ise, yine benzer bir kimyada olan lityum tiyonül klörür ve sülfürül klorür pillerinin empedans ve doğrusal olmayan harmonik incelenmeleri anlatılmıştır. Bu bölüm Kramers Kronig (KK) ve doğrusal olmayan harniklerin analizinin birbirleri ile uyumlu sonuçlar verdiğini ve birbirlerini desteklerini kanıtlamıştır. Son olarak, appendix kısmında yer alan çalışmada şahsi ilgi alanım olan elektro gitar manyetiklerini inceleyen ve farklı türlerinin empedanslarını kıyaslayan kısa bir bölüm bulunmaktadır.

Anahtar sözcükler: empedans spektroskopisi, metalik Lityum anot, dogrusal olmayan harmoniklerin analizi, Li-ion pil.

Acknowledgement

First of all, I would like to thank my advisor, Assoc. Prof. Burak Ülgüt for his guidance and mentorship throughout my graduate studies. Similarly, I am grateful to my thesis progression committee members, Prof. Emrah Özensoy and Assoc. Prof. Damla Eroğlu Pala, Prof. Şefik Süzer, and Prof. Mark Orazem for their valuable feedback on this thesis. In addition, I would like to thank all of the professors in the Chemistry Department and other institutes' professors whose classes I have taken throughout my studies in Bilkent.

I want to mention the groupmates I have worked with over the years. In Ülgüt group, I would like to thank Dr. Mohammed Zabara, Fazlı Eren Civan, Ezgi Sevgen, Fatma Altuğ, Gözde Karaoğlu, and Eylül Ergün. In the Özensoy group, I would like to thank Dr. Yusuf Koçak, Bartu Karakurt, Ayşe Erdali, Dr. Zafer Say, Kerem Emre Ercan, Merve Kurt, Elnaz Ebrahimi, Ahmet Arda Türk, Kaan Karaca, and Zeynep Kap.

I would like to dedicate this thesis to my grandparents, *Selma and Hamdi Türkmen*, who passed away in the third year of my doctorate studies. Additionally, I would like to sincerely thank my brother *Berkay*, my mother *Jülide*, and my cute little brother *Layka*. Lastly, I would like to say thank you and congratulate my dear wife, *Assel*, for being there for me and her doctoral studies.

Furthermore, I would like to mention the people who inspired and helped me to achieve academic and non-academic success up to the date. First, thank you to all my teachers throughout the years, from F.S.M. primary school, Vefa Lisesi, professors of Boğaziçi University Chemistry Department, and many more that I cannot recall. An honorable mention and thanks to my high school history

teacher, İsmail Aktaş, for showing us the academic world and its values. Similarly, I would like to thank Prof. Ufuk Önen of Bilkent COMD for his books and discussions that taught me how to explore sound and its technologies, contributing to this thesis's electric guitar pickup section in the appendix. As a part of the non-academic aspect of my life in Bilkent, I would like to thank my tennis teacher/coach, Halil Karakaya, my long-time tennis buddy Dr. Çağatay Alpay, and my other tennis buddies in Bilkent. These people are (in no specific order) Furkan Kızılyel, Zana Özdemir, Emre Uyan, Burak Ateşkan, Eren Özdilkural, Onur Ataç, and Alihan Deşir. Tennis is the hobby that I developed a huge interest in during my doctorate studies.

Contents

1 Introduction **2**

1.1 Batteries, Electrochemistry, and Motivation 2

1.2 Fundamentals of Electrochemistry 5

1.2.1 Electrochemical Energy Storage Systems 5

1.2.2 Basic Concepts 6

1.2.3 Half reactions, Electrodes & Electrolytes 10

1.2.4 Double-layer Capacitance 13

1.2.5 Charge and Mass Transfer Processes 15

1.2.6 Properties of Thionyl Chloride 20

1.2.7 Solid-Electrolyte Interface (SEI) 22

1.3 EIS Fundamentals 24

1.4 Equivalent Circuits 30

1.5 Visualization: Bode & Nyquist plots 33

1.6 Organization of the Thesis 41

2 Methodology & Experimental Setup **42**

2.1 Equivalent Circuit Fitting 42

2.2 Constant Phase Element (CPE) and Effective Capacitance 44

2.3 Non-linear Harmonic Analysis (NHA) 46

2.4 Conclusions 53

3 Initial Transients **54**

3.1 Introduction 54

3.2 Results and Discussion 57

3.3 Conclusions 63

4 Temperature-Dependent EIS **65**

4.1 Theory and Background 65

4.2 Results and Discussion 68

4.2.1 Symmetric Cell Configuration 68

4.2.2 Aging and Cycling Estimations based on Symmetric Cells 74

4.2.3 Bobbin vs. Spiral Li/$SOCl_2$ Batteries 85

4.3 Conclusions 100

5 EIS Measurements of Tekcell $SOCl_2$ and SO_2Cl_2 batteries **102**

5.1 Introduction 102

5.2 Experimental Section 103

5.3 Results 105

5.3.1 EIS Measurement Results 105

5.3.2 Equivalent Circuit Fits 107

5.3.3 KK Compatibility, Residuals, and Non-linear Harmonic Analysis (NHA) 108

5.4 Conclusions 119

6 Conclusions **121**

Conclusions **121**

6.1 Future Recommendations 123

Appendix **124**

6.1.1 Measurement Parameters 125

6.2 Results and Discussion 128

List of Publications **151**

List of Figures

1.1 Power densities of primary lithium batteries in terms of W/kg (upper) and W/L (lower). Source: [1]. 4

1.2 Basic components of an Electrochemical Energy Storage System. . 7

1.3 Schematic of four probe measurements between the potentiostat and the battery. In our measurements, we either purchase factory-made connection leads or spot-weld thin nickel strips. 12

1.4 Potential distribution over the electrode, double layer, and bulk electrolyte (a) and illustration of ionic species on a charged metal electrode(b). E_m is the potential of the bulk metal electrode, and E_S is the potential of the bulk electrolyte. 14

1.5 Illustration of Butler-Volmer model for a broad potential interval (a) and zoomed-in view of no charge region (b). 18

1.6 2D representation of the LiCl SEI layer on metallic Li anode, which occurs in Li/$SOCl_2$ batteries. 23

1.7 The time-domain profiles of the excitation and response signals (a) with a 90°phase (ϕ). The Lissajous plot is a common way of representing these two signals (b). The green dot is the actual measurement point on the Lissajous ellipse, which generally rotates in a clockwise direction (when the excitation signal initially increases). 26

1.8 Schematic of a simplified Randles' circuit. 31

1.9 Bode (upper) and Nyquist (lower) plots of 100 Ω resistor. 36

1.10 Bode (left) and Nyquist (right) plots of a simple one mF capacitor. 37

1.11 Bode (left) and Nyquist (right) plots of an RC unit with 10 kΩ resistance and 2.2 μF capacitor. The discontinuity of phase angle at 100 Hz is due to a filter engaging/disengaging at lower/higher frequencies. It is an instrumental artifact and is not significant in our discussions. 38

1.12 Nyquist plot of an RC element with a constant phase element (CPE), with different α values. 39

1.13 Bode (left) and Nyquist (right) plots of a Randles' cell. The series and parallel resistances are 10 kΩ, and the capacitor is 2.2 μF. . . 40

2.1 Illustration of harvesting the information regarding the NHA analysis. The process is done using Python code. 46

3.1 Non-linear harmonic analysis of a Li/$SOCl_2$ battery with initial transients being shown in the blue rectangle. 55

3.2 Two dummy cells that were used in this research. *This figure is reproduced with permission.* 57

3.3 Response Harmonics of two dummy cells. *This figure is reproduced with permission.* 58

3.4 Simulated Response Harmonics of two dummy cells. The real-life measurement includes noise, which can also be simulated by adding a 0.1% noise level to the main signal amplitude. *This figure is reproduced with permission.* 59

3.5 Simulated results without discarding any cycles, with a total of five cycles. *This figure is reproduced with permission.* 62
3.6 Simulated harmonics by measuring 30 cycles and discarding the first 24 of them. *This figure is reproduced with permission.* 63

4.1 Impedance responses of symmetric Li/Li cells with different electrolyte compositions at 15°C (a) and 55°C (b). 71
4.2 Impedance responses of battery-type cells with different electrolyte compositions at 15°C (a) and 55°C (b). 72
4.3 Nyquist plot of EC-DMC battery-type cell and the semicircle representations. 73
4.4 Nyquist plots of symmetric pristine (a) and aged (b) samples, and battery-type pristine (c) and aged (d) cells. 74
4.5 Illustration of the cell architectures with different electrode configurations. 75
4.6 The Nyquist plots of each cell architecture at -20°C. The plots belong to Li-Li (top), Li-LFP (middle), and LFP-LFP (bottom) cells. 76
4.7 1/RC values of battery-type (a) and symmetric architectures (c). Similarly, the effective capacitances of battery-type (b) and symmetric cells (d) are plotted over the temperature range between -20°C and 60°C. 77
4.8 Nyquist plots of Li-LFP (pristine) battery-type cells at different temperatures. 79
4.9 Arrhenius plots of battery-type (Full Cell) and Symmetric configurations at pristine and aged states. 80

4.10 Bode plot of a battery-type cell at different cycle counts. This plot was taken with permission from our collaborators. 82

4.11 1/RC and capacity values of a battery-type sample measured with 0.5C for 60 cycles. 83

4.12 Illustration of ion and electron movements in the bobbin (a) and spiral (b) geometries of $Li/SOCl_2$ batteries. 86

4.13 The EIS response of spiral and bobbin architectures at the same experimental conditions. 87

4.14 Nyquist plots of spiral (upper) and bobbin (lower) types of $Li/SOCl_2$ batteries. Additionally, the equivalent circuit fit model for both chemistries, alongside the region, indicates the transmission line for the bobbin type. 89

4.15 The equivalent circuit elements of a $Li/SOCl_2$ battery. Each R-CPE element represents a process, and they are positioned in the place of the process. 90

4.16 Temperature-dependent EIS results of the bobbin (a) and spiral (b) types at various temperatures. 92

4.17 Effective capacitances of electrochemical processes in the bobbin (a) and spiral (c) type of $Li/SOCl_2$ batteries. Similarly, the 1/RC values of bobbin (b) and spiral (d) geometries are plotted. 94

4.18 Arrhenius plots of different electrochemical processes observed in the EIs of the spiral (right) and bobbin(left) geometries, analyzed at 80% SoC. 96

4.19 Bobbin-type temperature-dependent EIS responses at high (a), middle (c), and low (e) states of charge. Likewise, the spiral responses at high (b), middle (d), and low (f) SoCs are plotted. . . 97

4.20 Arrhenius plots of charge transfer resistance across the SEI for spiral (right) and bobbin (left) geometries at different SoCs. . . . 99

5.1 C-size new 2022 batteries at different states of charge. 105

5.2 D-size new 2022 batteries at different states of charge. *This figure is reproduced with permission.* 106

5.3 Equivalent circuit fits of C-size batteries, all chemistries included. *This figure is reproduced with permission.* 108

5.4 Equivalent circuit fits of C-size batteries, all chemistries included. *This figure is reproduced with permission.* 109

5.5 The equivalent circuit-based NHA of a battery (a), the real-world NHA of the battery with a good KK-fit(b), and a non-KK-compatible NHA result (c). The lower row is a scaled-up view of the fundamental response with a linear y-scale instead of logarithmic. 110

5.6 C-size 85% $SOCl_2$ battery with KK-compatible results at high (a), middle (c), and low (e) SoCs. In the right column, the same states of charges with non-KK-compatible results (b), (d), and (f). 15% $SOCl_2$ battery with KK-compatible results is plotted at high (g) and Low(i) SoCs, whereas (h) and (j) show non-KK-compatible results at the same SoCs. *This figure is reproduced with permission.* 112

5.7 The equivalent circuit of a C-size mixture battery (a), simulated Nyquist plot of the same equivalent circuit (b), simulations of NHA with 3 mA (c), 30 mA (d), 300 mA(e), and 3 A (f) AC amplitudes. *This figure is reproduced with permission.* 114

5.8 Simulation results of the equivalent circuit described in 5.7(a) with a cosine (a) and sine (b) signal. Time-domain data representing the excitation signal and voltage response at the peak frequencies of the harmonics are also plotted alongside the frequency-domain plots. *This figure is reproduced with permission.* 115

5.9 Kramers Kronig residuals of batteries with compatible and non-compatible KK fits. *This figure is reproduced with permission.* . . 117

5.10 Kramers-Kronig residuals with 2 Voigt elements per decade (a) and 9 elements per decade of frequency (b). *This figure is reproduced with permission.* 119

6.1 The experimental components of this research consist of the pickup, a grounded Faraday Cage, a Potentiostat, and a computer. 126

6.2 Equivalent circuit fit for the single coil and humbucker pickups. . 127

6.3 Impedance (upper) and phase angle (lower) spectra of single coil and humbucker pickups from 100 kHz to 1Hz. 128

6.4 The components of the equivalent circuit elements on the impedance response of the most prominent (middle) peak. 131

6.5 Non-linear harmonic analysis of (upper) single coil and (lower) humbucker pickups. 133

List of Tables

4.1 Activation energies of battery-type samples at various cycled states. 80

4.2 Activation energies of Li-Li and LFP-LFP symmetric cells at pristine and aged conditions. 81

5.1 Discharge amounts and DC magnitudes for all batteries. AC magnitude was always 10 mA in all measurements. To save space, only $SOCl_2$ amounts were used to define the battery composition. . . . 104

6.1 Equivalent circuit elements used in the model and their values and errors. Abbreviations used in this table are: E.C.E. is Equivalent Circuit Element and its unit. 132

List of Symbols

F	Faraday constant = 96485 C/mol
T	Absolute temperature in Kelvin (K)
R	Universal gas constant = 8.31446261815324 J/K
η	Overpotential (V)
Q	Charge (C)
M	molar mass (g/mol)
n	number moles of electron
ϵ_0	permittivity of the space = 8.854 x 10^{-12} F/m
R	Resistance (Ω)
S	Siemens ($1/\Omega$)

Chapter 1

Introduction

1.1 Batteries, Electrochemistry, and Motivation

In recent years, energy storage systems have been developed significantly with the advancements in battery technologies. As today's world shifts to renewable energy in many areas, batteries play a critical role in the storage of the produced energy. Moreover, the utilization of batteries in transportation also necessitates the need for battery development. Additionally, the cost of battery-powered applications is becoming more viable and cheaper as the batteries (in terms of manufacturing, raw material cost, production efficiency, etc.) evolve.

Batteries are currently the most popular means of energy storage systems. The first and foremost reason is their portability and integration to a hugely vast array of applications. Additionally, the volumetric and gravimetric energy densities of batteries are relatively high compared to their alternatives, such as internal

combustion engines. Although batteries have less energy density than traditional combustion engines, lack of periodical maintenance and rechargeability are important advantages of battery-powered applications. As a result, the development and optimization processes of battery performance are being undertaken at a significant speed. Furthermore, the low maintenance costs of battery-powered vehicles and devices make them a charming option. As the application area of the batteries can differ largely, so can the chemistry and the size of the battery[1].

Batteries are *broadly* categorized into two sections: primary and secondary batteries. Primary batteries are disposable and single-use batteries and cannot be charged for another cycle of use. The governing electrochemical reactions are irreversible, and attempting to charge these batteries is not recommended due to safety reasons. On the other hand, reversible electrochemical reactions run secondary batteries, and the batteries can be charged and discharged at cycling conditions specified by the manufacturer. Overall, the batteries have different open circuit voltages, energy, and power densities because of their chemical compositions, and they are used in appropriate application fields.

Primary batteries have distinctive advantages over secondary batteries despite being non-rechargeable. The high energy density (in terms of volumetric and gravimetric), longer shelf life ($Li/SOCl_2$ notably), lower manufacturing costs, wider operation temperature range, and overall reliability are the main advantages. Therefore, primary batteries can be found in low-current devices such as detectors, military devices, scientific and research instruments, space-related applications, and disposable products. Among the chemistries of primary batteries, zinc-carbon is the most commonly found type and is used in home/low-current withdrawing electronics due to its low cost. Similarly, alkaline batteries are used

in low-current devices, and they have higher energy density than zinc-carbon batteries. Silver oxide batteries also have moderate energy densities and are mostly used in medical devices. Lastly, thionyl chloride and sulfuryl chloride batteries have high volumetric and gravimetric energy densities, as seen in Figure 1.1.

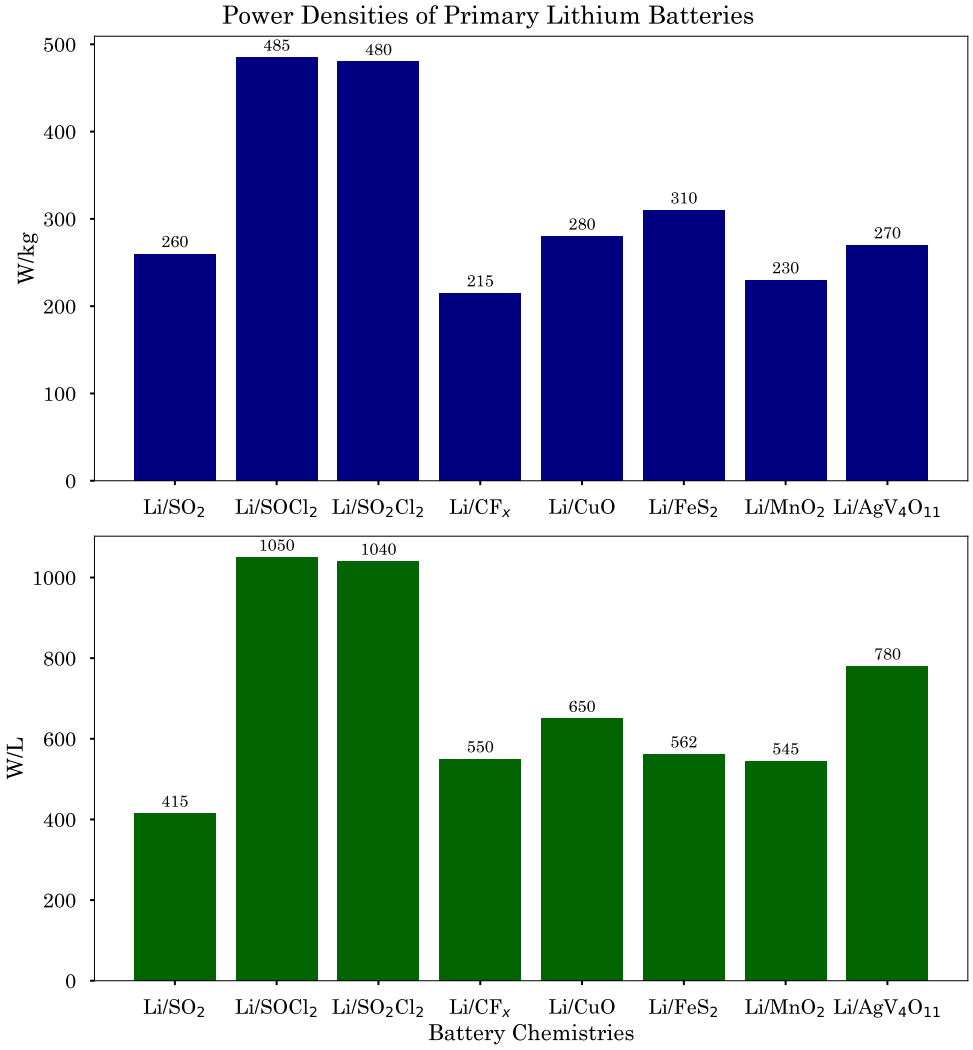

Figure 1.1: Power densities of primary lithium batteries in terms of W/kg (upper) and W/L (lower). Source: [1].

Implementing metallic Li anodes in Li-ion battery technology is the ultimate

goal for achieving maximum gravimetric and volumetric energy densities [2][3]. Limitations for their implementation include the formation of inhomogeneous/-mossy Li and the formation of Li dendrites during charging, which leads to performance and safety concerns [4]. Approaches for employing metallic Lithium without the adverse effects include solid-state electrolytes and with new electrolyte formulations[5][6][7]. Commercialization efforts have been slow due to performance, cost, and scale-up problems.

In this introductory chapter, we will cover the very first fundamentals of electrochemistry and then build our way up to the current research with the batteries. Therefore, the following parts will show the basics of electrochemistry, governing mechanisms, properties, and processes.

1.2 Fundamentals of Electrochemistry

1.2.1 Electrochemical Energy Storage Systems

We shall start by defining the critical and main components of every electrochemical energy storage system. Regardless of chemistry and purpose, they all have four main components. These are anode, cathode, electrolyte, and separator. The energy storage in these components is provided by storing the energy in chemicals and then converting them into electricity by going through redox reactions. Moreover, the redox reactions yield different chemical species and generation of electrons. These electrons circulate throughout the external circuit and provide the energy needed for application. Obviously, a complete electrical contact has to

be present in order to run the electrochemical cell. As we shall investigate later, the connection types and procedures will vary and be used for different purposes.

To begin with, the types of anode and cathode predominantly determine the rechargeability, capacity, power output, and operational conditions. For many battery types and chemistries, these electrode configurations also determine the name of the battery type/name. In this thesis, for instance, we will be discussing metallic Li anodes and porous carbon cathodes, which will be denoted as $Li/SOCl_2$. As a result, the electrode type and configuration are vital for the battery nomenclature.

The other components of an electrochemical cell are the separator and the electrolyte. The main purpose of a separator is to prevent direct physical contact between the electrodes and filter or allow the movement of certain chemical species. The engineering of the separator uses the governing electrochemical reactions, chemicals in the medium, and solute species and their concentrations as inputs. In Figure 1.2, an illustration of a simple electrochemical energy storage system or a battery is given.

1.2.2 Basic Concepts

In this section, we shall investigate the fundamental properties of electrochemical energy systems and cells. These definitions will be extensively used in this thesis, and understanding them is highly critical for conveying the outcomes.

Voltage (V): Also denoted as potential, it is the main contributor to the movement of electrons. Its formal definition is there is work needed for an electron

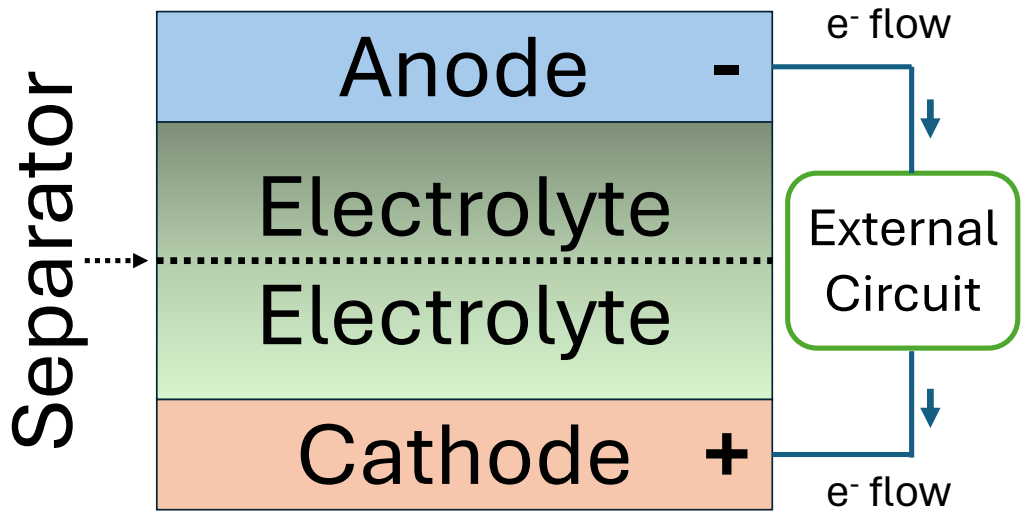

Figure 1.2: Basic components of an Electrochemical Energy Storage System.

to move between two electrodes of the cell. The potential of the cell is directly related to the Gibbs free energy by the following formulation:

$$\Delta G = -nFE \tag{1.1}$$

In this equation, ΔG is the Gibbs free energy change, n is the number of moles of electrons moved through the cell, F is Faraday's constant, and E is the cell voltage. Additionally, the negative sign is present due to the thermodynamic consistency between the two concepts. A spontaneous reaction has a negative ΔG and positive cell potential.

- *OCP (Open Circuit Potential):* is also known as the resting potential, which is observed in an electrochemical cell at the equilibrium state. This equilibrium state can be determined by observing the cell voltage over a few minutes, where the

voltage asymptotes and remains constant after a certain period. This equilibrium state will be discussed in the future and will play a critical role in cell health estimation and calculations.

- η *(Overpotential):* Overpotential is defined as the voltage gap between the theoretically calculated (equilibrium) voltage of the system and the voltage applied at the working electrode. Overpotential is a necessary quantity to utilize energy storage systems, such as batteries, for improvement and efficiency during the operation.

Current (A): is the amount of charge that passes through a single point in a circuit over time. The current is one of the most frequently used terms in this thesis, and its unit is Ampere (A). The formal definition of an Ampere is one Coulomb per second. One Coulomb (of charge) is around 6.24 x 10^{18} electrons.

- *C-rate:* is a commonly used formulation at which current the battery is charged or discharged. For many battery datasheets, different C-rates are given for charging and discharging since these processes have different rates for each process. A mathematical way of describing it would be the following:

$$C - rate = \frac{Current(A)}{NominalCapacity(Ah)} \tag{1.2}$$

As stated in Equation 1.2, C-rate gives an idea about the total charge or discharge duration of a battery at a given current amount. For instance, a 0.5C rate for a 40 Ah battery would require 20 A current withdrawal for 2 hours. The amount of C-rate is directly related to the architecture of the cell, electrode types, chemistry of the electrolyte, and operational conditions.

- *Peak and Continuous Maximum Currents:* The maximum current (or peak current) is defined as the maximum amount of current that a system can provide for a short amount of time that would not degrade or damage the cell. It generally occurs in quick bursts or transient states for a few seconds. It is dependent on the internal resistance or impedance of the system, connection types, capacity of the system, and electrode surface areas. On the other hand, the maximum continuous current is the highest current amount that a cell can provide over a longer period of time without any damage to the cell. It is usually less than the maximum current and related to the cell chemistry, electrode areas, and thermal properties of the cell.

Energy density: This density is identified as the energy stored per unit or per unit mass. It is frequently used in battery data sheets and comparison charts. Gravimetric energy density is generally expressed as Watt-hours per kilogram (Wh/kg), and it is a highly crucial parameter for weight considering applications such as aviation, automobiles, and so on. Similarly, the volumetric energy density is Watt-hours per liter (Wh/L). Consequently, it is vital to consider this property in space-limited, portable mobile device applications.

- *Power density:* This term refers to the rate of energy deliverance per unit volume or mass. Depending on the type of unit, it can be denoted as W/kg or W/L. It is mostly considered in applications where the power requirements are high, and energy densities should be condensed.

- *Capacity (Ah or Wh):* is the amount of energy that can be delivered or supplied by the electrochemical energy storage over a complete charge and discharge cycle. Generally, charge and discharge amounts are almost similar, but in this

thesis, we have discharge capacities reported in related sections in later discussions. While we generally talk about Ah capacities for small-size batteries, Wh or kWh capacities can be used to enlist the capacities of battery packs or modules in cars, airplanes, etc.

State-of-charge (SoC): is a percentage value for representing the remaining or present amount of energy inside a cell. In practice, it is the same value that we encounter on our smartphones, laptops, and other portable devices. Overall, the value represents how much (of percent) energy is being present in the cell with respect to the nominal capacity.

- *Depth-of-Discharge (DoD):* This term is the other half of the SoC value; it is the ratio of withdrawn or used energy divided by the nominal capacity. For instance, 30% SoC indicates 70% DoD. Therefore, these values are commonly used together or interchangeably in technical documentation, reports, and datasheets.

Generally, these definitions and terminology are enough for understanding most of the battery-related research. Further techniques and devices shall be discussed in the second chapter of this thesis.

1.2.3 Half reactions, Electrodes & Electrolytes

A typical redox reaction and an electrochemical reaction can be separated by the reaction medium. A traditional or simpler redox reaction takes place in the same bulky medium as the redox species. On the other hand, an electrochemical reaction has separate places for the reduction (via using the electrons) and oxidation (by extracting the electrons) reactions. These two reactions take place at

different locations or boundaries, usually on the electrodes and electrolytes.

The electrodes, from an electrochemistry point of view, are (usually) solid and conductive components that are in physical contact with a conductive liquid/medium called an electrolyte. Therefore, these two terms are generally used together. Consequently, the whole system is called an electrochemical cell and contains electrode(s), electrolyte, and external circuit components.

The historic and crucial law that governs the electrochemical processes is Faraday's law. It is used in charge/current calculations, material transformation, and electrolysis reactions. It actually has two sections, but a modern interpretation can be written as follows:

$$m = \left(\frac{Q}{nF}\right) M = \left(\frac{it}{nF}\right) M \tag{1.3}$$

In this equation, m is the mass of the substance, which is in grams, M is the molar mass of the substance, i is the current, n is the number of moles of electrons, F is Faraday's constant, and t is the time that passes in seconds. A text related to electrochemistry ought to contain some information regarding Faraday's constant, which is around 96485 Coulomb per mole. It states the amount of charge for the equivalence of a mole and will be used extensively throughout this thesis.

Moreover, the electrode number is an important issue in electrochemical cells. There are different numbers of cells that are built with either two, three, or four electrodes. Two electrode setups are commonly used for measuring simple electrochemical experiments such as CV (cyclic voltammetry), where a sensitive potential measurement is not necessary. When precise control of the potential is

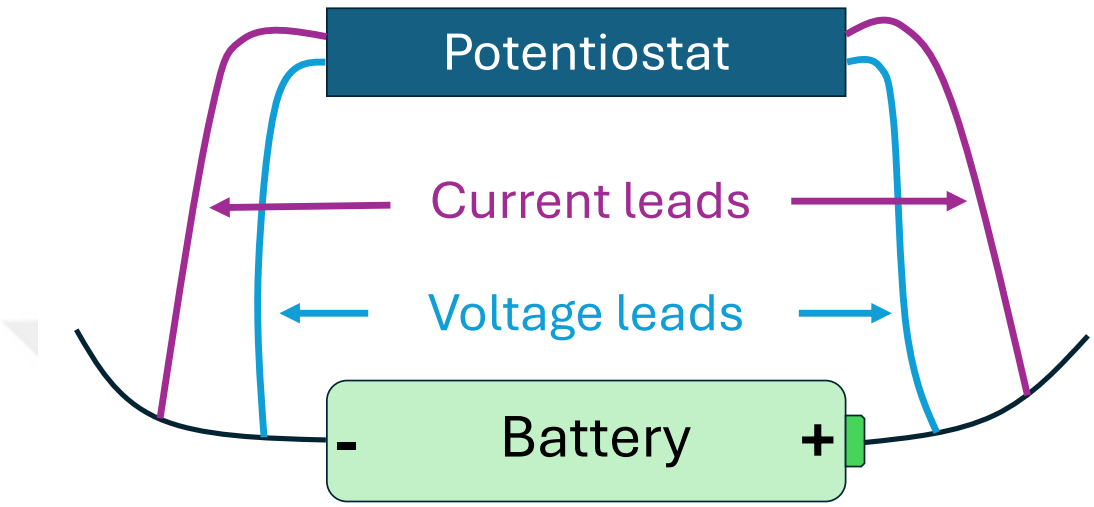

Figure 1.3: Schematic of four probe measurements between the potentiostat and the battery. In our measurements, we either purchase factory-made connection leads or spot-weld thin nickel strips.

required, a three-electrode setup can be used. In this case, the counter electrode enables a pathway for electrons to flow, and a reference electrode is used to measure the voltage between the reference and working electrodes. Lastly, a four-electrode system can even measure more sensitive properties by eliminating the effects such as polarization, high solution resistance, and so on. Throughout the measurements reported in this thesis, all of the measurements are performed with the four-electrode configuration to acquire the most accurate and precise results.

In Figure 1.3, a schematic illustration of our typical battery connection to potentiostats is shown. The voltage is measured between the voltage leads, which are placed right after the battery terminals. Similarly, the current flows between the outer two probes and does not interfere with the voltage measurement. By

utilizing this four-probe setup, measurement accuracy, and precision increase. Since Gamry potentiostats are being used extensively, their specific names can be mentioned: working and working sense electrodes are placed on the positive battery terminal, and they measure current and voltage, respectively. On the other hand, counter and reference probes measure current and voltage, respectively.

1.2.4 Double-layer Capacitance

As we have covered many required points and concepts so far, we shall delve into a classical and fundamental topic in electrochemistry called double-layer capacitance. Essential processes of electrochemistry mostly occur on electrode surfaces and boundaries between the electrodes and electrolytes. The layers form near the boundary due to the movement of charged species in the electrolyte. Consequently, the negatively charged electrode attracts positive ions, and the positively charged electrode attracts negative ions. Therefore, the formed structure is described as the double layer.

On the solid electrode surface, electrons and holes result in negative and positive charging, respectively. On the electrolyte side, a few layers are observed. The innermost layer is called the Helmholtz layer, and it is made of adsorbed molecules or chemical species. Thereafter, the second layer is formed by the solvated molecules, and these two layers are separated by the inner Helmholtz layer. Similarly, the bulk electrolyte and the second or outer Helmholtz layer are separated by the outer Helmholtz layer.

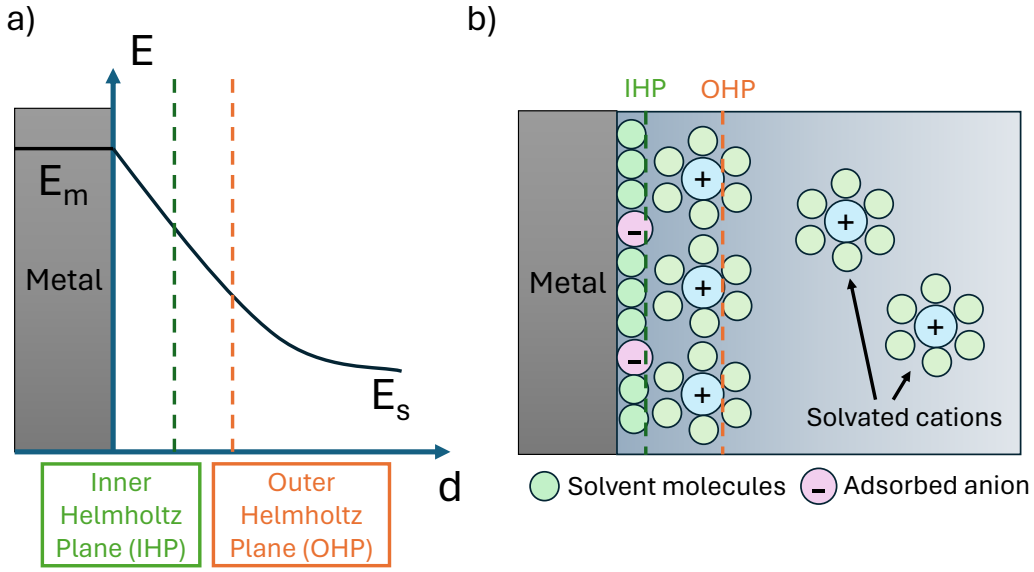

Figure 1.4: Potential distribution over the electrode, double layer, and bulk electrolyte (a) and illustration of ionic species on a charged metal electrode(b). E_m is the potential of the bulk metal electrode, and E_S is the potential of the bulk electrolyte.

As seen in Figure 1.4, the structure of these layers exhibits close planes of oppositely charged species, which eventually form capacitors. Since the distance between them is relatively small, a capacitance value can be calculated and used to describe the nature of this double layer. The generic formula of a capacitor is the following:

$$C = \epsilon_0 \epsilon \frac{A}{d} \tag{1.4}$$

In equation 1.4, it is clearly shown that the capacitance is directly proportional to the surface area (A), the permittivity (ϵ) of the volume between the plates where ϵ_0 is the permittivity of the space, and inversely proportional to the distance

(d) in between. This distance is generally a few Angstroms and does not change drastically. Therefore, the capacitance is more dependent on the surface area of the electrodes. Greater surface areas yield increased capacitance values, such as highly porous carbon electrodes. It should also noted that this capacitance is valid for the Helmholtz model and does not include Guoy-Chapman capacitance[8].

1.2.5 Charge and Mass Transfer Processes

In the context of this thesis, the charge transfer process is investigated as well-defined redox reactions of active materials. These reduction and oxidation reactions are coupled, and overall, they determine the cell voltage according to the principles of the Nernst equation. The Nernst equation can be derived from more fundamental relations as follows:

$$W_{max} = \Delta G = -nFE \tag{1.5}$$

In this statement, the maximum work done by a system can be represented by the Gibbs free energy change and converted into the electrochemical cell voltage. In the previous paragraph, we introduced the coupled redox reactions, and they can be represented by the following equations:

Anodic (oxidation) reaction:

$$aA \rightleftharpoons cC + ne^- \tag{1.6}$$

Cathodic (reduction) reaction:

$$bB + ne^{-} \rightleftharpoons dD \tag{1.7}$$

Overall cell (redox) reaction:

$$aA + bB \rightleftharpoons cC + dD \tag{1.8}$$

Therefore, the rearrangement of the Gibbs energy formula above gives the following formulation:

$$\Delta G = \Delta G^0 + RTln\left(\frac{\alpha_A^a \alpha_B^b}{\alpha_C^c \alpha_D^d}\right) \tag{1.9}$$

In this case, the term ΔG^0 can be found via $\Delta G^0 = -\frac{E^0}{nF}$. Thereafter, the Nernst equation can be easily acquired by dividing both sides by nF in Eq. 1.9:

$$E = E^0 + \frac{RT}{nF} log\left(\frac{\alpha_A^a \alpha_B^b}{\alpha_C^c \alpha_D^d}\right) \tag{1.10}$$

In this equation, F is the Faraday constant, R is the universal gas constant, and n is the number of moles of electrons passing through the cell. The overall cell voltage can be found by utilizing this equation, and due to the logarithm term, the cell voltage does not change significantly until one or more chemical species are consumed. It should be noted that the activities of the chemicals are used in Eq. 1.10; however, in many cases, this can be simplified into the concentrations

in (mol/liter).

Moreover, the amount of current generated in this electrochemical cell is limited by the mass transport of the dissolved species. In this case, the famous Butler-Volmer model or equation is used for modeling and understanding the kinetic processes. This equation explains the reaction rates on the electrode/-electrolyte interfaces and the electron exchange between the dissolved ions in the electrolyte and electrode[9]. The equation is the following:

$$i = i_0[e^{(\frac{\alpha F \eta}{RT})} - e^{(-\frac{(1-\alpha)F\eta}{RT})}] \tag{1.11}$$

In Eq. 1.11, i is the current density in A/cm^2, i_0 is the equilibrium (where the forward and backward reaction rates are equal) current density with the same A/cm^2 unit, α is the reaction coefficient which ranges from 0 to 1 (its value represents the symmetry of the reactions), η is the overpotential in V, R is the universal gas constant, and lastly T is the absolute temperature in Kelvin.

According to Eq. 1.11, the current must increase exponentially as the applied overpotential increases. However, in real-life scenarios, this exponential increase can be observed only at smaller voltage windows, which can be seen in Figure 1.5 (b). The mass-transport processes take over at higher overpotentials and asymptotes as the voltage goes to infinity at both positive and negative voltages. As a result, species cannot move in the electrolyte faster than this transport limit.

Similarly, the charge carriers or electrons face an obstacle at the electrode/-electrolyte interface, which is called charge transfer resistance. This resistance

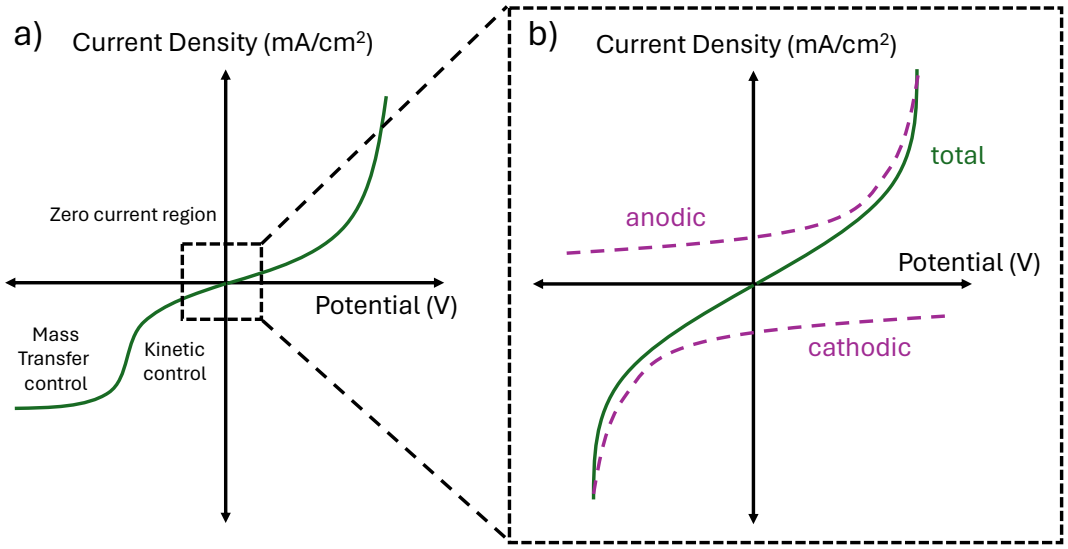

Figure 1.5: Illustration of Butler-Volmer model for a broad potential interval (a) and zoomed-in view of no charge region (b).

is related to the electrode kinetics, activation energies, temperature, and electrode conductivity. When the Butler-Volmer equation is reorganized with small overpotential values and i_0 values, the following statement can be reached:

$$R_{CT}(\Omega) = \frac{RT}{nFi_0} \tag{1.12}$$

This charge transfer resistance will be the main source of discussions, and it is a key parameter in finding the activation energy of the charge transfer processes. In addition, this charge transfer resistance represents an elementary reaction where the process can be investigated via Arrhenius relations. Therefore, the relation with the activation energy can be easily explained via the Arrhenius equation as follows:

$$\frac{1}{R_{CT}} \quad \alpha \quad k = Ae^{-\frac{E_A}{RT}} \tag{1.13}$$

In this equation, k is the rate constant for the charge transfer reaction ($O + e^{-} \rightleftharpoons R$), A is the pre-exponential term, E_A is the activation energy, R is the universal gas constant, and T is the absolute temperature in Kelvin. Consequently, the activation energy can be calculated from the slope of this reaction by plotting 1/T vs. $\ln(1/R_{CT})$. The slope of this Arrhenius plot gives the value of $-\frac{E_A}{R}$. Thereafter, multiplying this slope with -R gives the activation energy in j/mol. This slope would give a large value for most processes, albeit plotting 1000/T vs. $\ln(/R_{CT})$ can give the activation energy in kJ/mol.

Another critical point is the mass transfer inside an electrochemical cell, which occurs via diffusion and migration. Diffusion is due to the concentration gradient inside the electrolyte medium, and migration results from the electric field of electrodes. As a result, two charged planes in parallel structures generate the electric field and cause ions or chemical species' migration.

A simplified 1-D model of diffusion and migration can be written via the Nernst-Planck equation as follows:

$$J(x) = -D\frac{\delta C(x)}{\delta x} - DC\left(\frac{zF}{RT}\right)\left(\frac{\delta \phi(x)}{\delta x}\right) \tag{1.14}$$

In Equation 1.14, *J(x)* is the flux of species at position x, D is the diffusion coefficient, $\frac{\delta C(x)}{\delta x}$ is the concentration gradient at a given position. This first part is the diffusion part, and the rest is about the migration: z is the charge, $\frac{\delta \phi(x)}{\delta x}$ is the

electric field gradient, and F is the Faraday constant. The diffusion coefficient D can be determined and modeled via experimental measurements, such as EIS, CV, or potentiostatic/galvanostatic intermittent titration (PITT/GITT), depending on the electrode and electrolyte composition[10]. These transport processes are important for the understanding of the failure mechanisms of a battery. For instance, in metallic Li batteries, dendrite formation or the loss of active material is directly proportional to the mass transport during the operation. After a certain amount of cycling, Li deposits on the electrodes as *"dead Li"* or *"inactive Li"* and decreases the performance[11].

Although these models and equations can work well with simple cell structures, as we shall see, the batteries have a complex nature due to the additional critical parameters. One of them is the solid electrolyte interface (SEI) that occurs at the electrode/electrolyte boundary.

1.2.6 Properties of Thionyl Chloride

Thionyl chloride ($SOCl_2$) is a colorless, slightly volatile, sour, and sharp-smelling chemical compound. It is used in many battery chemistries throughout this thesis. In organic chemistry textbooks, it is used as a chlorination agent[12]. It is a toxic chemical and, on some occasions, is used as a solvent[13]. It is mainly synthesized by the reaction of sulfur dichloride and sulfur trioxide as follows:

$$SO_3 + SCl_2 \rightarrow SO_2 + SOCl_2 \tag{1.15}$$

In literature, alternative synthesis routes can be found with the following reactions as well[14]:

$$SO_2 + PCl_5 \rightarrow SOCl_2 + POCl_3 \tag{1.16}$$

$$SO_2 + Cl_2 + SCl_2 \rightarrow 2SOCl_2 \tag{1.17}$$

$$SO_2 + COCl_2 \rightarrow SOCl_2 + CO_2 \tag{1.18}$$

Thionyl chloride can easily react with water to form hydrochloric acid and sulfur dioxide gas[15]:

$$SOCl_2 + H_2O \rightarrow HCl + SO_2 \tag{1.19}$$

Lastly, thionyl chloride reacts with metals to produce metal chlorides, sulfur dioxide gas, and, in some cases, chloride compounds[16]:

$$M + SOCl_2 \rightarrow MCl + SO_2 \tag{1.20}$$

The reaction with lithium also produces SO_2 gas and LiCl compound, which forms the stable solid electrolyte interface (SEI) on the metallic Li anode. The formation and stability discussions are in the following section.

1.2.7 Solid-Electrolyte Interface (SEI)

A solid-electrolyte interface (SEI) is a thin and dynamic layer that forms on the electrodes once they are in physical contact with the electrolyte. The driving force for the SEI formation is mostly the electrolyte (redox) reactions with the electrode. Therefore, the SEI materials are some derivatives of the electrolyte species. For instance, in $Li/SOCl_2$ batteries, it is primarily LiCl, which is an ionic Lithium salt. As a result, SEI formation is a naturally occurring process and is affected by the cell chemistry, cycling (or discharge for primary batteries) conditions, and temperature.

Even though the formation processes can change between different cell chemistries, they generally form at the early stages of cell assembly or after a few activation/formation cycles. The SEI layer changes its thickness, morphology, and transfer properties as the batteries are cycled, discharged, and exposed to different temperatures. For many batteries, the SEI is highly temperature dependent, and charge transfer processes across the SEI are informative quantities for the evaluation of the SEI. Therefore, we shall take a closer look at the SEI structure. In Figure 1.6, the LiCl SEI structure on metallic Lithium anode can be seen. The dynamic nature of this specific SEI layer is formed when metallic lithium anode is immersed in $SOCl_2$ electrolyte. In later chapters, this SEI structure will be investigated thoroughly. Similarly, in another study by Markevich et al., SEI formation on metallic Li anode with different organic electrolytes has been investigated[17]. Lastly, Aurbach and co-workers published about the failure mechanisms of metallic Li anodes and Li-containing electrodes with different passivation structures and current rates, which are related to the surface passivation, volume expansion during Li transport, and electrode morphology[18].

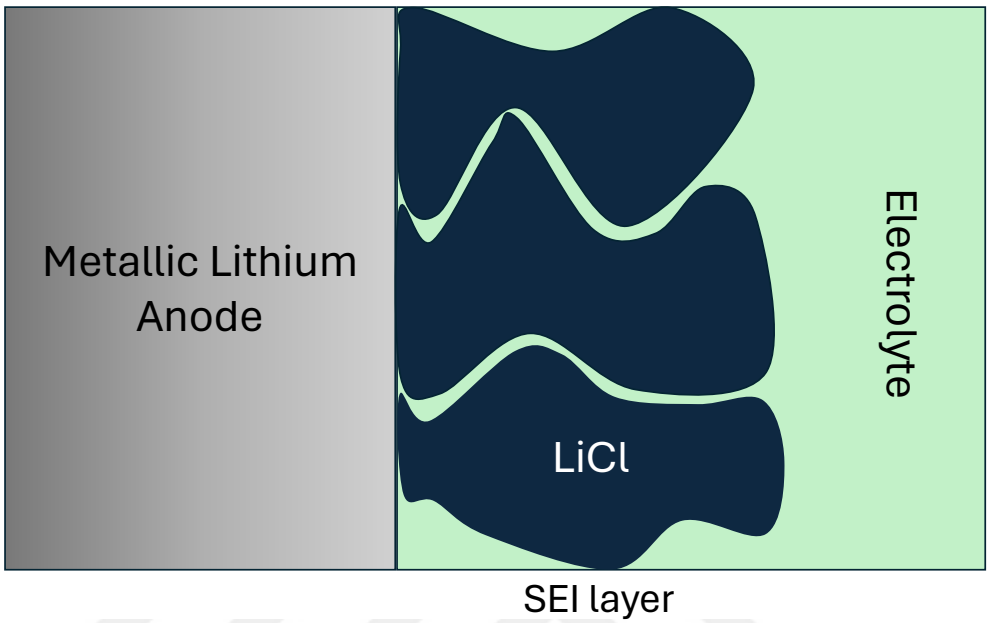

Figure 1.6: 2D representation of the LiCl SEI layer on metallic Li anode, which occurs in Li/$SOCl_2$ batteries.

The SEI is one of the most crucial components in many Li-ion and primary Lithium batteries[19]. The investigations of SEI mainly focus on measurement, modeling, and analysis aspects[20]. The SEI is a kinetic barrier that provides a stable structure, which prevents self-discharge and undesired electrochemical reactions. On the other hand, it needs to transfer Li^+ through the cracks and pores for the battery to function properly. In a study by Aurbach, the SEI formation with metallic Li, lithiated carbon, and transition metal oxide electrodes are thoroughly investigated[21].

1.3 EIS Fundamentals

Electrochemical Impedance Spectroscopy (EIS) is a non-destructive and in-situ electrochemical characterization method[22]. Since its conception in the second half of the 20^{th} century, EIS has been vastly used in corrosion science, semiconductors, sensors, and energy conversion and storage studies[23]. In these fields, EIS provides kinetic, thermodynamic, and transport properties of the investigated electrochemical system independently. The advancement of EIS has a direct correlation with the equipment development used in EIS. These developments increased the sensitivity, accuracy, and reliability of the measurements, making EIS a widely used analytical and diagnostic tool. The transition from analog to digital impedance devices enabled the usage of a wide frequency range, quicker data acquisition, and better data analysis. Additionally, the size of the measurement devices has become smaller over the years, and currently, EIS can be easily performed on-site. Furthermore, the advancements in the software side of EIS provided quick and accurate data evaluation and measurement automation, which reduced human error in the experiments.

EIS measurements are done by special devices designed for this purpose. Briefly, this device generates a sinusoidal excitation signal and measures the voltage response over a wide frequency range. The investigated electrochemical system is connected with a series of electrodes. Four-electrode measurement setup has been explained in Fig. 1.3. Throughout this thesis, four electrode (or probe) measurements are conducted in all battery measurements. By doing so, a four-electrode setup is being applied and the measurement is performed with the least amount of errors. Lastly, a grounding electrode can be used to ground

the Faraday cage to prevent electromagnetic interference. The measurements discussed in this thesis were done in a grounded Faraday cage.

Although EIS includes complex mathematical calculations, we can straightforwardly express the fundamental concept of impedance. Impedance is closely related to resistance, which is the tendency to resist electrical current. However, impedance is used in alternating current systems, where the current changes with respect to time or frequency. We can show the famous Ohm's Law as impedance as following:

$$Z(f) = \frac{V(f)}{I(f)} \tag{1.21}$$

The word "spectroscopy" may seem irrelevant at first, but we will later discuss that the spectrum can be represented in Bode plots, which have frequency as their x-axis. Most of the time, the frequency range starts from MegaHertz (10^6) to Milli Hertz (10^{-3}). Similarly, the word "electrochemical" refers to the medium in which the resistance is present.

The main working principle of EIS is applying a sinusoidal current signal and observing the voltage response (Galvanostatic EIS) or applying a sinusoidal voltage signal and monitoring the current response(Potentiostatic EIS). This excitation signal has two parameters: amplitude and frequency. For instance, in Galvanostatic EIS, the excitation is made with current that can be described with the following equation:

$$I(f) = I_A sin(2\pi f) \tag{1.22}$$

In this notation, $I(f)$ corresponds to applied current, I_A means current amplitude and f is frequency. However, in most cases, there is also a phase shift(ϕ) in the response signal, which can be added to the formula in the following way:

$$V(f) = V_A sin(2\pi f + \phi) \tag{1.23}$$

Therefore, we can visualize the excitation current and voltage response in the following Fig. 1.7, specially named as Lissajous plot[22].

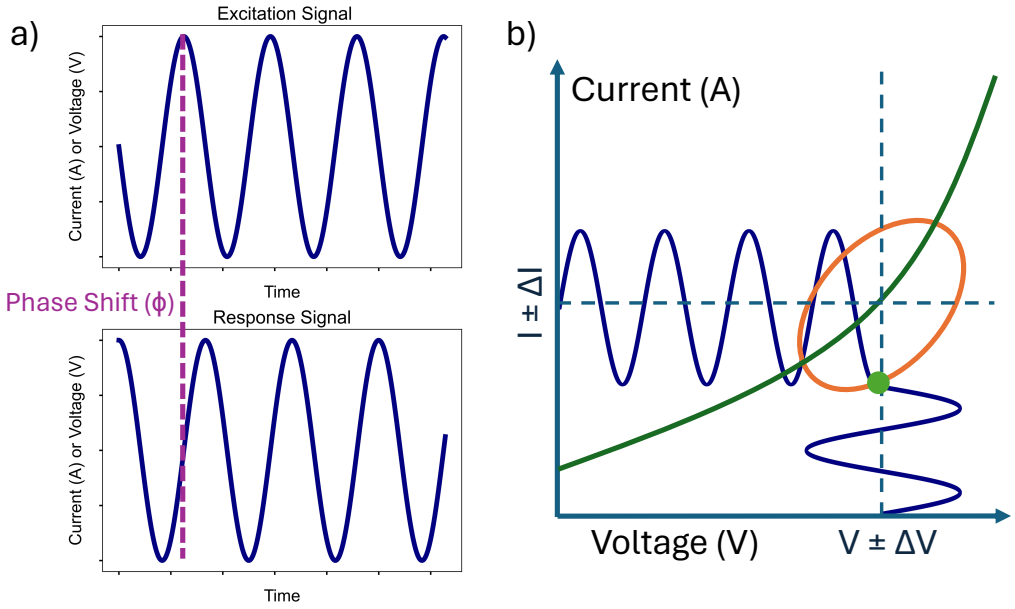

Figure 1.7: The time-domain profiles of the excitation and response signals (a) with a 90°phase (ϕ). The Lissajous plot is a common way of representing these two signals (b). The green dot is the actual measurement point on the Lissajous ellipse, which generally rotates in a clockwise direction (when the excitation signal initially increases).

Lissajous curve analysis can tell us about the linearity and stationarity of the electrochemical system. As shown with the equations above, the ratio of voltage over current gives us the impedance value. However, the impedance is expressed with two parts, real and imaginary, since it is a function of two variables.

$$Z(f) = \frac{V(f)}{I(f)} = \frac{V_A sin(2\pi f + \phi)}{I_A sin(2\pi f)} = Z_r + iZ_i \tag{1.24}$$

As a result, we can express the magnitude in the real part and phase change in the imaginary part as follows:

$$Z = \mid Z_r + iZ_i \mid \quad \text{and} \quad \phi = arctan\left(\frac{Z_r}{Z_i}\right) \tag{1.25}$$

The experimental parameters must be optimized and arranged so that the system exhibits linearity, causality, and stability. For instance, the current-voltage relationship in a kinetically limited reversible system is governed by the Butler-Volmer equation, which has the $e^{(Cons.)\eta} - e^{-(Cons.)\eta}$ term[9]. Therefore, this relationship is exponential in nature. To overcome this obstacle, relatively small amplitudes of the excitation signal are applied to generate a pseudo-linear response. The stability condition is related to the duration of measurement. Usually, it is defined as invariance in the impedance of the system during measurement[24]. Lastly, causality means that the data obtained come from the system entirely, not from external sources. In other words, the reason for the response signal is purely the source of the excitation. When there is no excitation signal, no response should be detected.

The validity of all these concepts can be checked with the Kramers-Kronig

(KK) transformation, which presents a relationship between real and imaginary components of the signal. The following KK formula is taken from *Electrochemical Impedance Spectroscopy by Orazem and Tribollet 2nd Ed.*, equation (22.66)[22]:

$$Z_r(\omega) = Z_{r,\infty} - \frac{2}{\pi}\int_0^\infty \frac{xZ_j(x) - \omega Z_j(\omega)}{x^2 - \omega^2} dx \tag{1.26}$$

In this equation, the real part of the impedance data is calculated from the imaginary components. Additionally, the impedance is dependent on the frequency of the applied signal, which is in the angular frequency term ω. This method was developed by the Orazem group and has been published in numerous publications[25][26][27]. In addition, the Orazem group has published/launched an open-source EIS data analysis program called "*Measurement Model*[28][29][30]." This model also checks for the KK-compatibility of the acquired data by using Voigt elements. As a side note, a Voigt element is a circuit component in which a resistor and a capacitor are connected in parallel[31]. It evaluates the number of Voigt elements necessary for the best fit and calculates the difference between the experimental data points and perfectly linear Voigt elements' fit results. Thereafter, the residuals of the KK fit/evaluation are given with the error limits. Of course, there are many options for the data fit and measurement parameters, but overall, all KK-compatibility tests work the same way.

Another method of evaluating the KK-compatibility was developed by Boukamp[32]. This method utilizes Voigt elements, which are made of a resistance and a capacitor connected in parallel. Since each Voigt element consists of linear circuit elements, their impedance response would be linear. Similarly,

a number of Voigt elements connected in series also yields a linear response. As a result, a complete spectrum, which can be modeled with a number of Voigt elements, can result in a linear impedance response if it overlaps with the real data. Therefore, this method does not include any integration; it just fits the data with an optimum number of Voigt elements. The *Measurement Model* also uses Voigt elements. However, the Boukamp method normalizes the data, whereas the *Measurement Model* does not. The KK spectra in this thesis are also based on this method, which is the default way of evaluating the KK compatibility.

If the response signal is not compatible (not overlapping) with the KK transformation, it would indicate non-linearity or non-stationarity in the measurement. In other words, the system is unstable and does not yield an ordinary and repetitive response if it is non-KK-compatible. Furthermore, the data consistency is also evaluated by the KK relations, where the data is compared against the KK transformation within a tolerance limit.

In the next chapters, Non-linear Harmonic Analysis (NHA) will be investigated, based on the response signal from the system. On this signal, Fourier Transformation will be performed. Fourier Transform is applied to the time domain response, which can be expressed as:

$$x(t) = \sum_{n=-\infty}^{\infty} c_n e^{-in\omega t} \tag{1.27}$$

In this expression, n is the sample number, ω is the angular frequency, which is also 2πf, and c_n is the Fourier series coefficient. Thereafter, this expression is solved for c_n to extract coefficients, which turns into:

$$c_f = \sum_{n=0}^{N-1} x_n e^{\frac{-i\pi f}{N}} \tag{1.28}$$

In this line, N is the number of samples, n is the sample number, x_n is the input signal number, and f is frequency. A non-linear and non-stationary signal has different amplitude signals other than its fundamental signal. For instance, let us say that the 1 Hz fundamental signal had an amplitude of 1 V (in Galvanostatic EIS). We may observe 10^{-3} V response with 2 Hz, and 10^{-7} V signal at 3 Hz. Usually, the trend follows lower amplitudes at higher frequencies.

1.4 Equivalent Circuits

Interpretation of KK-compatible impedance data is generally performed with equivalent circuit elements. Simple circuit elements such as resistors, capacitors, and inductors were connected in a way that the overall impedance response resembles the actual measured data. Therefore, the complex behavior of an electrochemical system can be modeled and individually investigated.

One of the most commonly used equivalent circuit element models is Randles' circuit. It was named after English scientist J.E.B. Randles, who developed this circuit in 1947[33]. It is a simple and effective method to represent the electrochemical processes that occur at the electrode/electrolyte interface.

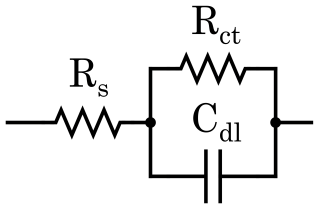

Figure 1.8: Schematic of a simplified Randles' circuit.

There are three main components to a simplified Randles' circuit. R_s term represents the series (or solution) resistance. R_{ct} denotes the charge transfer resistance. The redox reactions occurring on the boundary of the electrode and the kinetic parameters of this process are related to this term. Lastly, the term C_{dl} represents the electrical double-layer occurring on this interface. In some instances, a diffusion element called the Warburg element is also inserted next to the R_{ct}. In a recent publication by Ülgüt and Orazem, it was shown that the correct placement for a Warburg element is within the parallel part of a Randles' cell, not in series with the cell[34].

Overall impedance can be calculated with the following:

$$Z(\omega) = \frac{R_{ct}}{1 + j\omega R_{ct} C_{dl}} + R_s \tag{1.29}$$

In Eq.1.29, j is $\sqrt{-1}$ (imaginary component), ω is the angular frequency of the applied signal, and the $Z(\omega)$ is the frequency-dependent impedance.

Another commonly used circuit is RC segments. It is based on a resistor and a capacitor connected in parallel. This unit is also referred to as Voigt element[35].

Its impedance can be calculated with the following formula:

$$Z(\omega) = \frac{R}{1 + j\omega RC} \tag{1.30}$$

Modeling the impedance spectrum with equivalent circuit elements plays a critical role in investigating the complex nature of electrochemical processes. Although fitting the whole spectrum from point to point is highly challenging, certain processes (or semi-circles) can be easily fitted with proper elements. After the fitting process, certain parameters can be extracted and analyzed according to the context. Those parameters can include resistances, capacitances, and inductances; further investigations rely on those parameters. The fitting process can produce an error interval for each equivalent circuit element used in the model. By investigating these errors, one can deduce whether the model is a suitable one for the data or not. Furthermore, most of the fitting software gives an error value between the fit and the real data for the whole fitted segment. This error value confirms the error of the fit (χ^2) or the *goodness of the fit* and thus can be reported.

One must consider a few crucial points of the equivalent circuit fitting process. First of all, the correct circuit must be selected. Missing elements or excess usage of those elements leads to an unreliable fit. The error value of the fit must be small enough to satisfy the overlap between the fit and the data. Secondly, including all the data points for an ideal fit is essential. If done correctly, the equivalent circuit fit can represent the whole process with the least amount of error. Lastly, considering the non-ideal circuit elements would require modifications to the circuit elements. For instance, many times throughout this thesis, a

constant phase element (CPE) is used instead of a capacitor[36]. The impedance of a CPE is given in Equation 1.31.

$$Z_{CPE}(\omega) = \frac{1}{Q(j\omega)^{\alpha}} \tag{1.31}$$

In this equation, Q is the frequency-independent term that is in the unit of F/cm^2. α is the exponential term that determines the non-ideality of the CPE. If the α value is equal to 1, the CPE shows an ideal capacitor behavior. If it is zero, then the CPE turns into a resistor. The α value is set to be between 0.7 and 1 to model a leaking (non-ideal) capacitor. A non-ideal capacitor (modeled with a CPE) has differences from an ideal capacitor, such as electrode surface roughness, porous electrodes, and non-uniform dielectric material[37][38].

On the other hand, using equivalent circuits has its own disadvantages. Degeneracy is commonly observed in complex data where more than one way of representing the real data is possible. Therefore, selecting the correct circuit is challenging and requires additional experiments. Furthermore, complexity can cause the data to be misfit, and generally, changing the experimental parameters is required.

1.5 Visualization: Bode & Nyquist plots

Impedance data has two components: real and imaginary. Those components are plotted in a few different ways. Bode plot is commonly used to investigate the phase angle and the modulus of the impedance response[39]. Although it can be

plotted separately in two different plots, we will use a double-y plotting style to represent Bode plots. The frequency range and the impedance are usually plotted on a logarithm scale, whereas the phase angle is plotted on a linear scale. Plotting the impedance as a function of frequency enables the detection of characteristic frequencies. Similarly, plotting the phase angle as a function of frequency can visualize the delays and phase shifts of the electrochemical system. Furthermore, a trained eye can detect the number of time constants of impedance data by looking at the Bode plot.

Another common method for visualization of impedance data is called the Nyquist plot, which shows the real part of the impedance on the x-axis and the negative of the imaginary part on the y-axis. The shape(s) on the Nyquist plot provide information about the nature of the electrochemical system. A common feature of a Nyquist plot is the observation of semi-circles that arise from the RC components of the impedance elements. The diameter and height of the semi-circle are related to the resistance and capacitance of the RC circuit element. Additionally, the time constant of the semi-circle can be extracted from these resistance and capacitance values as follows:

$$\tau = \frac{1}{2\pi RC} \tag{1.32}$$

In Equation 1.32, τ is the time constant in Hertz, and R and C are the resistance and capacitance values, respectively.

Equivalent circuit fits are usually performed on the Nyquist plots. The number of RC components, solution resistance, and diffusion elements can be easily

identified on a Nyquist plot. However, as shall be discussed in later chapters, impedance data can be fitted with equivalent circuit elements only if it is KK-compatible.

Since the tools and the plots of impedance data analysis have been introduced, simple circuit elements' impedance responses can be investigated. High impedance values (a few kΩ or more) can be measured in Potentiostatic EIS, where the input voltage amplitude is controlled. On the contrary, low impedance values (10 Ω or less) can be measured more accurately with Galvanostatic EIS with the controlled AC amplitude.

A simple resistor gives a flat Bode plot, which indicates a frequency-independent response. This is due to the lack of reactive components and energy storage/release mechanisms. The impedance of a resistor is $Z = R$, and there are no angular components present. As a result, flat magnitude and zero phase shift are observed, as seen in Figure 1.9.

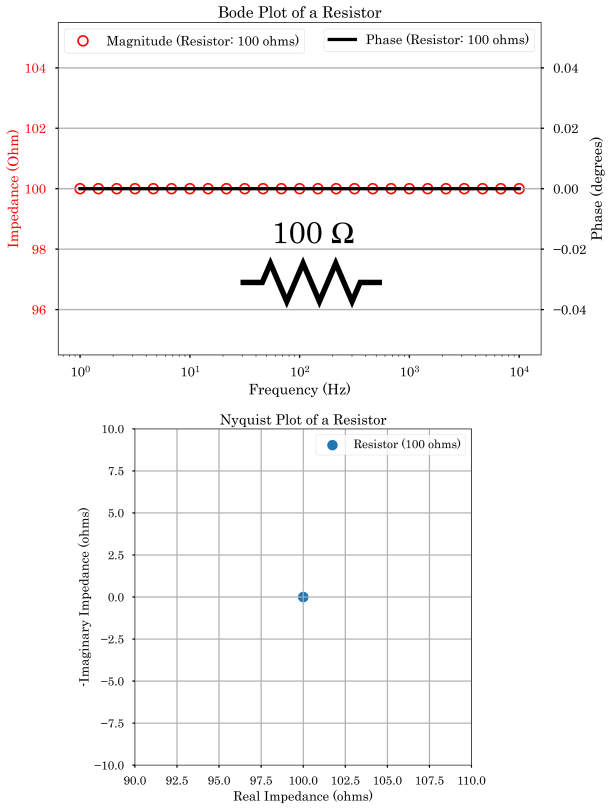

Figure 1.9: Bode (upper) and Nyquist (lower) plots of 100 Ω resistor.

A capacitor shows a frequency-dependent impedance response, as seen in Figure 1.10. The impedance of a capacitor is given by the formula:

$$Z = \frac{1}{j\omega C} \tag{1.33}$$

The term ω is the angular frequency of the applied signal; as the frequency decreases, the impedance (Z) increases. Additionally, the phase angle (phase lag) plot is reaching 90° at the lower frequencies. On the Nyquist plot, at high frequencies, the impedance of a capacitor appears to be a single point on the real axis. As the frequency decreases, it gradually and perpendicularly increases.

This increase is due to the domination of the capacitance behavior and the phase lag observed in the Bode plot. The Bode and Nyquist plots can be seen in Figure 1.10.

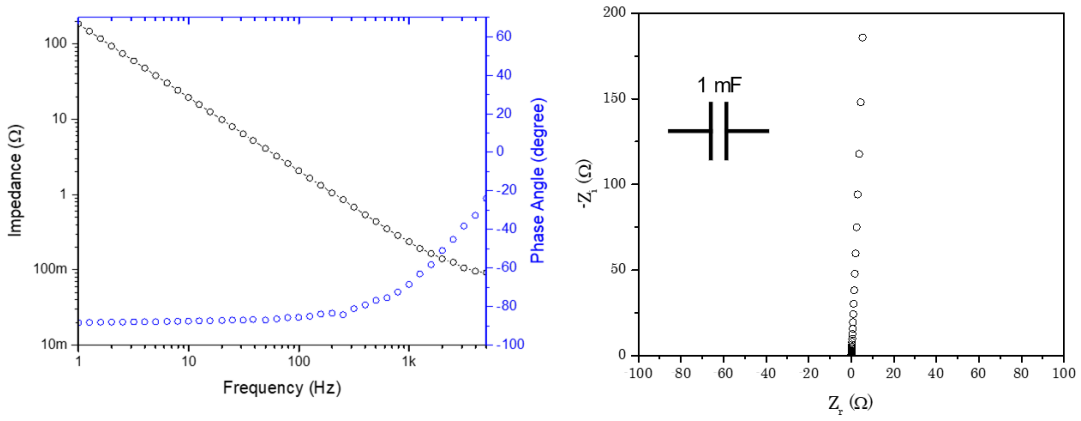

Figure 1.10: Bode (left) and Nyquist (right) plots of a simple one mF capacitor.

Another frequently observed phenomenon in impedance data (on Nyquist plots) is the semi-circles of RC components. Experimentally, a resistor and a capacitor connected in series were measured, and the Bode and Nyquist plots can be seen in Figure 1.11. At high and low frequencies, the imaginary component of impedance approaches zero, and the data points accumulate around the real axis. Similarly, the impedance approaches the DC resistance at the lower end of the frequency range, where only the real part of the impedance is observed. The width (real impedance) and height (imaginary impedance) of the semi-circle are controlled by the resistor and the capacitor, respectively. The tip of the drop

in the phase angle indicates the time constant of the RC element, which can be calculated by the formula:

$$\tau(Hz) = \frac{1}{2\pi RC} \tag{1.34}$$

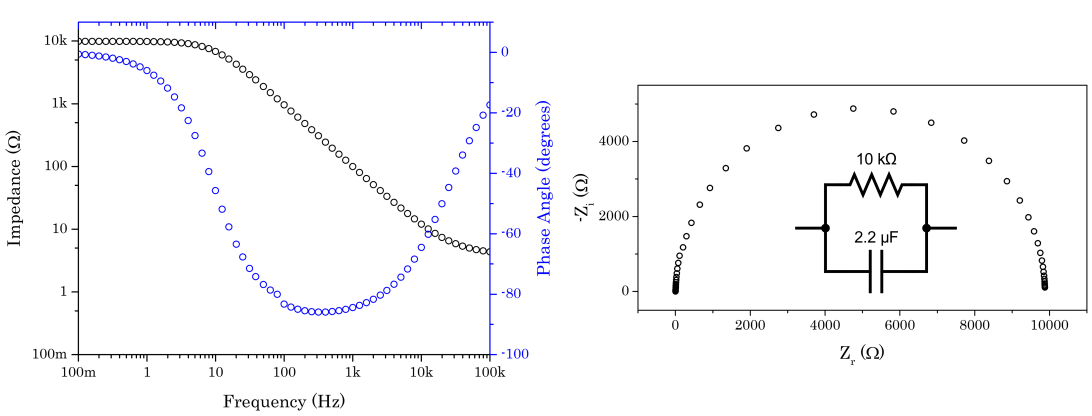

Figure 1.11: Bode (left) and Nyquist (right) plots of an RC unit with 10 kΩ resistance and 2.2 μF capacitor. The discontinuity of phase angle at 100 Hz is due to a filter engaging/disengaging at lower/higher frequencies. It is an instrumental artifact and is not significant in our discussions.

In an RC component with a pure capacitor, the semi-circle is exactly circular. However, real-world data rarely have perfect semi-circles. The constant phase element is introduced when the semi-circle looks suppressed from the top. The overall impedance of a constant phase element is described in Eq. 1.31, and the total impedance of an RC with a constant phase element can be calculated by the following Eq 1.35:

$$Z = \frac{R}{1 + Q(J\omega)^{\alpha} R} \tag{1.35}$$

A simulation based on this formula is plotted in Figure 1.12. In the figure, only the α values are changing from 1.0 (ideal capacitor) to 0.7 (lower limit for an acceptable α value). The peak of the semi-circle gets depressed as the α value gets smaller. In our fitting software, Gamry Echem Analyst v.7.10, α values have these lower and upper limits and cannot exceed the limits in any of the fits.

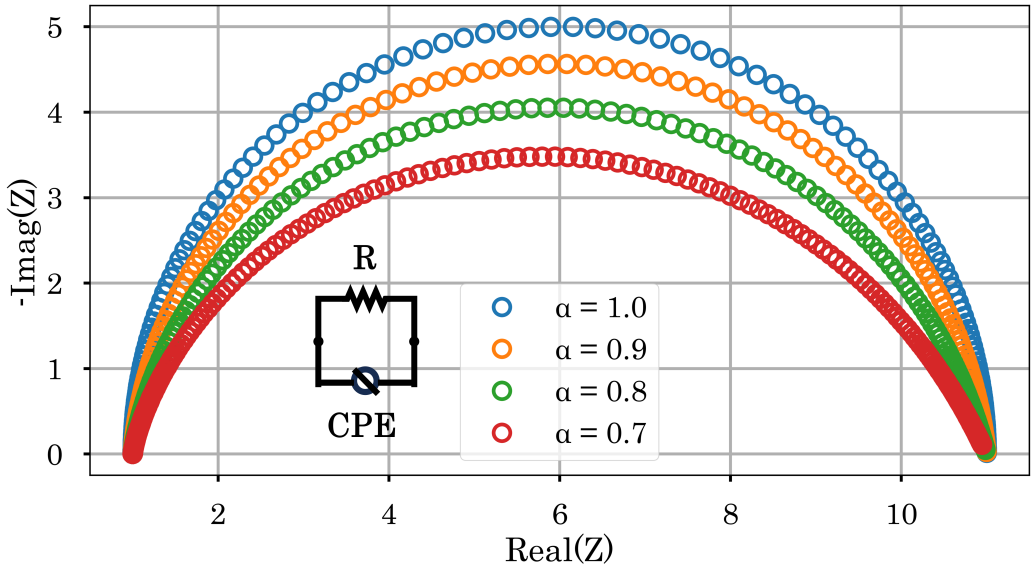

Figure 1.12: Nyquist plot of an RC element with a constant phase element (CPE), with different α values.

Lastly, the impedance response of a simplified Randles' cell should be investigated. The series resistance determines the high-frequency end of the semi-circle on the real (Z_r) axis. Similarly, the width of the semi-circle on the real axis is

related to the parallel resistance. The radius of the semi-circle depends on the resistance value, and the time constant of a semi-circle can be acquired from the capacitance value as well. The Bode and Nyquist plots can be seen in Figure 1.13.

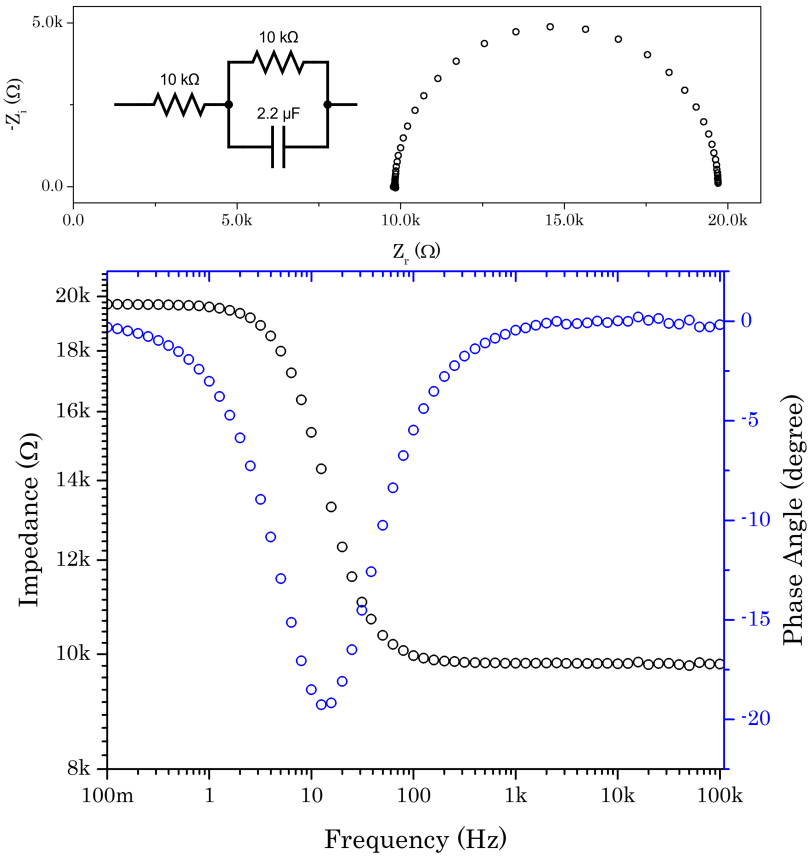

Figure 1.13: Bode (left) and Nyquist (right) plots of a Randles' cell. The series and parallel resistances are 10 kΩ, and the capacitor is 2.2 μF.

1.6 Organization of the Thesis

In this thesis, the introduction chapter consists of the motivation, the fundamental concepts about electrochemistry, batteries and evaluation methods, data visualization ways, and a brief description of various circuit elements.

Chapter 2 is about the methodology and experimental details of the conducted experiments. This section includes information on the performed methods and data analysis processes.

Chapter 3 will be about my first paper, which evaluates the occurrence of the initial transient phenomenon in EIS measurements via investigating with simulations and dummy cell measurements[40].

Chapter 4 will cover temperature-dependent EIS discussions based on a recent publication and ongoing research projects[41]. The chapter also introduces the theoretical section regarding the activation energy calculations via Arrhenius relations.

Chapter 5 is about a recently published study based on the relationship between the Kramers-Kronig (KK) and Non-linear Harmonic Analysis (NHA), demonstrated on $Li/SOCl_2/SO_2Cl_2$ battery systems. This section also delves into the proper EIS measurements of these batteries.

Lastly, the appendix section includes a side project on the EIS measurements of various types of electric guitar pickups and experimental notes for the devices used in the lab.

Chapter 2

Methodology & Experimental Setup

In this chapter, details regarding the measurement and analysis methods are discussed. A critical process in EIS measurements in this study is the equivalent circuit fitting, which is performed on Gamry Echem Analyst. Moreover, the non-linear harmonic analysis is also presented alongside the Python code in the following parts. Additionally, the notes and procedures for the devices can be found in the Appendix of this thesis.

2.1 Equivalent Circuit Fitting

The fitting process starts with a Kramer-Kronig compatibility test of the Gamry Echem Analyst. The points per decade value is set to be automatic. When Gamry's KK algorithm is investigated thoroughly, the points per decade are set to have a maximum value of 7 points per decade if the measurement was done with a higher points per decade value. On the other hand, if the data is taken

with less than 7 points per decade, the points per decade of the KK fit is the same number as the measurement parameters.

A satisfactory or acceptable equivalent circuit fit must represent the experimental data accurately and provide the necessary information about the system measured. This information includes the number of electrochemical processes occurring in the system, the physical relevance of the equivalent circuit, and the limitations or constraints of the system. Therefore, an equivalent circuit fit generally includes a numeric error value between the fit and measurement. Depending on the model and the measurement, these error values have acceptable ranges and limits and can be determined individually. Additionally, the circuit should be robust, i.e., it should fit the data set under different experimental conditions such as temperature or SoC changes.

Similarly, the quality of the acquired spectrum can be evaluated using Kramers-Kronig (KK) relations. Although there are a few ways of calculating the KK line, Gamry software uses the method which was proposed by Boukamp[32]. Briefly, this method consists of Voigt elements, which are RC elements connected in parallel. Each RC element is linear by its nature. Therefore, the overall KK model and the KK-compatible spectrum should also be linear. As a result, if the experimental spectrum is overlapping (compatible) with its KK transformation with an acceptable fit error, it can be considered KK-compatible.

2.2 Constant Phase Element (CPE) and Effective Capacitance

In the equivalent circuit fits of the experimental impedance measurements, a constant phase element (CPE) is used instead of a capacitor. Since non-ideal behaviors, such as charge and mass transfers, occur frequently on the modeled surfaces or interfaces, the modeling requires a few additional elements to fit properly.

To begin with, the impedance of a CPE can be written as follows:

$$Z = \frac{1}{Q(j\omega)^{\alpha}} \tag{2.1}$$

In this equation, Q is the CPE constant, which is in the unit of $\frac{s^{\alpha}}{\Omega}$. Therefore, when the α is equal to one, the CPE becomes an ideal capacitor, and the Q value becomes the capacitance. Similarly, when α is equal to zero, the overall expression turns into the reciprocal of resistance ($\frac{1}{\Omega}$), and CPE behaves as a resistor. Moreover, when the α is 0.5, it becomes a square root function. Since most of the square-root functions are related to diffusion in electrochemistry, CPE becomes the Warburg element, which is used for modeling diffusion processes in electrochemical systems. Thus, the Q value becomes Q_W and is defined as the Warburg coefficient.

When the α value is less than 1, Q cannot simply represent the capacitance[42]. For the cases where α is less than 1, different approaches should be performed. Brug et al. published the modeling of CPE with non-ideal behavior and concluded the effective capacitance[43]. In a study by Orazem et al., different methods of

capacitance evaluations are performed with diverse measurement samples such as human skin or steel[44]. In another study by Hirschorn et al., CPE is used for film structure characterization with different α values[35]. Overall, the effective capacitance (C_{eff}) of a CPE can be written as:

$$C_{eff} = Q^{\frac{1}{\alpha}}[R_e^{-1} + R_t^{-1}]^{(\alpha-1)/\alpha} \tag{2.2}$$

In this equation, R_e is the ohmic resistance, and R_t is the charge transfer resistance[42]. Therefore, the CPE should be approached carefully when the α is less than one. In these cases, the effective capacitance values can be acquired with slight variations. In the equivalent circuit fits of this thesis, the α value is set to be between 0.7 and 1 on Gamry's Echem Analyst software. The unit for the non-ideal capacitor (or CPE) is $\frac{1}{Ss^{\alpha}}$ and is denoted as effective capacitance. In this equation, S is the reciprocal of resistance, which is in the unit of Siemens. Therefore, the overall unit of the effective capacitance can be written as:

$$C_{eff} = \Omega^{-1/\alpha} s^{-1+\frac{1}{\alpha}} \tag{2.3}$$

Consequently, when the α is equal to one, the unit is Farad (F). When it is in the range $0.7<\alpha<1$, it is involved in the discussion above.

2.3 Non-linear Harmonic Analysis (NHA)

Non-linear harmonic analysis (NHA) is a frequently used technique in various chapters of this thesis. NHA can present the non-linear behaviors of the investigated electrochemical system by analyzing the response[45]. These non-linearities include kinetic and interfacial phenomena, symmetry of the system, and state of health information[46][47]. The NHA data is presented in a Bode plot where the x-axis is the frequency of the measurement, and the y-axis is the response signal amplitude.

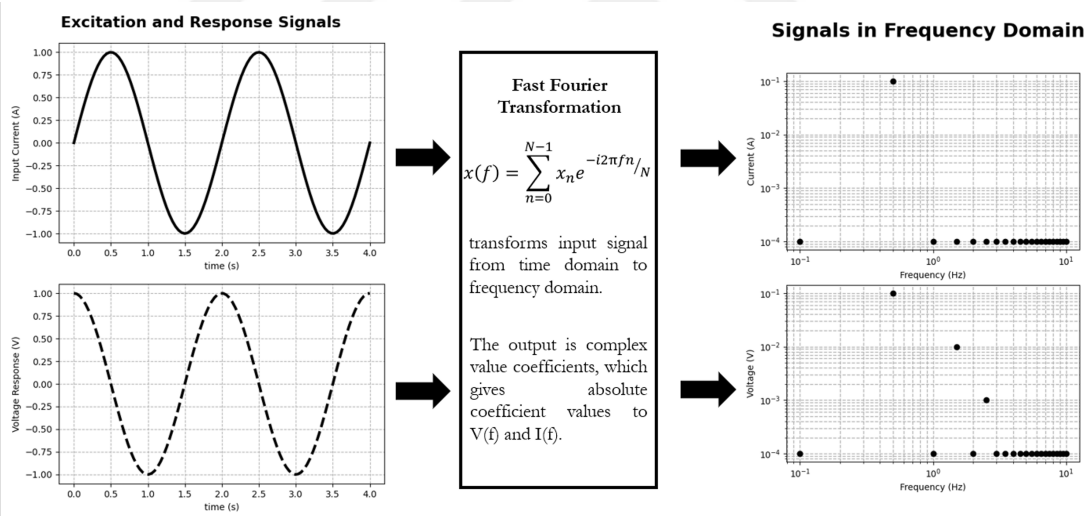

Figure 2.1: Illustration of harvesting the information regarding the NHA analysis. The process is done using Python code.

The overall data acquisition process is shown in Figure 2.1. For this purpose, we have written a custom Gamry measurement script for this measurement. In this script, the potentiostat receives the response in the time domain at each applied frequency. Besides, the response is also saved as regular EIS

data for KK-compatibility and equivalent circuit fit processes. Then, a Python script converts this response to the frequency domain by utilizing the Fast Fourier Transformation (FFT) function of the SciPy library. For each frequency in the measurement, the script calculates the overtones or harmonics. For instance, the second harmonic has twice the frequency of the fundamental response, and the third harmonic has triple the frequency of the fundamental response, and so on. Thereafter, these calculated harmonics and fundamental responses are plotted in terms of their amplitude for each frequency. As a result, a Bode plot of the response signal with harmonics is acquired.

The code for the NHA can be found in the following section. In this code, data is recorded in the time-domain format with a custom Gamry script. Thereafter, a fast-Fourier Transformation is applied to the signal to acquire frequency-domain data. For each frequency, the amplitude of this fundamental response signal and its harmonics' are calculated.

```
import glob,os
import numpy as np
import pylab as plt
import scipy.fftpack


rangebegin = 32
rangeend = 80
frange = (rangeend-rangebegin)/2 - 1
freqlimit = 1000


def fft(voltage_array,st):

    freqlength = int(len(voltage_array)/2)
    fftfreq_ =
        scipy.fftpack.fftfreq(int(len(voltage_array)),st)[:freqlength]
    fft_voltage
        =2*abs(scipy.fft(voltage_array))[:freqlength]/len(voltage_array)


    return(fft_voltage,fftfreq_)


def MatchAbsNearest(array,element):
    mindif = 1e38
    imin = 0
    for i in range(len(array)):
        idif = abs(abs(element)-abs(array[i]))
        if  idif < mindif:
            imin = i
```

```
            mindif = idif
    return imin

harmonic_amplitudes = []
harmonic_frequencies = []
fundamental_amplitudes = []
fundamental_frequencies = []
third_harmonic_amplitudes = []
third_harmonic_frequencies = []
fourth_harmonic_amplitudes = []
fourth_harmonic_frequencies = []
fifth_harmonic_amplitudes = []
fifth_harmonic_frequencies = []

os.chdir(folderused1)

for filename in glob.glob('*'):
    if float(filename) <= freqlimit:
        inputarray = np.genfromtxt(filename, skip_header = 3,
            invalid_raise = False, dtype = [('Pt','i8'), ('T','f8'),
            ('Vf','f8'), ('Im','f8'), ('Vu','f8'), ('Sig','f8'),
            ('Ach','f8'), ('IERange','f8'), ('Over','f8')])
        ydata = inputarray['Vf'][rangebegin:rangeend]
        st = inputarray['T'][1] - inputarray['T'][0]
        fft_voltage,fftfreq_ = fft(ydata,st)

        fundamental_index = np.argmax(fft_voltage[1:])
        fundamental_index = fundamental_index + 1
```

```
fundamental_frequency = fftfreq_[fundamental_index]
fundamental_amplitudes.append(fft_voltage[fundamental_index])
fundamental_frequencies.append(fundamental_frequency)

harmonic_index =
    MatchAbsNearest(fftfreq_,fundamental_frequency*2)
harmonic_frequency = fftfreq_[harmonic_index]/2
harmonic_amplitudes.append(fft_voltage[harmonic_index])
harmonic_frequencies.append(harmonic_frequency)

third_harmonic_index =
    MatchAbsNearest(fftfreq_,fundamental_frequency*3)
third_harmonic_frequency = fftfreq_[third_harmonic_index]/3
third_harmonic_amplitudes.append(fft_voltage[third_harmonic_index])
third_harmonic_frequencies.append(third_harmonic_frequency)

fourth_harmonic_index =
    MatchAbsNearest(fftfreq_,fundamental_frequency*4)
fourth_harmonic_frequency = fftfreq_[fourth_harmonic_index]/4
fourth_harmonic_amplitudes.append(fft_voltage[fourth_harmonic_index])
fourth_harmonic_frequencies.append(fourth_harmonic_frequency)

fifth_harmonic_index =
    MatchAbsNearest(fftfreq_,fundamental_frequency*5)
fifth_harmonic_frequency = fftfreq_[fifth_harmonic_index]/5
fifth_harmonic_amplitudes.append(fft_voltage[fifth_harmonic_index])
fifth_harmonic_frequencies.append(fifth_harmonic_frequency)
```

Also, the code for the Gamry potentiostat is given here, based on a previous publication of our group[47]. This code can be implemented in the custom script section inside the framework.

```
    NUMBEROFCYCLES = 5
NUMBEROFPOINTS = 16
DDSCutoff = 100.0
Pstat.SetVoltage (0.0)
Output.Close() ; Close the main file, so that doesn't get corrupted
if (ReadZGalv.Zfreq() gt DDSCutoff)
Pstat.SetDDSAmpl(1.41*Sac) ; Setup the sine wave application
Pstat.SetDDSFreq(ReadZGalv.Zfreq())
Pstat.SetDDSEnable(TRUE)
Signal =
    ICONST.New("SIGNAL",Pstat,IDCReq.Value(),NUMBEROFCYCLES*1.0/Freq,
& 1.0/(NUMBEROFPOINTS*Freq)) ;
else
Pstat.SetDDSEnable(FALSE)
Mysignal = VectorNew(Index(NUMBEROFCYCLES*NUMBEROFPOINTS))
VectorRLE = VectorNew(VectorCount(Mysignal))
SampleTime = 1.0/(ReadZGalv.Zfreq()*NUMBEROFPOINTS)
i=0
while(i lt VectorCount(Mysignal))
MyPhase = ((i*SampleTime)*ReadZGalv.Zfreq()- Index((i*SampleTime)
& * ReadZGalv.Zfreq())) * 2.0*PI
Mysignal[i] = IDCReq.Value() + IACReq.Value()*Sin(MyPhase)
VectorRLE[i] = 1
i=i+1
```

```
Signal = IARRAY.New("SIGNAL", Pstat, IDCReq.Value(), 1 , SampleTime,
& Mysignal, VectorRLE, BIASMODE_INPUT)
Pstat.SetSignal(Signal)
Curve = IVT.New ("CURVE", Pstat)
Curve.SetPlotView(0.05, "Time", IVT_Vf, 0.0, "V", "V", IVT_Im, 0.0,
    "I", "A")
Pstat.SetCell (CellOn)
Curve.Activate()
Curve.Run()
Pstat.SetDDSEnable(FALSE)
Filename = Sprint(".\\LissGalv\\",Freq)
LissOutput = OUTPUT.New ("OUTPUT",Filename, "Output &File")
LissOutput.Open()
Curve.Printl()
LissOutput.Close()
Output.Append()
Pstat.SetVoltage (Sdc)
```

In the conventional EIS measurements, non-linear electrochemical processes are invisible. By utilizing the NHA, those non-linearities can be investigated. Furthermore, more than one electrochemical process can have close time constants and exhibit overlapping EIS responses. Similarly, the difference can be detected by the NHA of the data. On the other hand, the complexity of the acquired spectrum makes the correct interpretation of the system significantly difficult. Analysis of the data requires comprehensive research and experience. In addition, there can be artifacts that are not related to the electrochemical reactions but result from experimental conditions. The investigation and diagnosis of these

artifacts require control experiments with simple design elements or simulations based on the investigated system.

2.4 Conclusions

In this chapter, the details of the EIS measurements are provided in terms of equivalent circuit fitting and NHA and Kramers-Kronig (KK) relations. In addition, the code snippets for the NHA are given and explained to provide a comprehensive understanding of the data acquisition and treatment processes. Furthermore, the constant phase element is discussed to yield the capacitance values within the limited pre-exponential factor values.

Chapter 3

Initial Transients

3.1 Introduction

This section is based on our group's publication entitled "Methods–Unexpected effects of galvanostatic EIS of Randles cells"[40].

In the introduction section, we discussed that the EIS data should be compatible with KK and have lower amplitude harmonics. Otherwise, the data would be useless and discarded. However, the origin of these defects can be beneficial in EIS studies. In recent years, there have been several studies that investigated non-linear harmonics and their mechanistic and kinetic reasons[48][49][50].

As mentioned in the introduction section, the study of harmonics requires applying Fourier Transformation (time domain to frequency domain) to obtain a response signal. Then, the components at each frequency are analyzed and plotted. Stationary and linear signals result in no harmonics, but nonlinear and

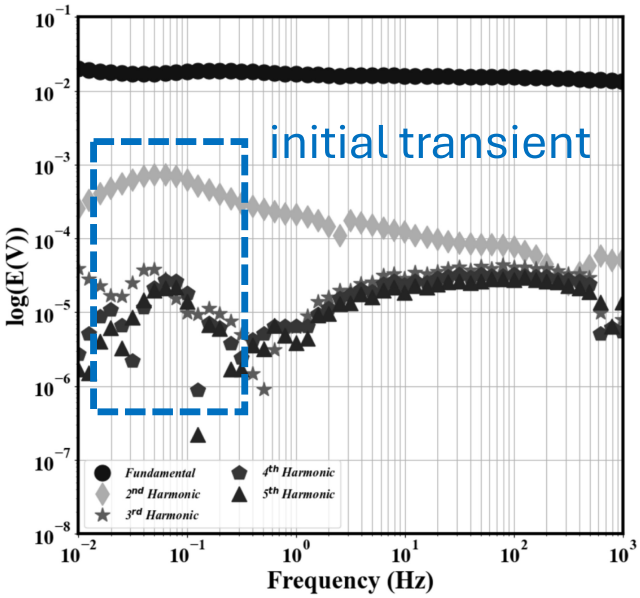

Figure 3.1: Non-linear harmonic analysis of a Li/$SOCl_2$ battery with initial transients being shown in the blue rectangle.

nonstationary signals result in characteristic harmonics.

The main motivation for this study is the occurrence of peaks/shapes in NHA plots of various systems. In these plots, all of the harmonics exhibit an increase and a decrease over a frequency range, similar to a peak. Therefore, a detailed investigation idea emerged, and we started working from there. An initial transient is a natural process that occurs in all impedance measurements. The first few cycles generally do not yield a steady and linear response. Rather, they exhibit a decaying or non-stationary response signal. They are mostly observed in the first few cycles of measurements, therefore named *initial transients*.

For instance, in Figure 3.1, initial transients are present at lower frequencies. After many encounters with this shape in our measurements, the investigation continued with experimenting with dummy cells. The effect was also observed

with dummy cells, and eventually, the simulations of the same dummy cell experiments were performed. As a result, this initial transient phenomenon is always present in all measurements and cannot be removed completely.

A comprehensive illustration of nonlinear harmonic analysis can be seen in Figure 2.1. For these calculations in our study, we employ NumPy, Matplotlib, and SciPy libraries of Python on Spyder IDE[51][52][53]. The complete code can be found in the publication appendix.

In our publication, we have demonstrated the initial transient effect and generation of harmonics on simplified Randles' Cells. Simplified Randles' Cell is made of a series resistor (R_s) and a resistor(R_{ct}) and capacitor(C_{dl}) in parallel. A brief illustration can be seen in Figure 1.8.

The complete Randles' circuit contains a Warburg element, which is connected next to the charge transfer resistor R_{ct}. Warburg element is responsible for diffusion. This effect results from the non-linear part, which can be beneficial for understanding the linear behavior of the electrochemical system. As explained earlier, nonlinear harmonics require a series of mathematical calculations, such as Fourier Transformations, to investigate the results. Very simply, signals with a frequency higher than the fundamental frequency indicate non-linearity and can be analyzed accordingly.

Investigating the literature, in a study by Vidakovic et al., the researchers emphasized the importance of nonlinear harmonics in kinetic studies of electrochemical systems[54]. In another study by Murbach et al., the non-linear harmonic response was linked to the aging and thermodynamic properties of commercially available batteries[55]. Furthermore, Harting et al. published numerous papers

on the aging process of batteries at different temperatures[56][57][58]. Similarly, Liebhart and co-workers have published about using nonlinear EIS at lithium-ion battery characterization at different temperatures[59]. Moreover, Kiel et al. showed the usage of higher-order harmonics in EIS measurement and supported their proposal by building simple Randles circuit models for simulation[48]. Recently, we have also published our work about nonlinear harmonic analysis of $Li/SOCl_2$ batteries[47].

3.2 Results and Discussion

We have built two dummy cells (simplified Randles' Cells) to test and simulate the effect. The schematic of a cell was demonstrated in Figure 3.2, whereas our cells can be seen in the following figure:

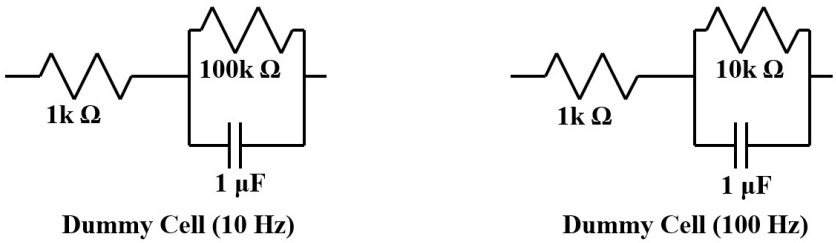

Figure 3.2: Two dummy cells that were used in this research. *This figure is reproduced with permission.*

Time constants (the frequencies written next to each cell) can be calculated with $\frac{1}{CR_p}$ since the series resistance (R_S) is only an additive factor. The experimental conditions, such as the current values, start-finish frequencies, and points

per decade values, were kept the same for the simulation of the cells.

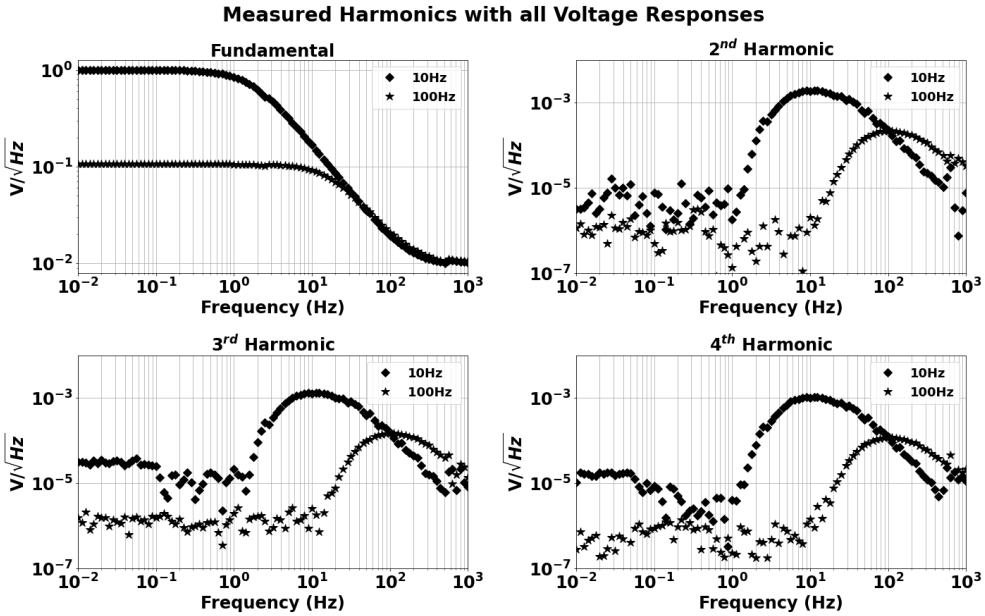

Figure 3.3: Response Harmonics of two dummy cells. *This figure is reproduced with permission.*

A comprehensive illustration of nonlinear harmonic analysis can be seen in the Figure 3.3. In the following figures, we can see the measured and simulated harmonics of the two dummy cells. The peak values correspond to the time constants. The harmonics also have a decreasing trend as the harmonic number increases. In our study, we were able to recreate this experimental result exactly with a simulation. The basic principle of the simulation is based on the fundamental laws of electric circuits. When a set of formulas is applied, the current can be distributed across the resistor and capacitor, depending on their values (magnitudes). The complete equations can be found in the following part, where the initial transients are derived from simple equations. Thereafter, the simulation was performed with the same experimental parameters, such as points per

decade value, initial and final frequencies, and amount of applied and removed signal segments. The simulation results are given in Figure 3.4. When plotted side by side with measured results, it becomes challenging to see the difference between the simulated and the measured harmonics. This simulated harmonic has a 0.1% noise level added to the main signal.

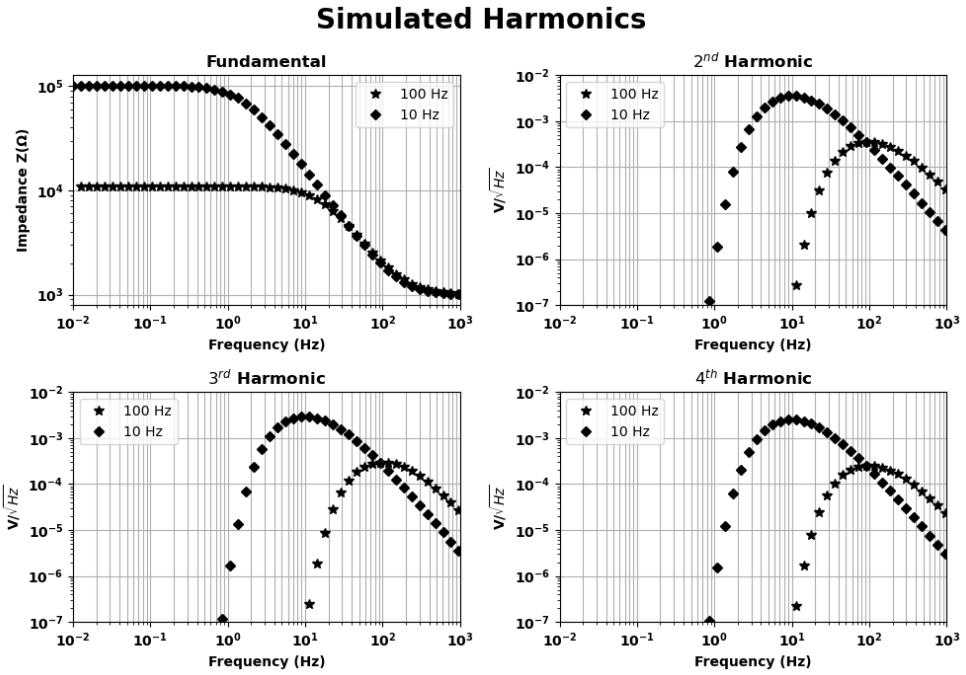

Figure 3.4: Simulated Response Harmonics of two dummy cells. The real-life measurement includes noise, which can also be simulated by adding a 0.1% noise level to the main signal amplitude. *This figure is reproduced with permission.*

The simulation of the dummy cells requires a few assumptions based on the fundamental laws of simple circuit elements. The overall voltage across the dummy cell is the summation of voltages on the resistor and the RC component. The parallel part of the circuit gives the voltage as follows:

$$i_R * R_P = \frac{\int_0^t i_C dt}{C} \tag{3.1}$$

In this equation, the voltage is equal across the resistor and the capacitor since they are connected in parallel. Additionally, the term i_R corresponds to the current passing through the parallel resistor, and i_C is the current through the capacitor. Consequently, the summation of these two currents would give the total current that passes through the circuit:

$$i_R + i_C = i \tag{3.2}$$

In this equation, i stands for the total current. The reorganization of these two equations in terms of i_C as a function of C, R_P, and i leads to the following:

$$i_C = i - \frac{1}{C * R_P} * \int_0^t i_C dt \tag{3.3}$$

This equation can be re-written as a discrete time series as follows:

$$i_C[j] = i[j] - \frac{1}{C * R_P} * \sum_{0}^{index-1} i_C[k] * t_s \tag{3.4}$$

In this statement, the t_s is the sampling time, and j is the current array index. This equation can also give the current to pass through the capacitor. However, one should note that there are no current assumptions here, so it can be used to simulate random current sequences. Therefore, the current through the capacitor

and the resistor can be calculated, and the voltage is formulated as follows:

$$E = i[j]R_S + \sum_{0}^{index} i_C[k] * \frac{t_s}{C} \tag{3.5}$$

Another rearrangement of this equation is the following:

$$E = i[j] * R_S + (i[j] - i_C[j]) * R_P \tag{3.6}$$

The waveform of the current is not stated in these equations. One can simulate the analytical solution for Eq. 3.3 based on a sinusoidal form of current. However, it is not the aim of this discussion.

The time-domain simulation data is performed before the Fast Fourier Transformation (FFT) to simulate the harmonics with the fundamental harmonic response. Five cycles of the excitation signal were applied, and the first complete cycle was removed before the FFT. As a result, closely matching simulated and measured harmonic responses were observed. Thus, the experimental results demonstrate that the harmonics only result from the simple structure that was built as the simulation.

Lastly, the total number of cycles and how many of these cycles can be discarded before the analysis can affect the initial transients. For instance, a typical EIS measurement measures five cycles in total and discards the first cycle. A simulation scenario without discarding this first cycle is performed, and the results can be seen in Figure 3.5. As a result, the initial transients have increased presence and amplitude without any discarding process. Therefore, the main

purpose of this removal of the initial cycle is to suppress the initial transients at the critical frequencies.

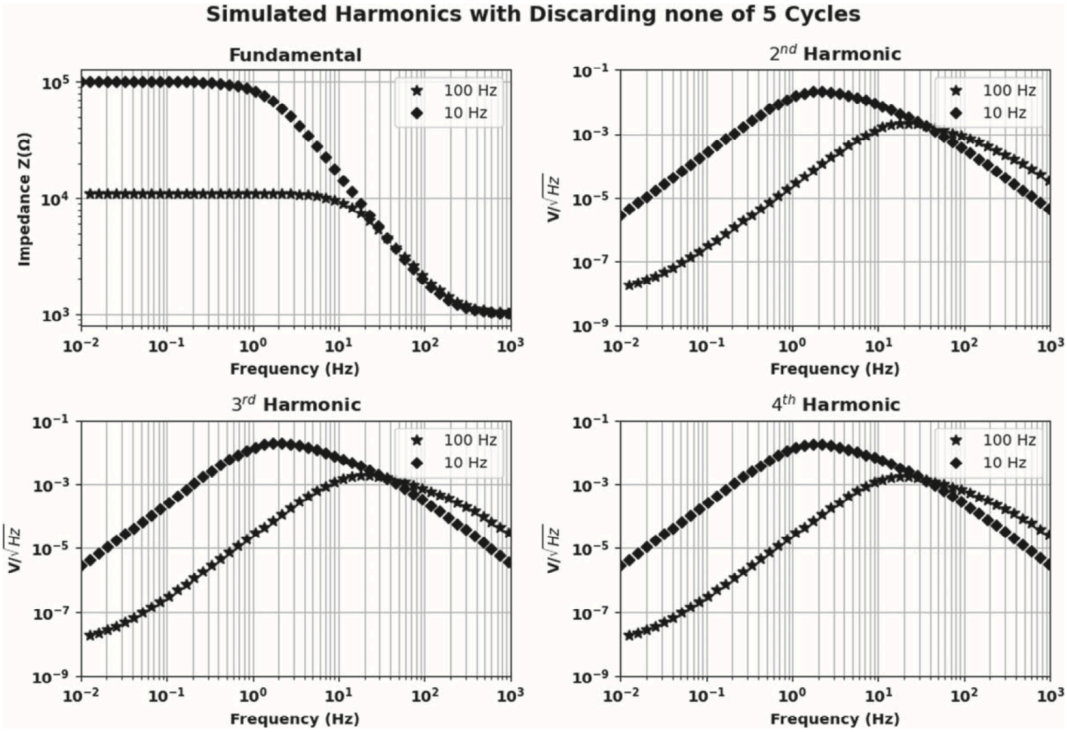

Figure 3.5: Simulated results without discarding any cycles, with a total of five cycles. *This figure is reproduced with permission.*

On the other hand, a non-realistic but simulated scenario can be performed by applying 30 cycles and discarding the initial 25. In this case, the initial transients have even more suppressed presence but are still observable easily, as seen in Figure 3.6. Therefore, the initial transient is present even in unrealistically long measurement times and cannot be got rid of. Moreover, the shape of the initial transients can be notified on NHA data and should be treated accordingly.

Overall, NHA provides substantial information about the investigated electrochemical system. However, one must use it carefully with additional control experiments based on dummy cells or equivalent circuit elements. Thereafter, the

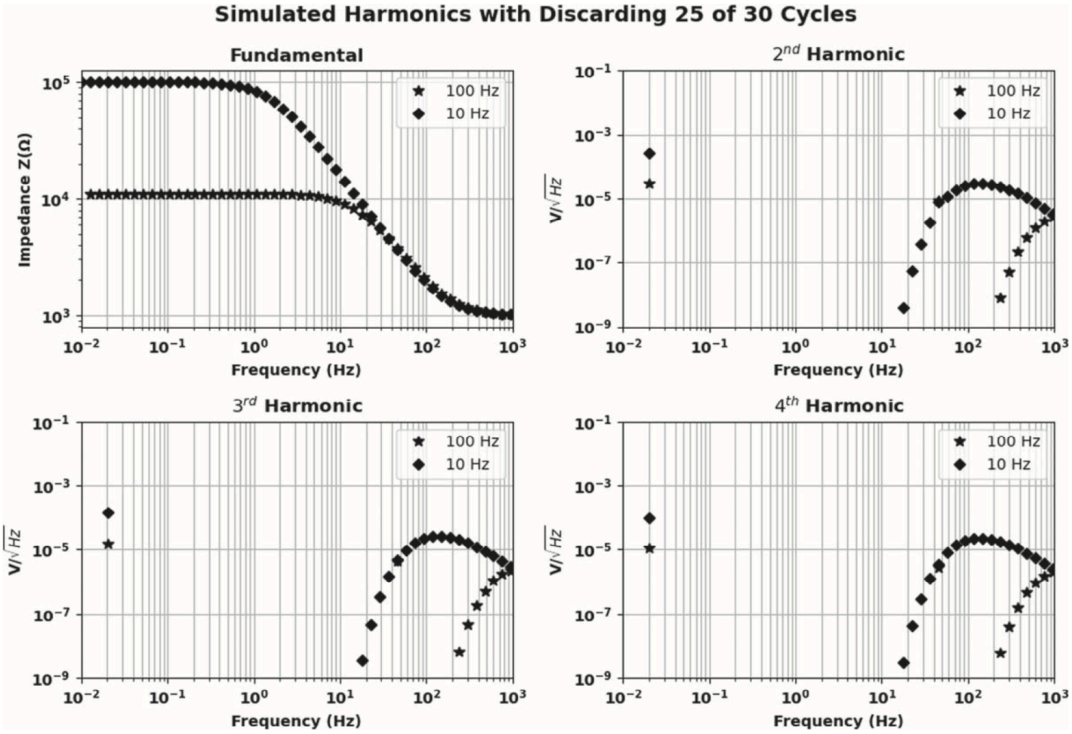

Figure 3.6: Simulated harmonics by measuring 30 cycles and discarding the first 24 of them. *This figure is reproduced with permission.*

results can be trustworthy and evaluated for further analysis.

3.3 Conclusions

In this chapter, the initial transient phenomenon is investigated. The initial transients are always present with real-life measurements, dummy cell measurements, and even simulations based on the dummy cell experiments. Therefore, the initial transients cannot be cleared completely from harmonic analysis. Different measurement scenarios are simulated and also concluded that even with measurements of 30 cycles, the initial transients are present with decreased amplitudes.

Overall, they are resulting from the equations based on the fundamental electric circuit equations and a natural artifact of NHA measurements. In addition, the technical details and codes for the simulations and the NHA measurements are provided in the previous chapters.

Chapter 4

Temperature-Dependent EIS

4.1 Theory and Background

Temperature-dependent EIS is a valuable technique that reveals many important parameters of the battery. The EIS measurements were performed at previously determined temperatures, and acquired spectra were fitted with equivalent circuit elements. These parameters were investigated in terms of their change and magnitude over the temperature array. Kinetic parameters related to charge transfer and electrochemical processes can be extracted with temperature-dependent EIS.

Impedance measurements at different temperatures reveal the resistance and capacitance (usually from CPE) of electrode/electrolyte interfaces (the SEI) and Li oxidation. After obtaining these values, an Arrhenius plot can be derived for each mechanism. In an Arrhenius equation, we can conclude the relation between the resistance and "k" as follows:

$$k = Ae^{-\frac{E_A}{RT}} \quad \alpha \quad \frac{1}{R_{ct}} \tag{4.1}$$

In this equation, k is the rate constant, R_{ct} is the charge transfer resistance, A is the pre-exponential factor, R is the universal gas constant, and T is the temperature in Kelvin. The processes observed with EIS occur on the surfaces or boundaries around the electrodes. Since the Arrhenius relations depend on the transition state theory and the collision theory, the electrode processes yield similar results due to the similar kinetic properties. Therefore, empirically, it is considered as an elementary reaction. Naturally, there is more than one process involved in this mechanism, such as oxidation, solvation, etc., but the overall trend generally follows an Arrhenius relation[60]. In order to obtain activation energy (E_A) in kJ/mol, we need to convert the temperature segment to 1000/T. The logarithm of both sides yields the following:

$$log(k) = log(A) - \frac{E_A(in\frac{kJ}{mol})}{R} * \frac{1000}{T} \tag{4.2}$$

The conversion of resistance to rate constant requires additional terms in this equation. However, these terms do not change the slope of the equation where the activation energy is directly related to the slope. Here, we can introduce the collective multiplier "c" to the equation:

$$log(\frac{c}{R}) = log(A) - \frac{E_A(in\frac{kJ}{mol})}{R} * \frac{1000}{T} \tag{4.3}$$

Lastly, the direct relation between the resistance and the activation energy can

be deduced from the following equation:

$$log(\frac{1}{R}) = log(A) - log(c) - \frac{E_A(in \frac{kJ}{mol})}{R} * \frac{1000}{T} \tag{4.4}$$

A plot of 1/R versus 1000/T can give a linear slope with a negative slope. This negative slope is -E_A/R. As a result, the multiplication of the slope with the negative universal gas constant (R) leads to the activation energy of the process. The data is presented as an Arrhenius plot with a temperature range on the x-axis and 1/R on the y-axis. The fitting software determines the slope, where the data points can be selected according to the linear segments of the data array.

During the discharge of a standard cell, Li-ions are transported after oxidation to the cathode through the formed Solid Electrolyte Interface (SEI) by the electrolyte[61]. The structure and composition of the SEI have a huge impact on the Li-ion transport process [62]. After oxidation, it is proposed that Li-ion goes through SEI by solid-state diffusion, which is then solvated into the electrolyte to be transported to the cathode[63][20]. The reverse process is expected to happen before Li deposition during charging. However, each process's thermodynamic and kinetic details are still under investigation [64]. The effect of each process(diffusion and solvation) on the Li-ion transport is still under debate, and determining contributing parameters requires in-situ operando characterization techniques[65][66][67][68].

The processes mentioned for the metallic Li anode can be studied using EIS. As reported by several studies, the EIS response for these processes shows a high-frequency feature corresponding to the Li-ion transport and solvation followed by

a middle-frequency one for the Li oxidation process[69][70][71][72]. EIS studies show that the Li-ion transport process possesses higher impedance values than Li oxidation[73][74][75].

Further EIS investigations by changing cell parameters, such as temperature and electrolyte compositions, provide more understanding of the nature of these processes and enable the calculations of kinetic and thermodynamic parameters [76][77][60]. The resistance value obtained from the impedance response can be related to the resistance faced by the Li-ion during transport and solvation. The capacitive response can also be obtained, which can be associated with the dielectric properties of the formed SEI. Investigating the changes in the resistance and capacitive impedance response with electrolyte variation and temperature variation provides valuable information about the parameters affecting the operation of the Li battery and sheds light on the nature of the processes.

4.2 Results and Discussion

4.2.1 Symmetric Cell Configuration

This section investigates the anodic and cathodic processes in CR 2032-size batteries with metallic Li electrodes using temperature-dependent EIS for various metallic Li cells. We have published the results of this study in 2024[41]. We assemble Li/Li symmetric cells with three different electrolytes and study the change in impedance and the activation energies of the Li-ion processes. We also do temperature-dependent EIS combined with aging tests to understand the

changes in the SEI with the operation. Finally, we compare the Li/Li symmetric result with Li/MnO_2 battery to observe the change in impedance response and identify the limitation of EIS in studying such processes.

Li/Li symmetric cells were assembled under an argon-filled glovebox. The two electrode cells were composed of two electrode-grade Li metal chips and a Celgard PP separator. The diameter of the electrodes was 15 mm, with a capacity density of 1.8 mAh/cm^2. As a result, the total capacity of battery-type cells was 3.2 mAh. The electrolytes used were as follows:

1. 1M $LiPF_6$ in EC-DEC (1:1, v/v)
2. 1M $LiPF_6$ in EC-DMC (1:1, v/v)
3. 1M $LiPF_6$ in EC-EMC (7:3, v/v)

In these chemical compositions, EC is ethylene carbonate, DEC is diethyl carbonate, DMC is dimethyl carbonate, $LiPF_6$ is lithium hexafluorophosphate, and EMC is ethyl methyl carbonate. Li/MnO_2 cells were assembled using the same method, replacing one of the Li metal chips with a commercially obtained (from Sigma-Aldrich) MnO_2 electrode.

The effect of temperature on the symmetric sample impedance can be seen in Figure 4.1, which shows the impedance response of each cell from 1MHz to 1Hz at two different temperatures (15 and 55 °C). In all cells, there is a distorted semicircle response, which is assumed to result from the interfacial process of metallic Li electrodes. At lower temperatures, in this case, 15°C, the semi-circle is significantly larger than at higher temperatures, indicating the large charge

transfer resistance of the interfacial process dominating the response. This interfacial impedance response is assumed to include the processes of Li-ion transport after Li oxidation. In the literature, the processes are suggested to be solid-state diffusion through SEI and solvation into the electrolyte[78][79]. Separating each process in the impedance response is hard, if not impossible, since the data is very convoluted. However, we will refer to this response as Li-ion transport, which is directly related to the structure/composition of the SEI and the solvation of the Li-ion. The solvation process is assumed to be similar in all the cells since the Li salt type and concentration are identical in all the cells. Therefore, the variation in the impedance response can be concluded to result from the transport through SEI.

The formation of the SEI will be different for each electrolyte composition. In our study, we used three solvent compositions, which will have different reactions with the electrode surface, resulting in the formation of SEI with somewhat different properties. From Figure 4.1, the EC-DMC symmetric cell shows the largest resistance among the three electrolytes, followed by EC:EMC and EC:DEC. This high charge transfer resistance can be related to the effect of larger strain in Li-ion transport. It may result from a more compact SEI structure in the EC-DMC cell or higher interaction with the SEI component during transport[80]. This trend is also observed in the high-temperature Nyquist plot, where the greatest impedance value belongs to the EC-DMC and the lowest to EC:DEC. It should be noted that these results are for pristine cells. The SEI was formed by the direct reaction of metallic Li with the electrolyte before any charge or discharge current.

The results obtained from symmetric cells showed the large and dominating

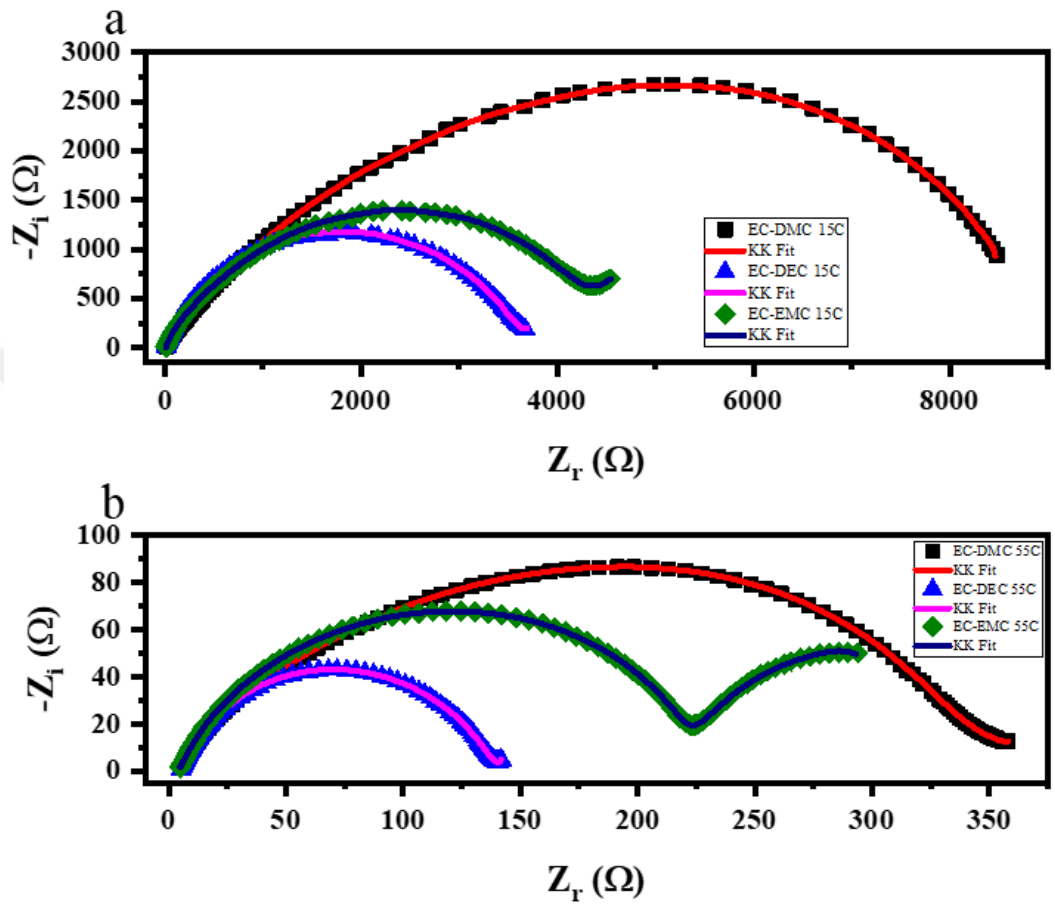

Figure 4.1: Impedance responses of symmetric Li/Li cells with different electrolyte compositions at 15°C (a) and 55°C (b).

impedance response for the interfacial processes of metallic Li anode. The same response is expected to be observed in any cell that uses metallic Li in the anode unless the cathode impedance is larger. To distinguish the effect of the cathode on the impedance response and to investigate the possibility of observing the metallic Li impedance response in the presence of the cathode, we performed the same measurements on Li/MnO_2 cell, which can be seen in Figure 4.2. The Nyquist plots show a large distorted semicircle at the high-frequency region, which is assumed to be from the metallic Li anode interfacial processes. Other semicircles

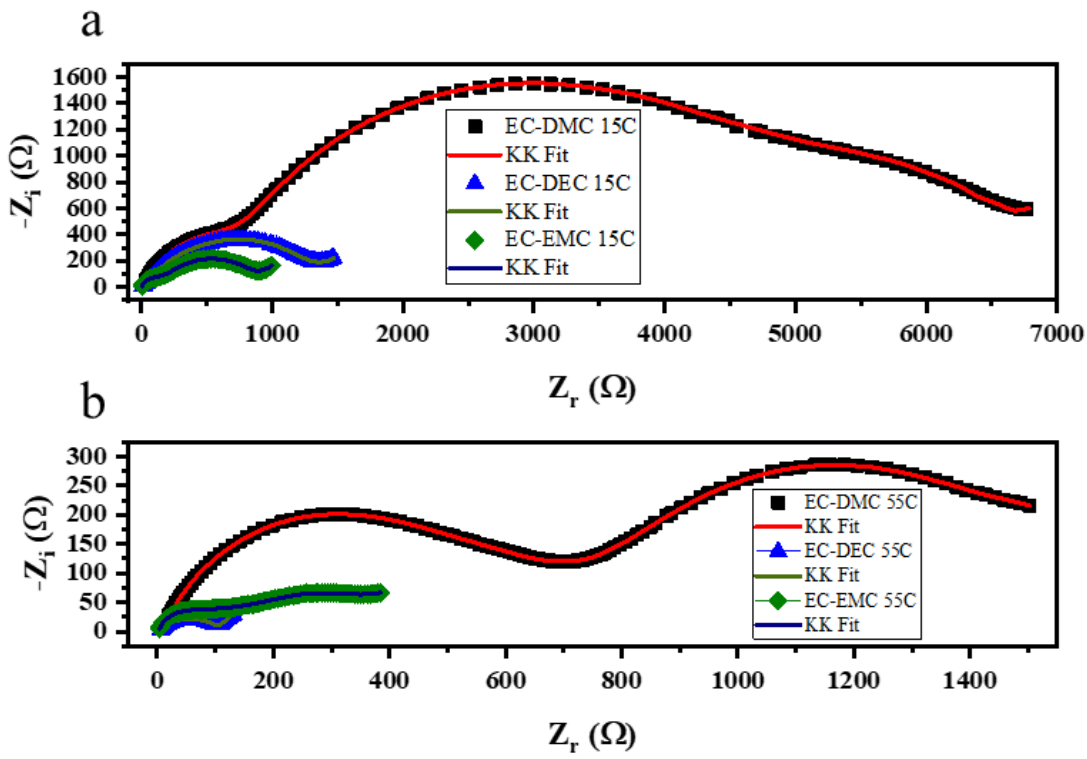

Figure 4.2: Impedance responses of battery-type cells with different electrolyte compositions at 15°C (a) and 55°C (b).

appear as well, which can be related to the cathode. The first is a small semicircle at a very high-frequency region, and the second is a semicircle at low frequencies. The high-frequency semicircle is related to the current collector, and the low frequency is to the cathode[81][82][83]. These semicircles are clearly observed for EC:DMC Nyquist response. An example illustrative can be seen in Figure 4.3.

To observe the effect of cell cycling on the discussed interfacial/cathode processes, the cells were cycled with constant current, and the impedance was measured after several cycles. The symmetric cells were aged with 28 μA/cm^2 current for 30 minutes in alternating directions. The total amount of aging was 10 of these cycles, which took about 10 hours. As for the battery-type cells, the aging was

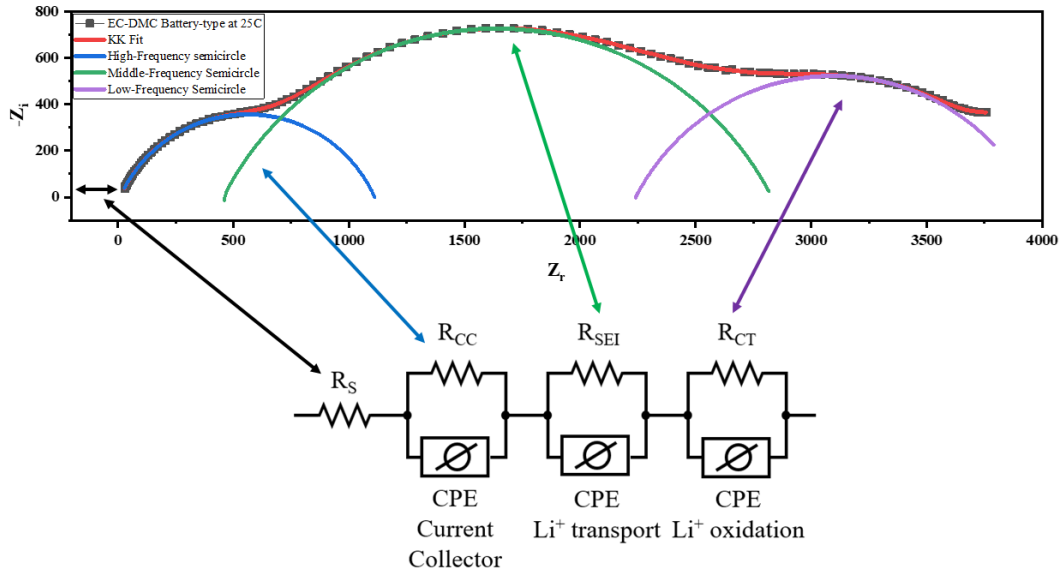

Figure 4.3: Nyquist plot of EC-DMC battery-type cell and the semicircle representations.

done by withdrawing 28 μA/cm^2 for 6 hours. Figure 4.4 shows the Nyquist plots of both pristine and aged for both symmetric Li/Li and Li/MnO_2 cells. As can be seen, there is a large decrease in the impedance values as the cells are aged. In a study by Li et al., the aging mechanism was explained as the formation of predominantly Li^+-EC pairs on the metallic Li anode[84]. Similarly, Andersson and co-workers showed the formation of Li_2CO_3 and lithium alkyl carbonates on the metallic Li anode with XPS[85].

Consequently, processes such as charge transfer resistance depend on the kinetics of this pair on the SEI. Furthermore, a decrease in resistance upon cycling the cells was also observed in a reported study by Zhang et al. [86]. The study suggests that the resistive layer forms when the cells are assembled. After cycling, the ionic conductivity of the SEI layer improves significantly and reduces the measured impedance[87].

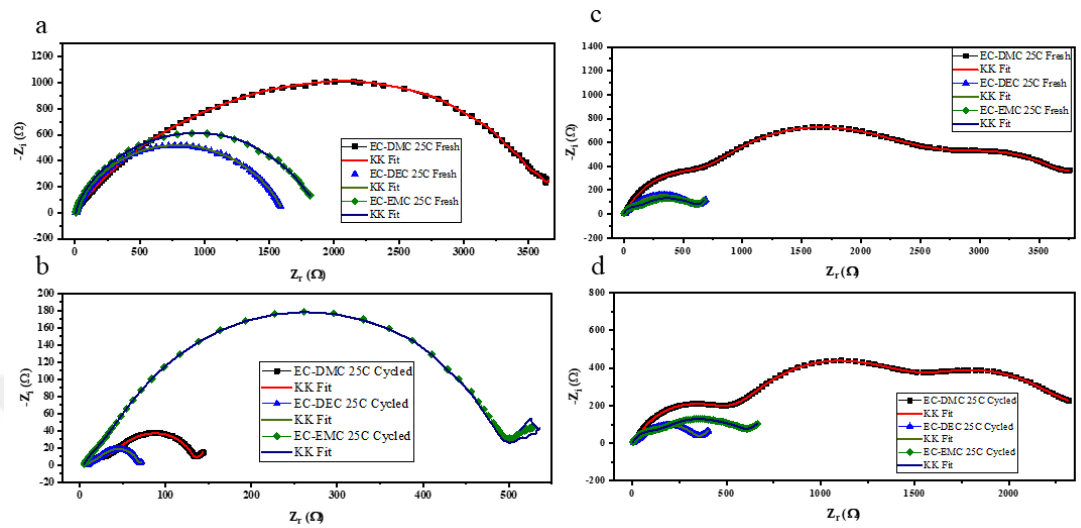

Figure 4.4: Nyquist plots of symmetric pristine (a) and aged (b) samples, and battery-type pristine (c) and aged (d) cells.

In conclusion, these results highlight that the assembly of symmetric cell configuration enables the isolation of individual electrode processes and the sole observation of the effect. Thereafter, the battery-type configuration results expressed the complete cell and contribution of each process. Lastly, the effect of aging and its impacts on the SEI layer has been observed and evaluated based on the temperature-dependent EIS.

4.2.2 Aging and Cycling Estimations based on Symmetric Cells

This section is part of an ongoing project with our collaborators from Wuhan University in China. We are investigating the effect of aging and cycling via temperature-dependent EIS, similar to the previous section. The cells are the

same size in this section as well, CR2032 size, and made of the following configurations:

1. Li-Li with 1M $LiPF_6$ in DMC:EC:EMC (1:1:1, v/v/v)
2. LFP-LFP with 1M $LiPF_6$ in DMC:EC:EMC (1:1:1, v/v/v)
3. Li-LFP (battery-type) with 1M $LiPF_6$ in DMC:EC:EMC (1:1:1, v/v/v)

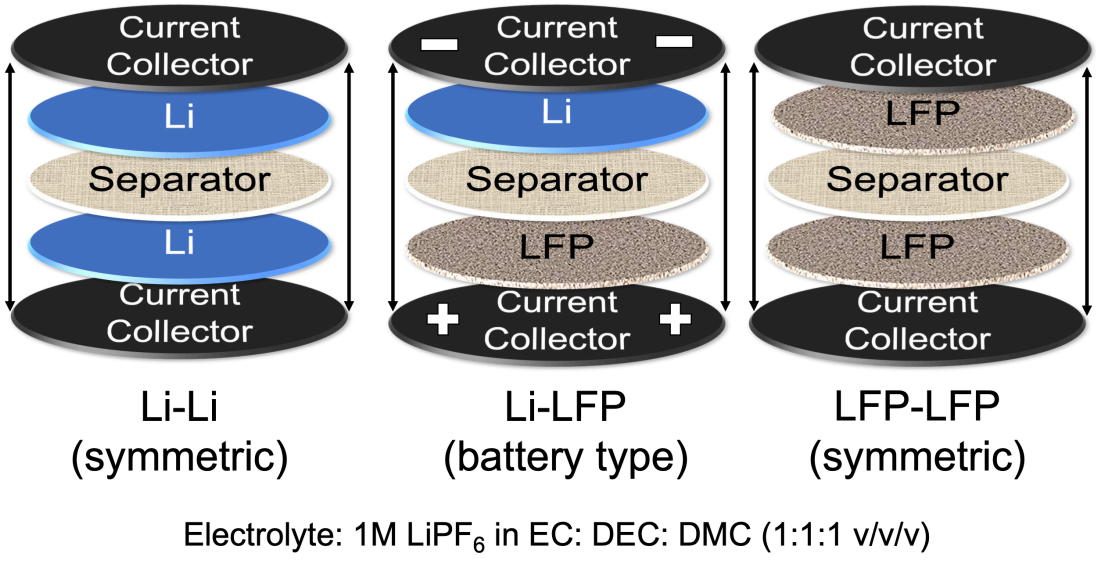

Figure 4.5: Illustration of the cell architectures with different electrode configurations.

Based on the recommendation of our collaborators, these cells were subjected to a current rate of C/2. Information regarding the battery-type capacity is around 3 mAh. Therefore, the cells were cycled with a 1.5 mA current. The symmetric configuration samples were cycled with this current rate for 30 minutes in both directions. This whole charge-discharge process was repeated 50 times.

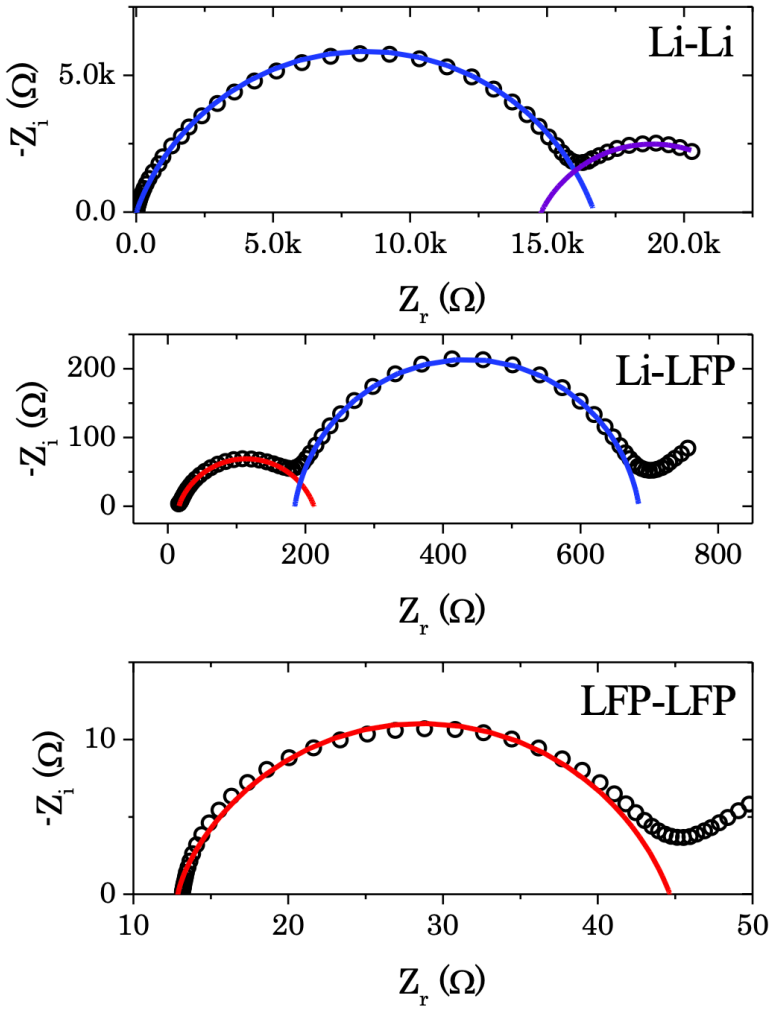

Figure 4.6: The Nyquist plots of each cell architecture at -20°C. The plots belong to Li-Li (top), Li-LFP (middle), and LFP-LFP (bottom) cells.

In Figure 4.6, the semi-circles of the electrodes can be seen. The shades of blue are from the Li electrode, and red/orange colors are due to the LFP electrode. In addition, the battery-type cell exhibits semi-circles from both geometries.

The assignments of these semi-circles on the battery type originate from the symmetric cells. The purpose of building and measuring symmetric cells is to isolate and evaluate the electrode types individually. This method provides valuable

information about the processes occurring on each electrode. Furthermore, the time constants of each process can be calculated and utilized in further analysis.

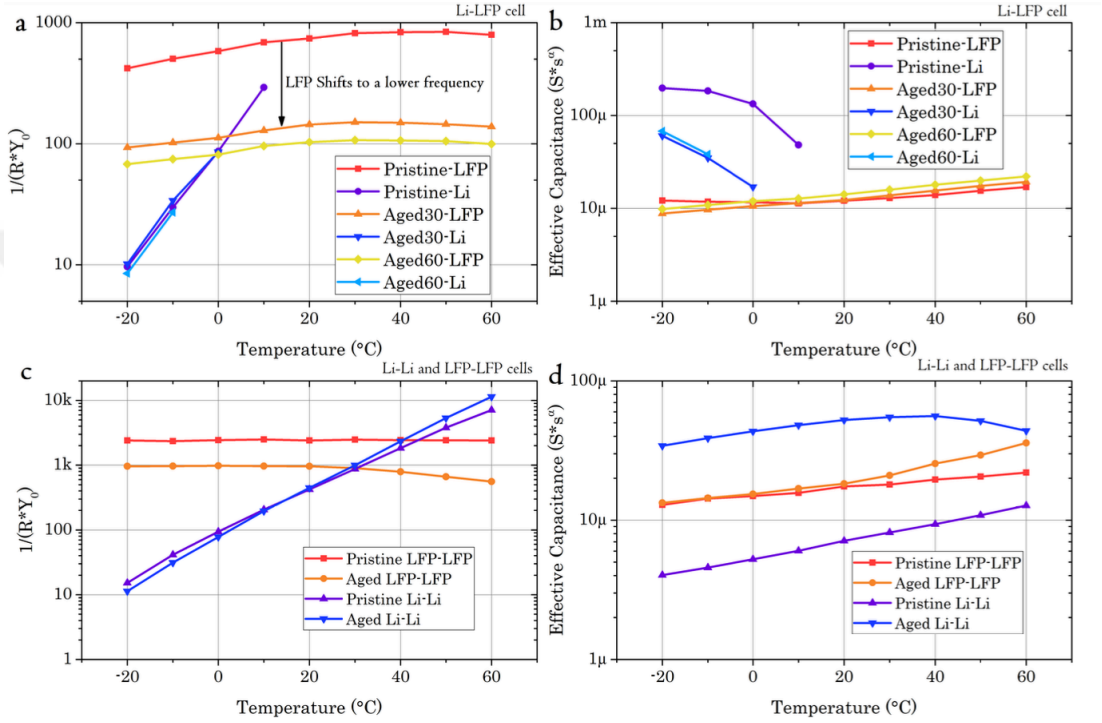

Figure 4.7: 1/RC values of battery-type (a) and symmetric architectures (c). Similarly, the effective capacitances of battery-type (b) and symmetric cells (d) are plotted over the temperature range between -20°C and 60°C.

Temperature-dependent EIS comes in extremely handy for analysis situations like this. By measuring the impedance at various temperatures, critical processes such as charge transfer or SEI properties can be investigated. As seen in Figure 4.7, 1/RC values of each process are calculated and plotted in both aged and pristine conditions. For symmetric samples, only the charge transfer resistance is observed and evaluated in the measurement frequency range, which is 100 kHz to 0.1 Hz. On the other hand, the battery-type cells exhibit two different semi-circles, as seen in Fig. 4.6 (middle panel). The identification of these semi-circles is performed by investigating the 1/RC data of symmetric cells. It is clear that

the Li process occurs at a lower frequency than the LFP, based on the data in Fig. 4.7 (c). Therefore, the high-frequency semi-circle observed in the battery-type cells belongs to the LFP processes. Similarly, the lower frequency semi-circle is from the Li electrode, which is a lot more temperature-dependent than the LFP electrode.

First of all, the 1/RC values of Li processes (blue or purple lines) remain constant while the LFP processes shift to a lower value as the samples are cycled. Therefore, the cycling affects the LFP electrode more than the Li electrode in terms of kinetics. This 1/RC value decrease may originate from the volume changes of LFP during intercalation and de-intercalation processes and SEI properties on the electrodes[88]. On the other hand, the Li electrode has consistent 1/RC values, which are only dependent on the temperature but not on cycling. The purple and blue lines mostly overlap in both symmetric and battery-type 1/RC plots in Fig. 4.7 (a) and (c). As a result, proper separation and investigation of LFP processes can yield information about the cycling of the cells.

Secondly, the semi-circles merge in the battery-type cells after a certain temperature, as seen in Figure 4.8. In order to follow the 1/RC values of this situation, Figure 4.7 (a) should be investigated. As the temperature increases in battery-type cells, the 1/RC values of Li and LFP get closer. After a certain temperature, these two values overlap and become inseparable. Since the Li is a lot more temperature-dependent, at elevated temperatures, Li semi-circles become significantly smaller than the LFP semi-circles. Therefore, the Li processes can only be observed at lower temperatures where the LFP and Li processes are observed separately.

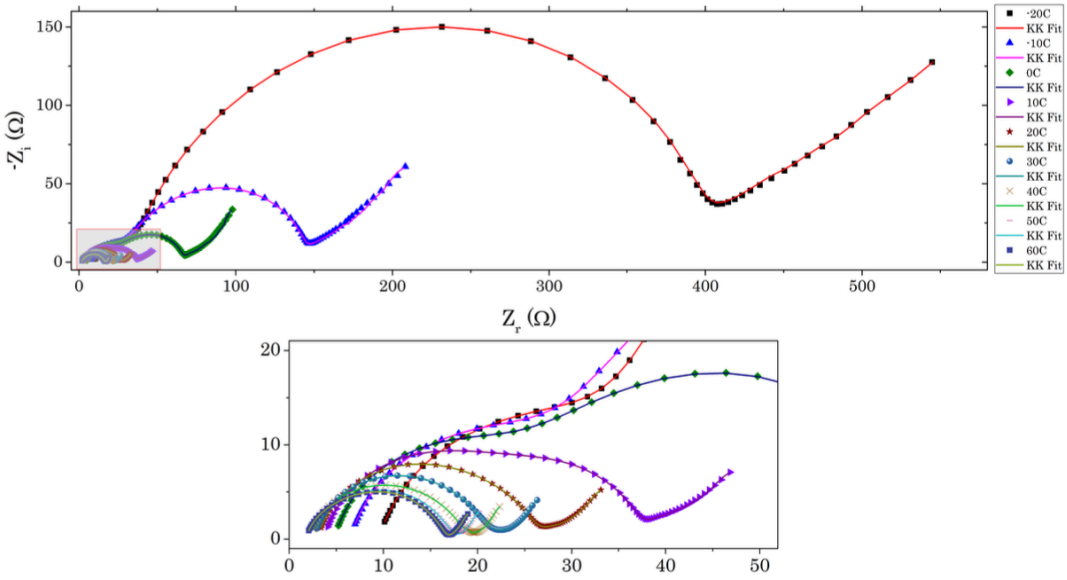

Figure 4.8: Nyquist plots of Li-LFP (pristine) battery-type cells at different temperatures.

Thirdly, the effective capacitance values (from CPE of equivalent circuit fit) are investigated and utilized for the evaluation of the capacitance properties of the electrodes. In this investigation, the LFP electrodes have temperature and cycling-independent capacitance values, whereas Li is severely affected by the cycling. At a certain SoC or a cycling number, the capacitance values do not change noticeably for both electrodes. These results also confirm and explain the 1/RC changes alongside the resistance values.

The resistance values obtained from these equivalent circuit fits can then be used for the calculation of the Activation Energies via Arrhenius relations. Since the Li electrode has a more temperature-dependent impedance response, it is expected to have a greater activation energy. The overall Arrhenius plots can be seen in Figure 4.9. The battery-type cells only exhibit a few Li-related data

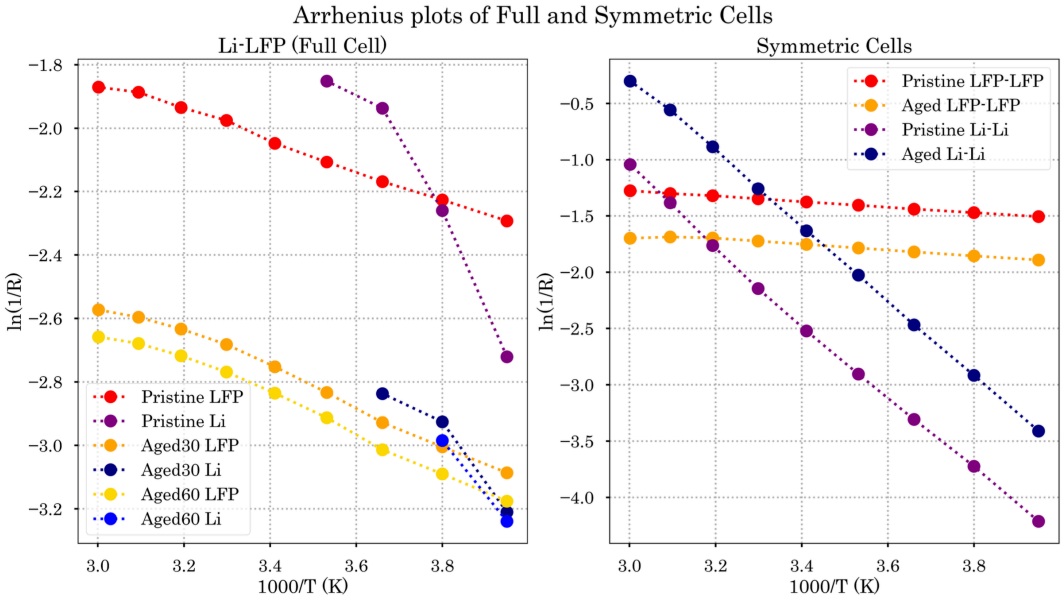

Figure 4.9: Arrhenius plots of battery-type (Full Cell) and Symmetric configurations at pristine and aged states.

points at the colder end of the temperature range due to the merging with the LFP. Therefore, the activation energy of these processes can only be calculated from these data points and should be evaluated more carefully. This is why experiments with symmetric cells are necessary for the correct identification and analysis of complete batteries.

The linear fit on these Arrhenius plots gives the activation energies of each process. The values can be seen in the Table 4.1.

Battery-type Samples	Li E_A (kJ/mol)	LFP E_A (kJ/mol)
Pristine	59.1 ± 4.2	13.2 ± 3.8
30 Cycled	35.8 ± 5.5	10.4 ± 4.2
60 Cycled	31.6 ± 2.5	9.3 ± 2.7

Table 4.1: Activation energies of battery-type samples at various cycled states.

The activation energies of Li semi-circles are considerably higher than the LFP

processes, as seen in Table 4.1 and Figure 4.9. The high sensitivity towards the temperature yields this greater activation energy in Li, which implies the charge transfer resistance has a greater activation energy and temperature sensitivity. On the contrary, LFP processes yield a stable activation energy, which shows a slight decrease as the batteries are cycled. The effect of aging on the Li side is difficult to comment on since there are only a few available data points, and the values show a significant decrease. As a result, these Li activation energies are suspicious, and symmetric configuration results should be considered for a better analysis.

Symmetric Samples	E_A (kJ/mol)
Li-Li Pristine	62.5 ± 2.2
Li-Li Aged	62.1 ± 1.8
LFP-LFP Pristine	4.9. ± 2.2
LFP-LFP Aged	4.8. ± 1.6

Table 4.2: Activation energies of Li-Li and LFP-LFP symmetric cells at pristine and aged conditions.

Overall, the activation energies of symmetric cells do not show any significant change. Li processes have around 62 kJ/mol, and LFP processes have 4.9 kJ/mol activation energies in both aged and pristine conditions. There is no expected change since the measured processes do not have any aging factor in terms of their activation energy. The semi-circles are assigned to the charge transfer resistances, and they should not change upon cycling.

In Figure 4.10, a Bode plot of a battery-type cell can be seen. As highlighted with the blue line, the peak position of the LFP semi-circle shifts, which is also confirmed by the 1/RC plot of Fig. 4.7 (a). Therefore, the investigation can be focused on the LFP process during the aging and capacity investigation.

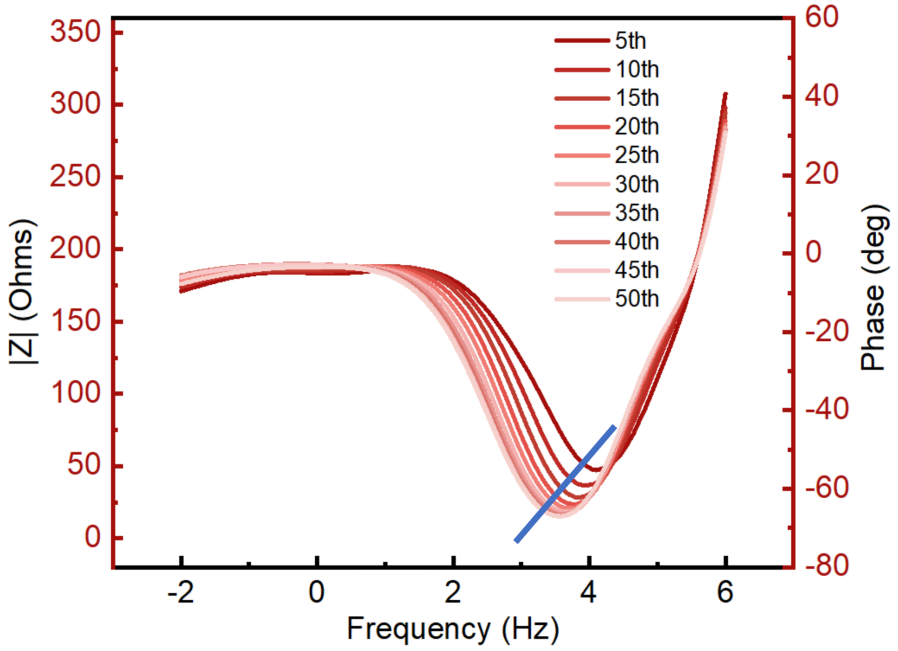

Figure 4.10: Bode plot of a battery-type cell at different cycle counts. This plot was taken with permission from our collaborators.

Herein, a quick and precise method for the estimation of the capacity and cycle count is proposed. As seen from the data above, the 1/RC value of LFP shifts to a lower frequency as the cells are aged. Additionally, the LFP processes occur at a higher frequency than the Li processes, which can be measured with a quicker impedance scan. Temperature plays a role in the observation of Li semi-circles in battery-type cells; however, the LFP semi-circle is always observed at the experimental temperature interval.

For a deeper investigation, an experimental sequence was written as follows:

- This cycle is repeated 60 times.
    - 10-minute waiting period.
    - two consecutive EIS scans.

- CC discharge at 0.5 C until 2.5 V.

- CCCV charge until 4.2 V with 0.5 C, finish at 0.1 C.

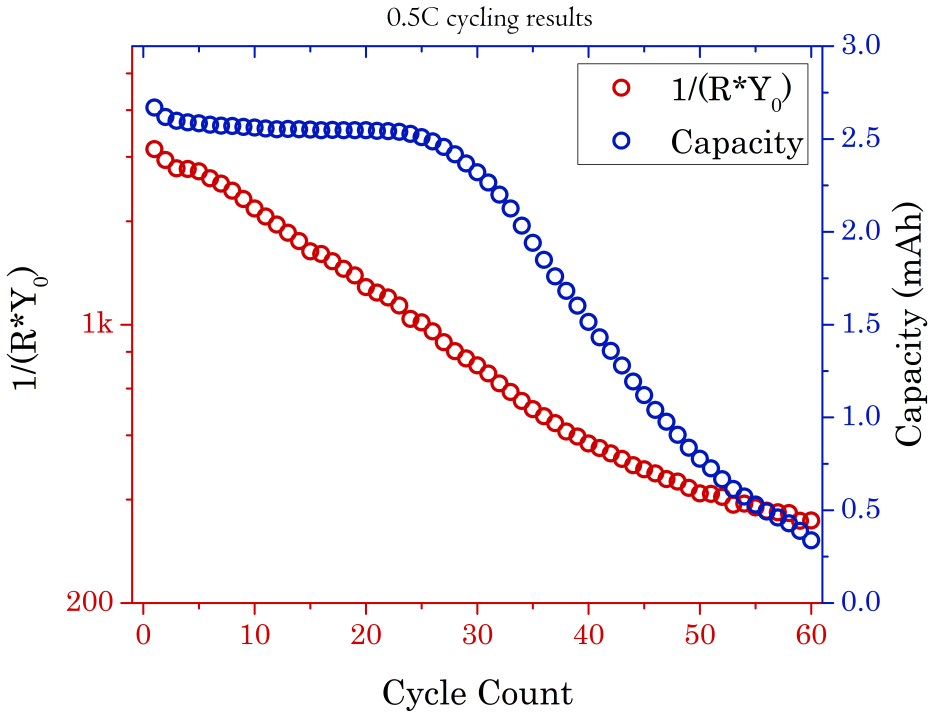

Figure 4.11: 1/RC and capacity values of a battery-type sample measured with 0.5C for 60 cycles.

The results of this experiment can be seen in Figure 4.11. 1/RC values show a gradual decrease, indicating that the mechanism of LFP is slowing down as the battery is cycled. The capacities are calculated from the CC discharge data. For this battery architecture, the capacity can be preserved until 25 cycles with a 0.5 C rate. Thereafter, the capacity quickly decreases and reaches around 10% of the initial capacity at around 60 cycles. Obviously, this drastic capacity loss is not applicable in real life, where only a high capacity from the batteries is accepted. For many (mobile and portable devices) batteries, 80% of the initial capacity is the lower limit of a health operation lifetime. When the capacity decreases by 80% of the initial capacity, battery replacement is recommended.

Between cycles 5 and 30, the capacity remains more or less constant while the 1/RC value decreases. For this battery specifications, the 1/RC value can provide information regarding the cycle life and capacity. By measuring the impedance quickly at high frequencies, one can have a solid idea about the status of the battery and make further decisions related to the battery.

Overall, this section highlights a quick EIS measurement method for the capacity and cycle count determination. It is shown that the symmetric cells enable the separation of individual electrodes and the characterization of a battery-type (whole cell) structure. The assignment of features from a battery-type cell is difficult since it is unknown which part of the cell generates the features.

4.2.3 Bobbin vs. Spiral Li/$SOCl_2$ Batteries

Extensive characterization of lithium thionyl chloride batteries is necessary for performance evaluation, design optimization, safety regulation, and device compatibility. A typical thionyl chloride battery has a metallic lithium anode, a carbon cathode with a porous structure, a non-aqueous $SOCl_2$:$LiAlCl_4$ electrolyte, and a polymer separator[89][90]. Thionyl chloride has a unique role as both the cathode-active material and the solvent for the electrolyte.

The anodic reaction:

$$Li \rightarrow Li^+ + e^- \tag{4.5}$$

The cathodic reaction:

$$2SOCl_2 + 4Li^+ + 4e^- \rightarrow 4LiCl + S + SO_2 \tag{4.6}$$

And the overall reaction of thionyl chloride batteries:

$$2SOCl_2 + 4Li \rightarrow 4LiCl + S + SO_2 \tag{4.7}$$

As a result, the open circuit potential of a thionyl chloride battery is around 3.6 V. The stable discharge voltage is due to the physical state of the reactants and the products. In the overall reaction, all of the species are in either solid or liquid form, and SO_2 produced is dissolved in the electrolyte. The concentration of SO_2 in the electrolyte depends on the SoC and the operation conditions of the battery. Additionally, many thionyl chloride batteries have ventilation mechanisms near

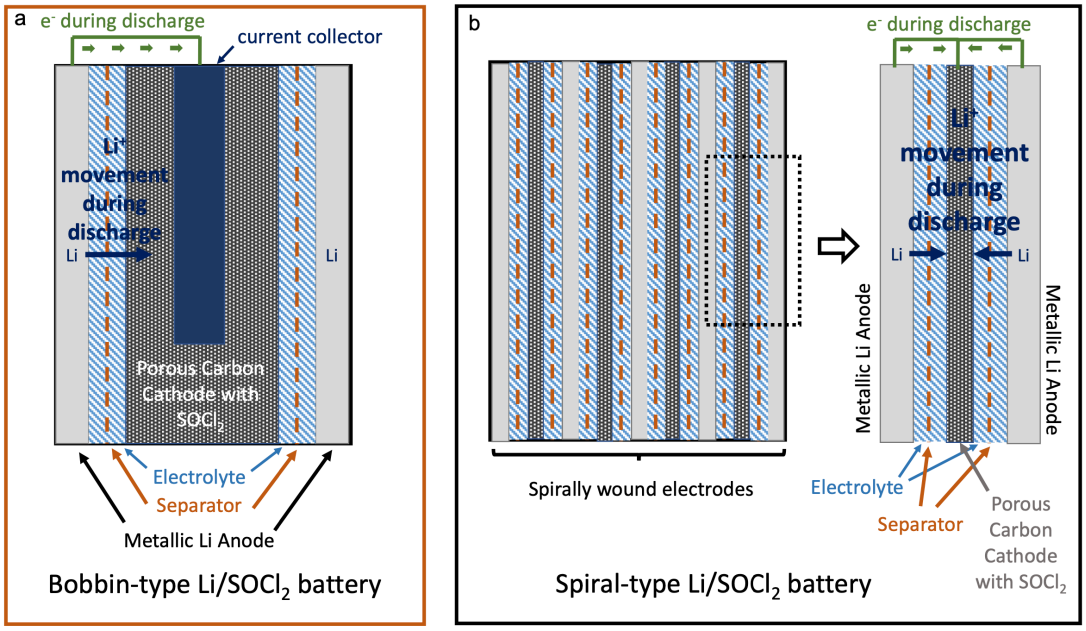

Figure 4.12: Illustration of ion and electron movements in the bobbin (a) and spiral (b) geometries of $Li/SOCl_2$ batteries.

the positive terminal to prevent extreme pressures. Therefore, the Nernst equation for the complete cell does not have any concentration-dependent logarithm component throughout the cell operation. Additionally, the solid-electrolyte interface (SEI) is formed on the metallic Li anode. The reaction between the anode and thionyl chloride generates a stable, non-conductive interface (LiCl), resulting in an extended shelf-life[89].

Lithium thionyl chloride batteries come in various sizes and architectures. They can be either in AA, A, C, or D sizes as cylindrical structures and bobbin or spiral geometries[89]. Spiral and bobbin-type originate from the power and capacity requirements of the application. The spiral structure has a greater electrode surface area. Thus, it can provide higher amounts of current. The downside is the reduced electroactive material amount due to the space occupied by the

spirally wounded electrodes. On the other hand, the bobbin-type batteries have stacked electrodes with smaller surface area but with higher $SOCl_2$ (electroactive material) amount. As a result, its capacity is higher than the spiral, but peak and continuous current limits are lower than the spiral type. An illustration of the two architectures can be seen in Figure 4.12.

SAFT C-size spiral (LSH 14, 5.8 Ah) and bobbin (LS26500, 7.7 Ah) batteries are measured to investigate the difference between the spiral and bobbin architectures. $Li/SOCl_2$ chemistry has a large operating temperature window, from -60°C to 150°C. Another unique feature of this chemistry is the highly stable passivation layer on the metallic Li anode. It is formed instantly during manufacturing when metallic lithium contacts the $SOCl_2$. Therefore, this passivation layer should have cracks or pores for Li^+ to move through during the operation. To form these cracks, a current withdrawal is just before the EIS measurements are done. The purpose is to form cracks on the SEI layer and generate passages for Li^+ movement. Similarly, these SEI cracks should be present during the EIS measurement. As a result, the EIS measurements have a negative DC offset, and the current is always in a withdrawing state. Charging currents on these batteries causes undesired side reactions and should be strictly avoided.

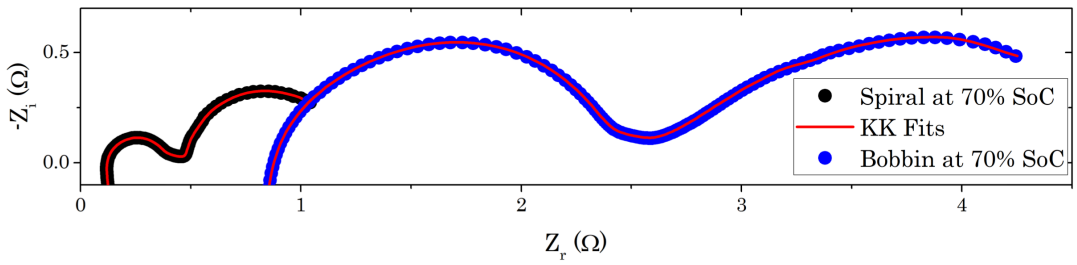

Figure 4.13: The EIS response of spiral and bobbin architectures at the same experimental conditions.

The impedance responses of the two architectures can be seen in Figure 4.13. Although they yield quite different impedance responses, the two batteries have the same chemistry, electrolyte, separator, and size. Therefore, to investigate the origins of this difference and identification of the electrochemical processes inside the batteries, a detailed look through the EIS response should be made.

In Figure 4.14, the two impedance responses can be compared. The equivalent circuits for these batteries are identical since the chemistry and electrochemical processes that govern the batteries are the same. These processes include Li^+ transport through the solid electrolyte interface (SEI) at high frequency (around 5-10 kHz), Li oxidation process at around 30-40 Hz, and cathodic charge transfer and LiCl adsorption processes around 20-40 mHz. These processes can be observed as the semi-circles on the Nyquist plots, and in a previous publication of our group, similar observations regarding the $Li/SOCl_2$ batteries have been made[91].

The two architectures yield a few differences in terms of impedance response. First of all, the high-frequency R_S (solution or series resistance) is greater in the bobbin type. This is due to the higher amounts of electrolyte and the larger distance between the anode and the cathode. Similarly, the overall impedance magnitude in bobbin is higher. This result is also expected and in good agreement with the purpose of each geometry. The spiral type is designed to provide higher currents, so having a lower impedance results in more energy efficiency during operation. Additionally, the bobbin type has a greater Li^+ transport semi-circle, and we shall see that there is also a feature coming from the current collector. As a result, this charge transfer process is also affected by the battery architecture. Moreover, the spiral type has well-defined semi-circles, while the bobbin has a

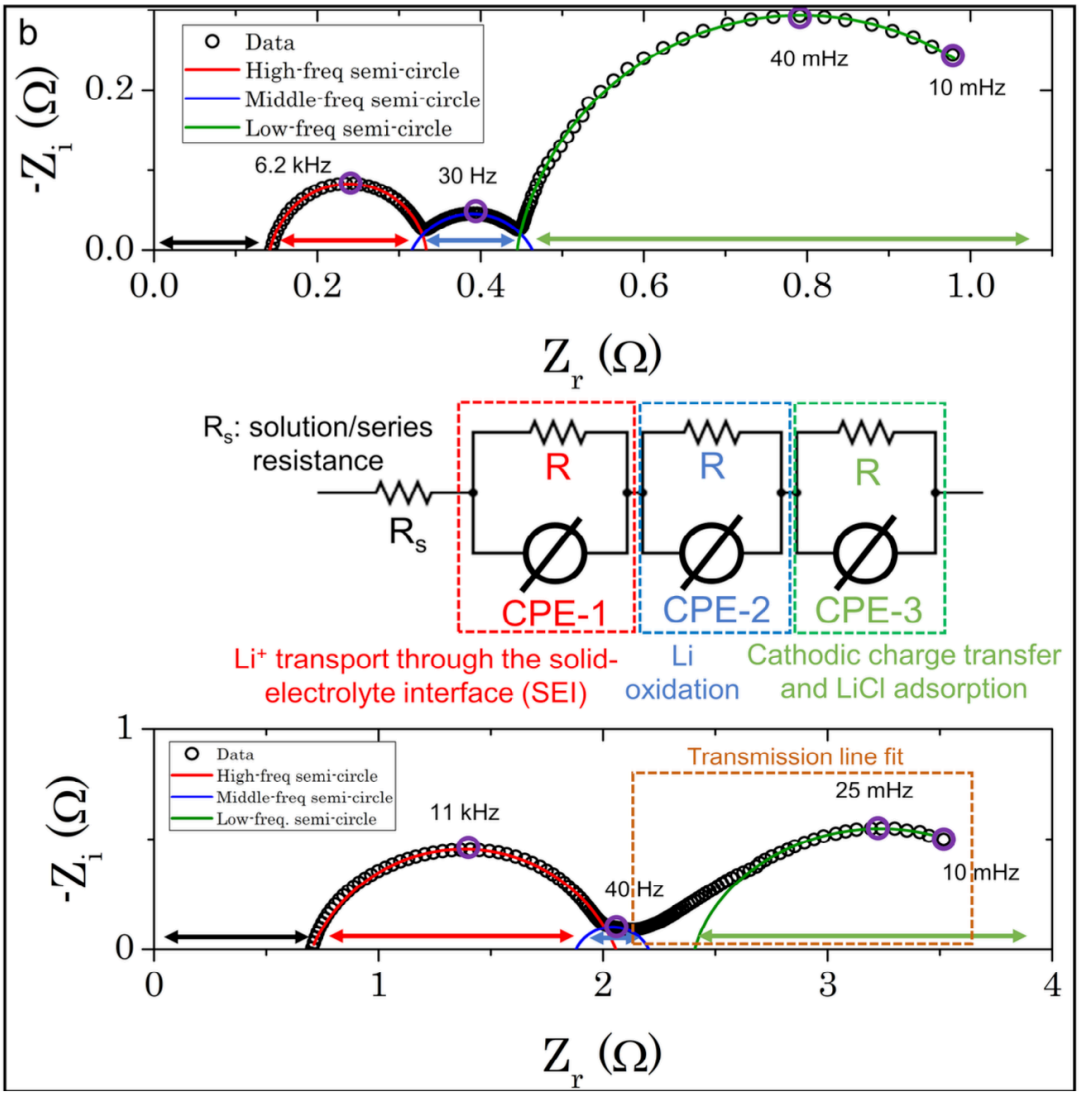

Figure 4.14: Nyquist plots of spiral (upper) and bobbin (lower) types of $Li/SOCl_2$ batteries. Additionally, the equivalent circuit fit model for both chemistries, alongside the region, indicates the transmission line for the bobbin type.

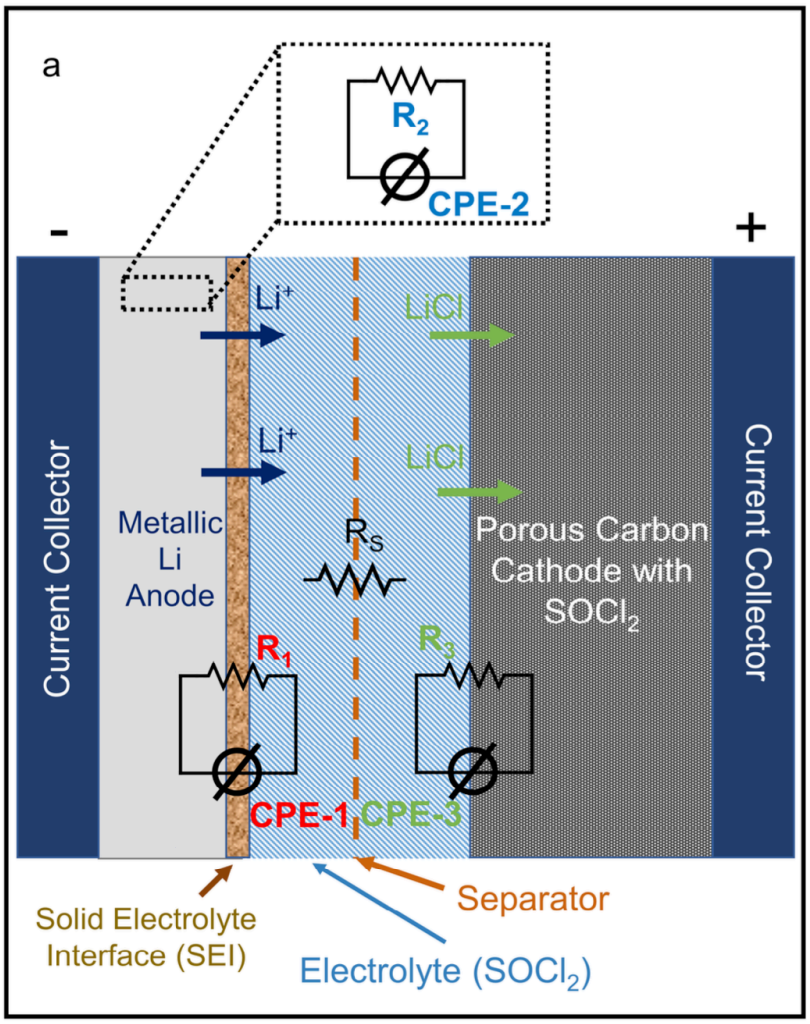

Figure 4.15: The equivalent circuit elements of a Li/$SOCl_2$ battery. Each R-CPE element represents a process, and they are positioned in the place of the process.

linear-like segment at lower frequencies. Due to the geometry difference, mass transport is the limiting factor in the bobbin type, whereas smaller distances of the bobbin type do not yield such results.

In the equivalent circuit modeling of the cells, a series resistance is used to model the solution resistance and cable/connection resistances. The calibration of the potentiostats can eliminate the instrumental artifacts, and only the battery-related resistances can be measured and modeled. Moreover, the high-frequency

semi-circle is located on the anode/electrolyte interface where the infamous SEI layer is present. This SEI layer is a critical property of $Li/SOCl_2$ batteries, and experimental requirements should be met to measure the cells properly. In addition, Li oxidation occurs on the metallic Li anode and is placed on the anode accordingly in Fig. 4.15. Lastly, the cathodic charge transfer and LiCl adsorption are placed on the electrolyte/cathode boundary. Furthermore, this part is also modeled with a transmission line in bobbin type, which will be discussed in later parts.

The batteries also yield different impedance responses throughout a temperature range. Electrochemical processes are affected by temperature, and as we shall see, some processes are more sensitive than others. A comparison between the two can be seen in Figure 4.16 below.

Firstly, the solution resistance in both geometries shows a difference as the temperature increases. The bobbin type has a distinctive decrease, whereas the spiral type has little to no change. This is due to the amount of electrolytes in the cells, while the bobbin type has higher amounts of electrolytes and a larger distance between the electrodes. Moreover, the high-frequency semi-circle is more temperature-dependent in the spiral case. At elevated temperatures, it becomes significantly small, and cathodic processes become the limiting process. On the other hand, the bobbin type has a persistent semi-circle at elevated temperatures and becomes temperature-independent. However, this semi-circle should not only be attributed to the charge transfer. There is another physical feature called the current collector, which comes from the steel housing of the cell and the contact between the anode and the container. The resistance and capacitance of this layer are due to contact between the steel and metallic Li.

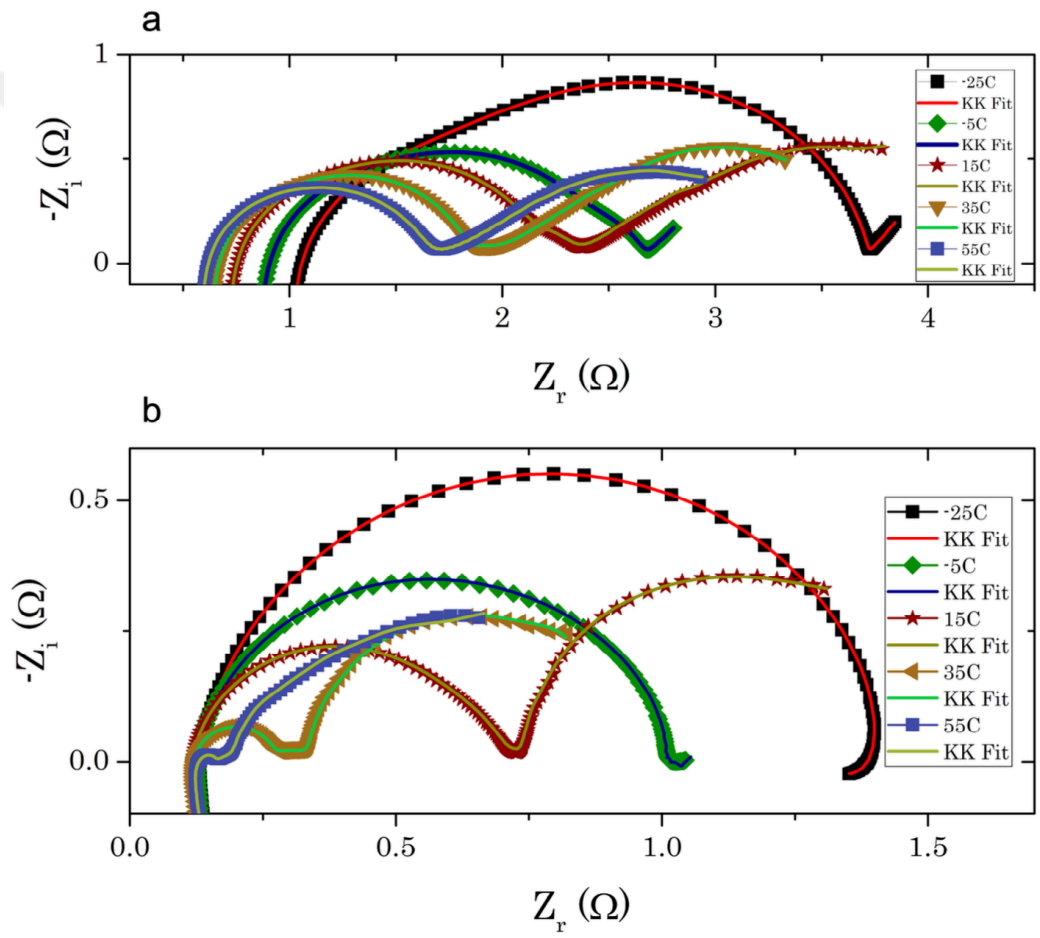

Figure 4.16: Temperature-dependent EIS results of the bobbin (a) and spiral (b) types at various temperatures.

Secondly, the Li oxidation is observed in both geometries at certain temperatures. It has a relatively smaller impedance and semi-circle. Therefore, the observation is not possible at low temperatures due to the domination of charge transfer semi-circle. Besides, it has a slight temperature dependency, which will be analyzed in later discussions.

Thirdly, the cathodic charge and mass transfer occur on the porous carbon cathode, and a representative semi-circle appears at the lower frequency region. Similar to the current collector semi-circle, it shows weak temperature dependency. Furthermore, the sizes and shapes of semi-circles are different in each geometry, which indicates that the mass transfer properties can affect the impedance response for this process.

Another important point is the SEI process. In the spiral case, this semi-circle continuously decreases as the temperature rises. On the other hand, the semi-circle does not change after 25°C for the bobbin type. The spiral case is a consequence of the large surface area of the electrodes and the SEI layer and charge transport through this layer is dominating at all temperatures. Meanwhile, the surface area of the bobbin is not as large as the spiral; thus, the semi-circle merges with the current collector, and the observed semi-circle (which is from the current collector) remains constant at elevated temperatures. In light of this information, further analysis with time constants (or 1/RCs) and capacitance values should be done to differentiate the processes more clearly.

Time constants or 1/RC values, as explained in the symmetric battery study above, can provide details about process kinetics. Moreover, the capacitance values of the same processes can further elaborate the surface properties, such

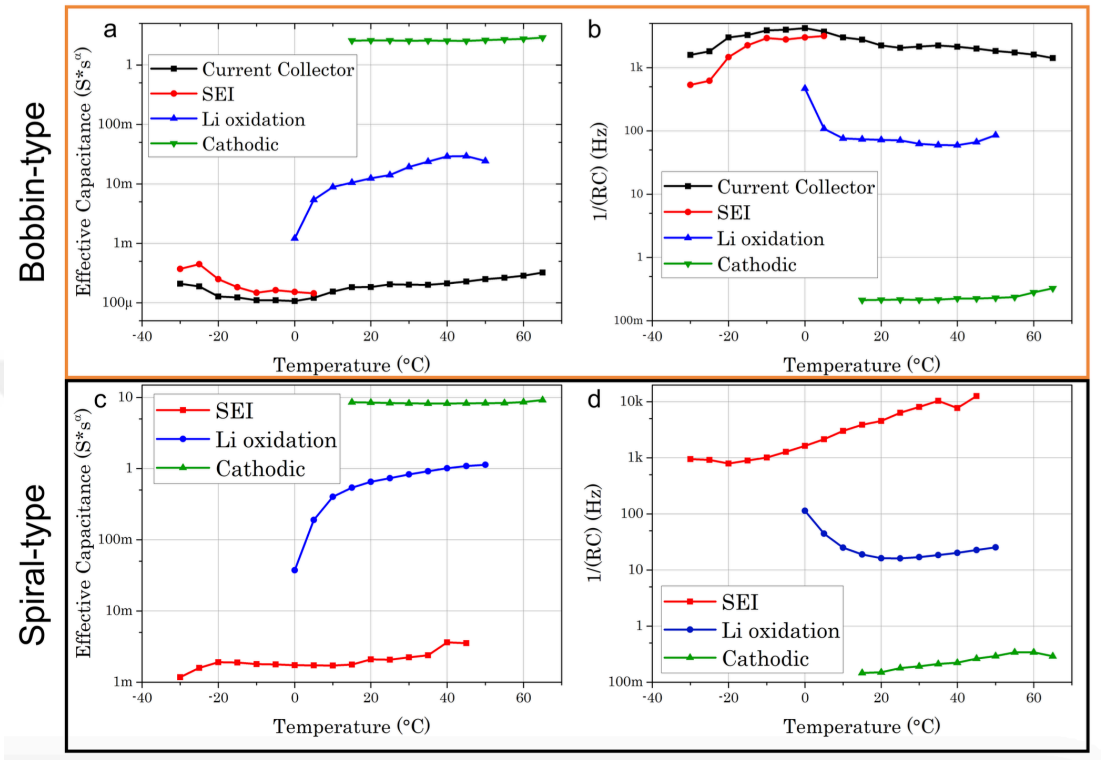

Figure 4.17: Effective capacitances of electrochemical processes in the bobbin (a) and spiral (c) type of Li/$SOCl_2$ batteries. Similarly, the 1/RC values of bobbin (b) and spiral (d) geometries are plotted.

as double-layer structures, effective surface areas, and surface impurities. As a result, the 1/RC and effective capacitance values can be seen in the Figure 4.17 below:

To begin with, a large difference in capacitance values can be seen between the spiral and bobbin types. This is due to the large surface area of the spiral geometry. Additionally, almost all processes have a slight increase as the temperature rises, resulting from the increased ion mobility and double-layer charge density. Similarly, the processes exhibit parallel behaviors as the temperature changes. The cathodic process remains constant because of the highly porous carbon structure. On the contrary, the Li oxidation and SEI processes yield a

slight temperature dependency in both architectures. These two processes will be investigated with Arrhenius relations, and their activation energies will be analyzed.

Moreover, the current collector and SEI processes converge after a certain temperature and become difficult to separate. This trend can be observed in both Nyquist/Bode plots and this figure. As a result, after the merge, these two processes are convoluted, and the current collector dominates the response. From the spiral type and other results, it is well-known that Li has an apparent temperature dependency. Therefore, the consistent and non-changing semi-circle belongs to the current collector.

Overall, the values (1/RC and capacitance) of electrochemical processes are in the same order of magnitude for both architectures. Therefore, the processes have similar kinetic properties. Since the chemistry and processes are identical, it is expected to have these results. Furthermore, a deeper look into the temperature-dependent processes will provide details about the kinetics.

As seen in Figure 4.18, electrochemical processes observed with EIS have different temperature-dependent behaviors. To begin with, SEI processes (charge transfer through the SEI) have a high-temperature dependency, whereas the cathıodic mass transport or LiCl adsorption has almost no dependency. Furthermore, the Li oxidation has a change with respect to temperature, which is observed with all metallic Li electrodes. Li oxidation has a stable activation energy, and it has been covered in our group's previous publication in detail[60]. The activation energy of Li oxidation is between 10 and 20 kJ/mol and does not change significantly as the SoC decreases. In addition, the bobbin-type SEI

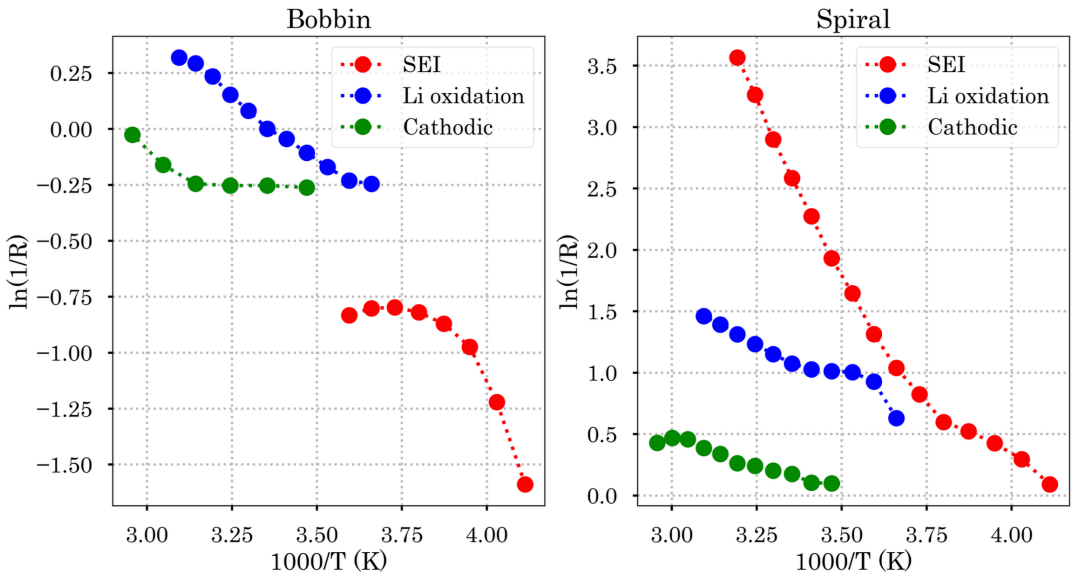

Figure 4.18: Arrhenius plots of different electrochemical processes observed in the EIs of the spiral (right) and bobbin(left) geometries, analyzed at 80% SoC.

processes do not have any data point after a certain temperature due to the merging with the current collector. Moreover, the spiral SEI layer has more than one linear segment, occurring at different temperature intervals. In literature, there are studies that show that the SEI layer is made of multiple structures and has a dynamic nature[92][93]. Therefore, multiple layers and different pore sizes can heavily affect the SEI properties at different temperatures and cause various activation energies.

Thereafter, the impedance response of the two architectures is investigated in terms of SoC variance. Since the batteries yield different EIS spectra, variation within SoC is expected eventually. The mechanism of consumption for $Li/SOCl_2$ batteries consists of Li^+ transfer from the metallic Li anode to the porous carbon cathode. Meanwhile, the Li^+ reacts with $SOCl_2$ along this movement and forms LiCl, which deposits on the cathode.

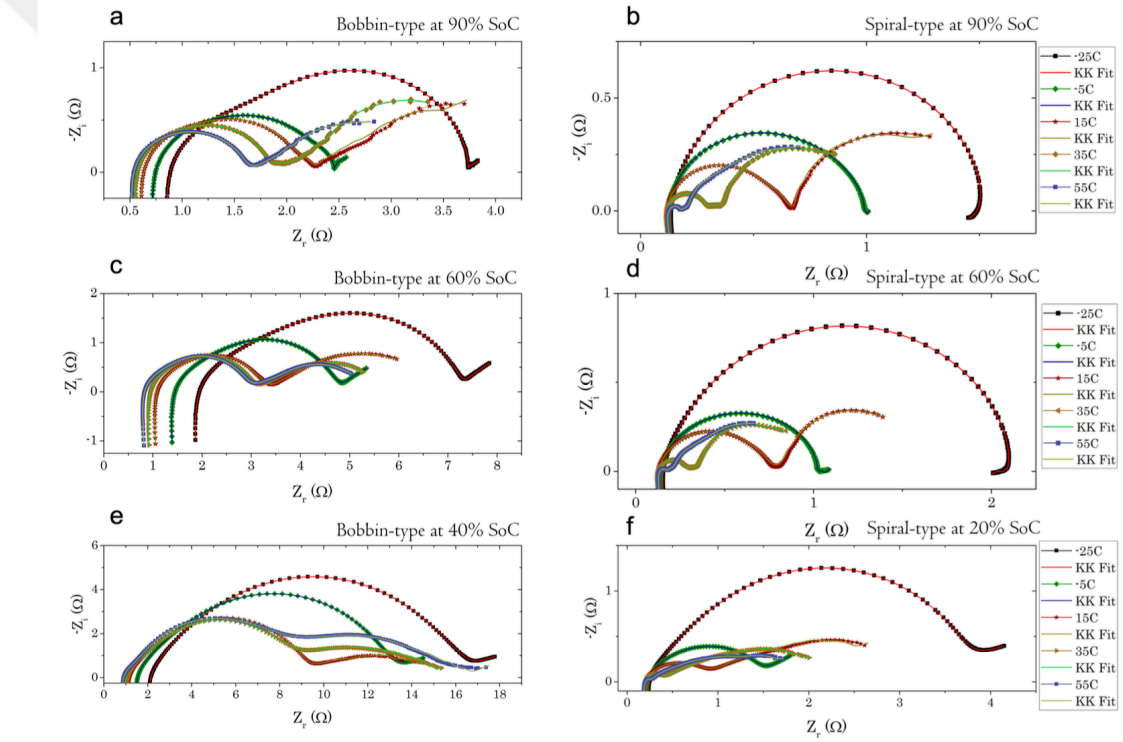

Figure 4.19: Bobbin-type temperature-dependent EIS responses at high (a), middle (c), and low (e) states of charge. Likewise, the spiral responses at high (b), middle (d), and low (f) SoCs are plotted.

In Figure 4.19, the impedance response of the two geometries is plotted. A notable feature in both types of batteries is the increasing overall impedance. As the batteries are discharged, the electrolyte (or the active material) amount decreases, and charge transfer resistances increase. Similar to the temperature-dependent case, the series or solution resistance also increases as the batteries are discharged. This is more prominently observed in the bobbin type, where the electrolyte amount is higher. In addition, the merging or converging of the current collector and SEI peak in the bobbin type is observed at all SoCs. As a result, this process is SoC-independent and occurs throughout the battery life span. For the Li oxidation process, the semi-circles do not show any significant change for both geometries. Li oxidation occurs in the bulk of the metallic Li anode and is not directly related to its surface properties. In a similar fashion, the cathodic processes or semi-circles exhibit a steady and robust structure in both types. Therefore it is only affected by the electrolyte or the active material amount, which has little to no effect on the impedance response. Lastly, the overall impedance increases greatly at the lowest SoC measurements due to the consumption of the active materials inside the cell. This is also confirmed by the Arrhenius plots in Fig. 4.20, where the lower SoCs have higher resistance values for the charge transfer process. The linear segments of the bobbin case are due to the convolution of the semi-circle with the current collector. As a result, the resistance value (used in this plot) does not change with respect to the temperature. The effect of the current collector can lead to misinterpretation of the results in the bobbin case, where the spiral case shows highly temperature-dependent metallic Li behavior, similar to the previous chapters. Therefore, comparative evaluation of the results with the literature and control experiments should be done to assign and process the results properly.

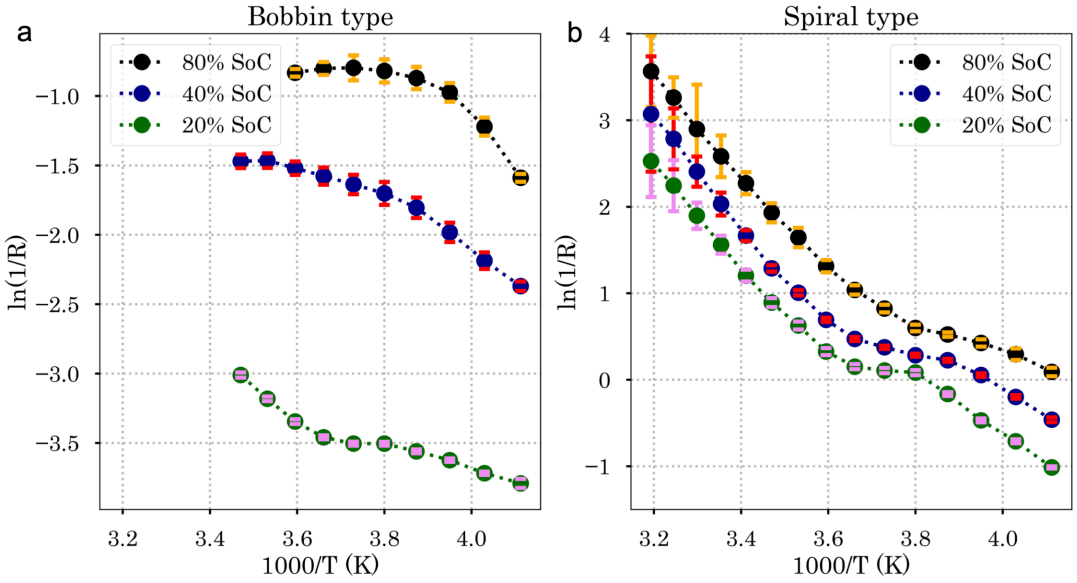

Figure 4.20: Arrhenius plots of charge transfer resistance across the SEI for spiral (right) and bobbin (left) geometries at different SoCs.

In these processes, the activation energy measured is the apparent activation energy, which contains not only the charge transfer process' activation energy but also the additional energy barriers of the experimental conditions and resistances[94]. Therefore, experimental parameters such as surface impurities or defects, transport limitations, multip-step charge transfer processes of the SEI layer, and temperature-dependent structure of the SEI layer can yield variations in the apparent activation energies. These complex processes produce the different slopes (or energies) on the Arrhenius plot. Since these two geometries of lithium thionyl chloride batteries have significant differences, differences in the Arrhenius plots or activation energies can be observed. As a result, complex electrochemical systems, or SEI layer in this case, can indicate the variations in the Arrhenius plots and various activation energies.

These results highlight a few critical points regarding the architectural effect

on the battery impedance response. First of all, the geometry plays a critical role in the impedance. Electrode surface areas, electrolyte amount, and current collector features determine the impedance response of these batteries. Secondly, the temperature-dependent EIS indicates that electrochemical processes inside the batteries can affect and dominate each other's impedance response at various temperature ranges. Therefore, the correct identification of these processes is critical during the evaluation of these results. Lastly, the activation energy calculation via the Arrhenius relations proves that these processes yield different profiles, meaning that the results should be well-separated and investigated, such as SEI and current collector semi-circle merging at elevated temperatures.

To sum up, temperature-dependent EIS is a valuable tool for the characterization of batteries with the proper planning and execution of the experiments. These factors include the KK-compatible measurement methods, correct diagnosis of the observed processes, and detailed evaluation of the results. Therefore, the methodology and processes explained in this chapter may shed light on the EIS-based characterization of various batteries.

4.3 Conclusions

In this chapter, temperature-dependent EIS is utilized for the investigation of electrochemical processes observed in the impedance spectra. The activation energies are calculated via the Arrhenius equation, which is related to the change in the resistance with respect to the temperature. Coin-size cells are assembled to isolate each electrode type with different electrolyte compositions to investigate the SEI properties, as well as the solution resistances. The results conclude that

the SEI structure is directly related to the electrolyte, and the SEI layer is made of the species inside the electrolyte. Therefore, the transfer processes through this SEI layer are dependent on the composition and show different activation energies. In addition, the symmetric cells are produced to isolate and understand the electrode processes individually. Thereafter, the complete cell spectra can be easily identified and evaluated. Similarly, the aging mechanisms of a battery-type cell are investigated, and results indicate that the aging is due to the anode and the cathode of the cell at different cycling counts. Thus, the limiting factors or compositions are evaluated via temperature-dependent EIS. Lastly, the spiral and bobbin geometries of lithium thionyl chloride batteries are investigated, and results conclude that both geometries have different impedance responses even though their chemistries are the same. Similarly, the activation energies of various processes inside these cells are compared, and similar energy values are found. Moreover, the geometries are compared, and the effect of the current collector on the bobbin-type cells is explained where it dominates the high-frequency region of the cell's impedance.

Chapter 5

EIS Measurements of Tekcell $SOCl_2$ and SO_2Cl_2 batteries

5.1 Introduction

This chapter is based on our collaboration with Korean battery manufacturer Vitzrocell/Tekcell, and we published our study in February 2024[95]. In this research collaboration, EIS of C and D-size bobbin type batteries with 100% $SOCl_2$, 85% $SOCl_2$ + 15% SO_2Cl_2 and 15% $SOCl_2$ + 85% SO_2Cl_2 ratios.

5.2 Experimental Section

Using the default EIS script, Galvanostatic Electrochemical Impedance Spectroscopy (EIS) was conducted on Tekcell batteries via Gamry Instruments Interface 1000E (potentiostat/galvanostat/ZRA). The batteries were placed inside a grounded Faraday Cage to avoid electromagnetic interference. The measured cells D-size (19 Ah, 3.6 V Open Circuit Potential (OCP), bobbin-type geometry) and C-size (8.5 Ah, 3.6 V OCP, bobbin-type) batteries, where the mixture cells' OCP is 3.9 V.

Before all measurements, $SOCl_2$ batteries require an initial current withdrawal from the battery. The purpose is to form cracks on the metallic Li (anode) surface, which is covered with a LiCl passivation layer (also known as solid electrolyte interface (SEI)). After forming cracks by current withdrawal, Li^+ can go through these cracks, and the battery functions normally. During the measurement, a current must be withdrawn at the same time as the alternating current (AC) to prevent the reformation of the passivation layer. Previously, we stated these currents ranged between 10 mA and 100 mA. In this report, the new method increases the magnitude of current withdrawal as the state of charge decreases.

This newly proposed approach uses Gamry's fast measurement mode rather than Gamry's low-noise measurement mode. Fast measurement mode is optimized for acquiring the data set by applying fewer sinusoidal signals. As a result, the measurement is quicker than normal measurement. On the other hand, low noise mode is engineered to apply longer excitation sinusoidal signals and acquire the data with less noise. The downside is a longer waiting period during the measurement. Our experience with the previous chemistries and measurements

showed that mixture cells require a faster measurement due to the SEI formation in these cells being quicker than the 100% $SOCl_2$ batteries. Furthermore, the lower frequency limit was set to 10 mHz, which was 1 mHz in previous measurements. The purpose of doing this is that the SEI layer between the anode and the electrolyte is so stable that it re-forms during longer measurements. As a result, we obtained the necessary parts to fit within a shorter time, with better KK compatibility. The following Nyquist plots in the results section were done using the new method called "variable DC offset." In this method, we started with smaller DC magnitudes and gradually increased the magnitude as the battery discharged. The optimization process took some time with experimenting with different experimental parameters where the AC and DC amplitudes have been investigated and tested with different scenarios. As a result, the following values are reached. The AC and DC magnitudes are given in the table below.

Battery	**Discharge (Ah)/DC Magnitude (mA)**								
C-100%$SOCl_2$	0Ah/80	0.82/80	1.64/80	2.46/80	3.28/80	4.10/80	4.92/80		
D-100%$SOCl_2$	0/100	1.85/100	3.30/100	4.95/100	6.60/100	8.25/100			
C-85%$SOCl_2$	0/80	0.9/150	1.8/150	2.7/150	3.6/150				
D-85%$SOCl_2$	0/50	1.8/150	3.6/200	5.4/250	7.2/300	9.0/300			
C-15%$SOCl_2$	0/50	0.9/150	1.8/150	2.7/200	3.6/250	4.5/300	5.4/300		
D-15%$SOCl_2$	0/40	1.8/200	3.6/250	5.4/250	7.2/250	9.0/300	10.8/300	12.6/300	14.4/300

Table 5.1: Discharge amounts and DC magnitudes for all batteries. AC magnitude was always 10 mA in all measurements. To save space, only $SOCl_2$ amounts were used to define the battery composition.

In Table 5.1, the discharge amounts and withdrawn current magnitudes during the measurements can be seen. Discharge amounts were calculated from the theoretical capacity on the battery datasheet. The batteries were assumed to be consumed after their voltage dropped below 2 V during measurements. As discussed in the earlier reports, current withdrawals that are higher than recommended result in a lower capacity. This is observed in Table 5.1, specifically in the C-size batteries.

5.3 Results

5.3.1 EIS Measurement Results

C-size new chemistries gave better KK-compatible Nyquist plots, which can be seen in Fig. 5.1.

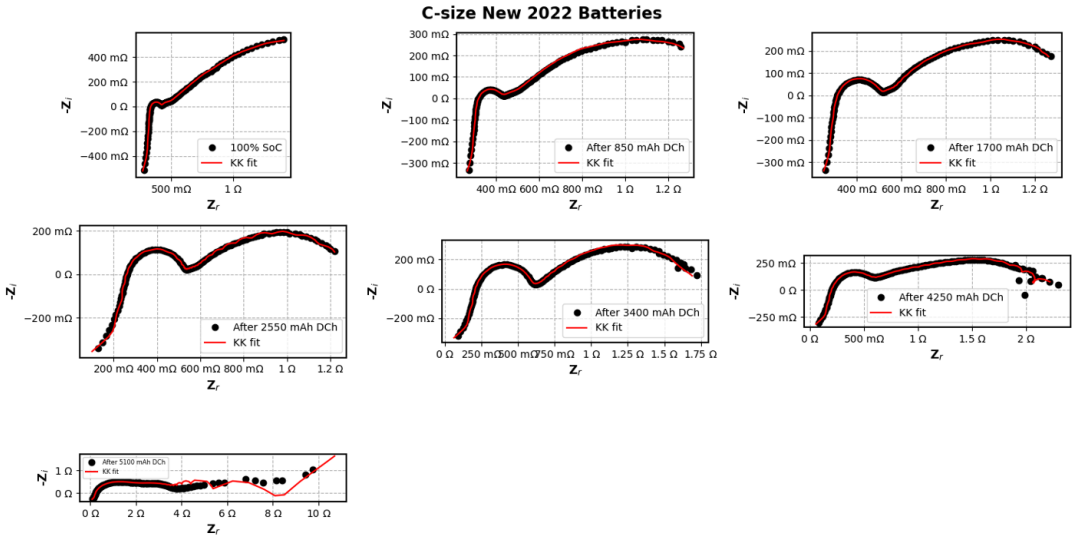

Figure 5.1: C-size new 2022 batteries at different states of charge.

The increase in the DC magnitude during the discharge is needed to keep the SEI layer formation out of the measurement. As seen in the table above, the magnitude increases and becomes significantly higher than the recommended discharge current, which is 80 mA for C-size and 100 mA for D-size batteries. However, a KK-compatible measurement is not possible with low DC currents. The main disadvantage is decreased capacity. Instead of 8.5 Ah capacity, we have observed 3.6 and 5.4 Ah capacities in C-size mixture chemistries, as well as 100% $SOCl_2$ sample. Furthermore, the overall impedance has become drastically larger at low states of charge. The semi-circles become more compressed and

broadened as the battery is consumed. This drastic increase of internal resistance is a common indicator that a battery's state of charge is low[96].

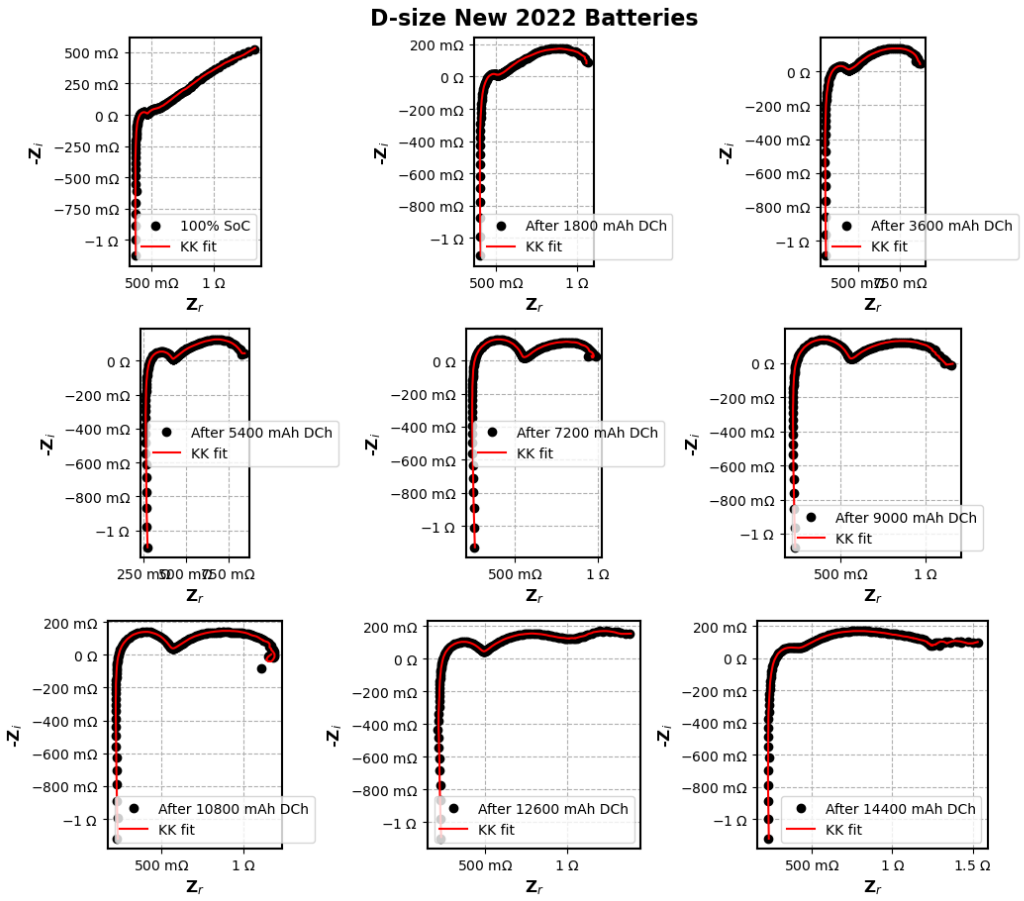

Figure 5.2: D-size new 2022 batteries at different states of charge. *This figure is reproduced with permission.*

D-size batteries gave similar results to the C-size, which can be seen in Figure 5.2. In both batteries, lower states of charges result in high-impedance spectra. As the battery ages, the resistance corresponding to the electrochemical processes in the battery increases. In addition, KK compatibility also deviates at lower states of charge, resulting in a noisy KK line.

5.3.2 Equivalent Circuit Fits

Equivalent circuit fits were done on all acquired spectra with the new variable DC method. C-size and D-size fit results can be seen in Figures 5.3 and 5.4, respectively. In addition, the complete fit results can be found in the appendix. In the plots, we can observe the change in solution (or series) resistance, which is denoted as R_S. The high-frequency semi-circle, which corresponds to the charge transfer through the SEI, gradually increases as the batteries age. However, the effective capacitance values of the high-frequency semi-circles did not show any trend. Moreover, middle-frequency semi-circles showed similar behavior during the course of battery discharge. Lastly, the low-frequency semi-circles, corresponding to the cathodic charge transfers, exhibited steady resistance values and slightly decreasing effective capacitances. On the contrary, the 85% $SOCl_2$ sample increased effective capacitances at a lower state of charge in both sizes. In every battery, we observed flatter and larger Nyquist plots as the battery consumed. As a result, the lower frequency semi-circle gets significantly larger.

We can draw the following conclusions from the results above:

- R_S values clearly show a difference as the batteries age. 100% $SOCl_2$ samples have increasing R_s values while the other chemistries remain the same.
- charge transfer resistance of 100% $SOCl_2$ battery is always slightly greater than the SO_2Cl_2 mixtures in all samples.
- Similarly, C_{dl} values for high-frequency semi-circle for 100% $SOCl_2$ are slightly greater than the others in both C and D sizes.
- Overall impedance of the batteries, regardless of their chemistries, increases

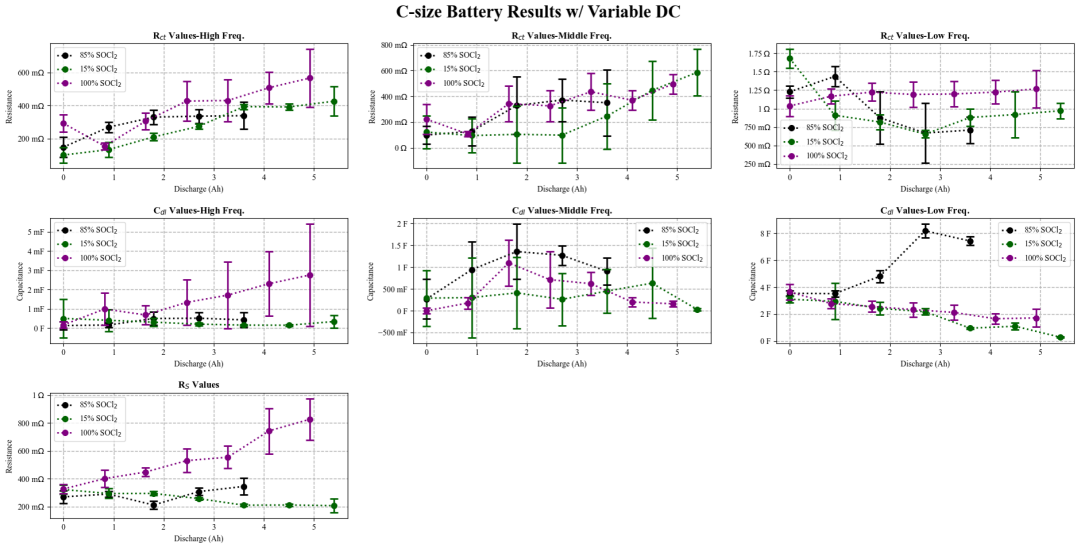

Figure 5.3: Equivalent circuit fits of C-size batteries, all chemistries included. *This figure is reproduced with permission.*

significantly at the lowest SoC measurements.

5.3.3 KK Compatibility, Residuals, and Non-linear Harmonic Analysis (NHA)

The second part of this study is related to the Kramers-Kronig relations and non-linear harmonic analysis (NHA). Our research group previously published on these topics individually[40][97]. In these studies, we have demonstrated the non-linearity effects on a simple Randles cell (made of resistors and a capacitor). The other study is also based on the NHA investigation of different battery systems. Briefly, NHA works according to the following procedure: the batteries were excited with a single sine current excitation, and the voltage response from the batteries was investigated. As expected, the voltage response is of a fundamental frequency and additional harmonics. These harmonics were detected by

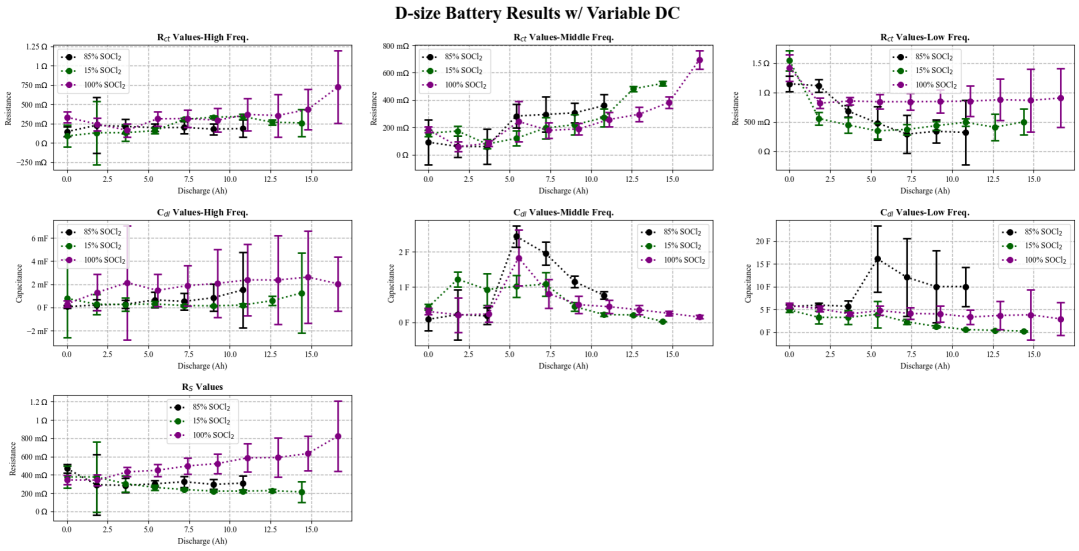

Figure 5.4: Equivalent circuit fits of C-size batteries, all chemistries included. *This figure is reproduced with permission.*

employing Fast Fourier Transformation (FFT). Observation of this fundamental voltage response and harmonics enables the detection of drift and non-linearity in the system[97].

One of the main findings in this section is the relationship between KK-compatibility and non-linear harmonic analysis (NHA). The linearity and causality of the acquired data are verified with KK tests, where good KK-compatible data (with around less than 1% residuals) yields an NHA with minimal non-linearity and drift. Additionally, the summation of the fundamental response and upper harmonics' amplitudes can be used to assess the data quality and provide information about the electrochemical processes resulting in the overall response[46]. A comparison between an equivalent circuit of a mixture battery, the actual battery with a KK-compatible fit, and a non-KK-compatible fit can be seen in Figure 5.5.

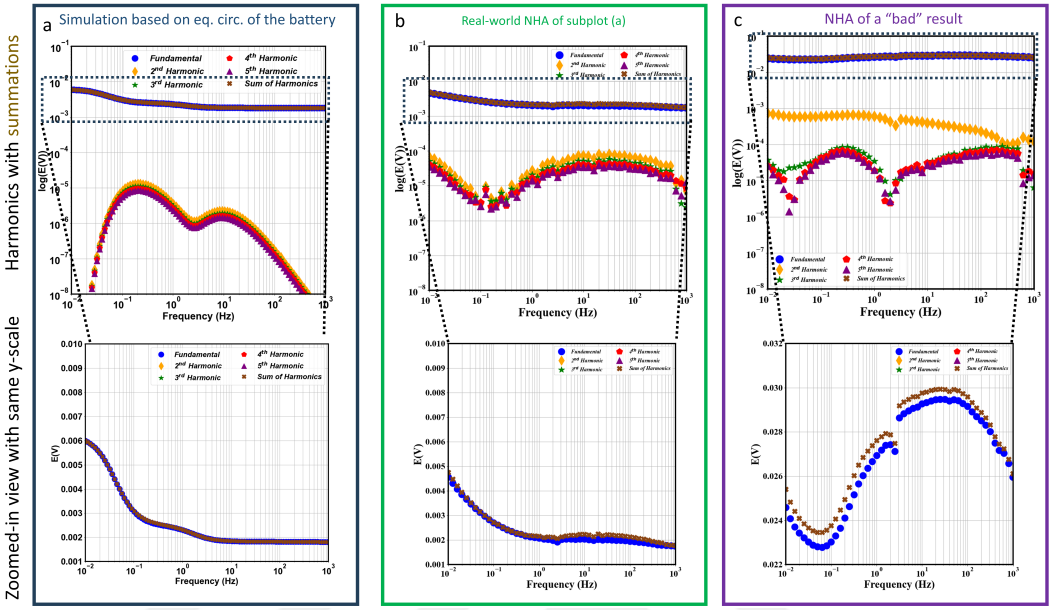

Figure 5.5: The equivalent circuit-based NHA of a battery (a), the real-world NHA of the battery with a good KK-fit(b), and a non-KK-compatible NHA result (c). The lower row is a scaled-up view of the fundamental response with a linear y-scale instead of logarithmic.

In non-KK-compatible results, the second harmonic arises from the rest of the harmonics and contributes to the system's non-linearity. In a study by Murbach and Schwartz, the second harmonic is related to the symmetry of the charge transfer processes on the electrodes[98]. It was observed that a second harmonic arises on the frequencies of kinetic processes. At high frequencies, the second harmonic and higher harmonics asymptote and only Ohmic resistances are significant. On the contrary, at low frequencies, only the diffusion impedance dominates the second harmonic. In the same study, it was also denoted that the third harmonic is sensitive to symmetry. However, the response is not as prominent as the second harmonic.

The presence of this significant non-linear harmonic indicates the response of the system is not purely linear. Comparison between the fundamental response

(the first harmonic) and the summation of the upper harmonics can be used to evaluate the overall quality of the EIS data, as seen in Fig. 5.5. A high-quality spectrum should have similar behavior to the equivalent circuit of the system (Fig. 5.5 (a)), where the fundamental response and higher harmonics' amplitudes are aligned with their expected values. Thus, the harmonics do not generate any significant increase when summed with the fundamental response, resulting in an overlapping harmonic sum. Moreover, the summation should provide a smooth and continuous distribution across the frequency range. Deviations from this theoretical summation, such as sharp changes in summation or significant differences between the model and real data, imply problems with the data quality. Real-world measurement data can present a slight increase in the harmonic sum at certain frequencies due to drift. In Fig. 5.5 (b), one may observe the drift and the fractional increase in the harmonic sum. Additionally, the harmonic response of equivalent circuit fit at high frequency is also observed in the real data plotted in (b). However, in non-KK-compatible data, as seen in Fig. 5.5 (c), The sum of harmonics exhibits a difference above the fundamental response, almost at all frequencies. As a result, the quality of the data can be evaluated by investigating the fundamental response and the total sum of the harmonics.

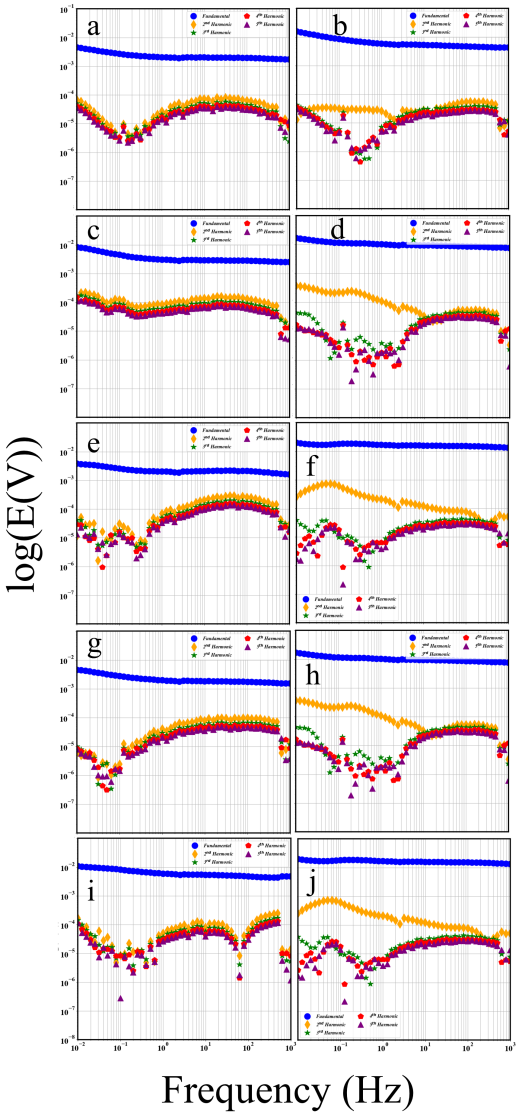

Figure 5.6: C-size 85% $SOCl_2$ battery with KK-compatible results at high (a), middle (c), and low (e) SoCs. In the right column, the same states of charges with non-KK-compatible results (b), (d), and (f). 15% $SOCl_2$ battery with KK-compatible results is plotted at high (g) and Low(i) SoCs, whereas (h) and (j) show non-KK-compatible results at the same SoCs. *This figure is reproduced with permission.*

Figure 5.6 shows the NHA results of C-size mixture batteries. In literature, some studies suggest that the even harmonics (the second and the fourth harmonics) are insignificant due to the symmetry of the electrochemical system[55]. In these cases, the response of the system also exhibits symmetry and suppresses the even harmonics. However, in EIS studies of the primary Lithium batteries, both even and odd harmonics can provide potentially valuable information about the system, and it is not always accurate to ignore the even harmonics[99]. In impedance measurements of simple RC circuits, the even harmonics are visible[40]. While the symmetry of the system can dictate the presence of even harmonics, other parameters can have an effect on the harmonics. The excitation signal and its amplitude can affect the amplitude of the harmonics. In Figure 5.7, we can observe increasing AC amplitude in the simulation. As the AC amplitude increases, the response voltage of both the fundamental and the harmonics show a direct proportion.

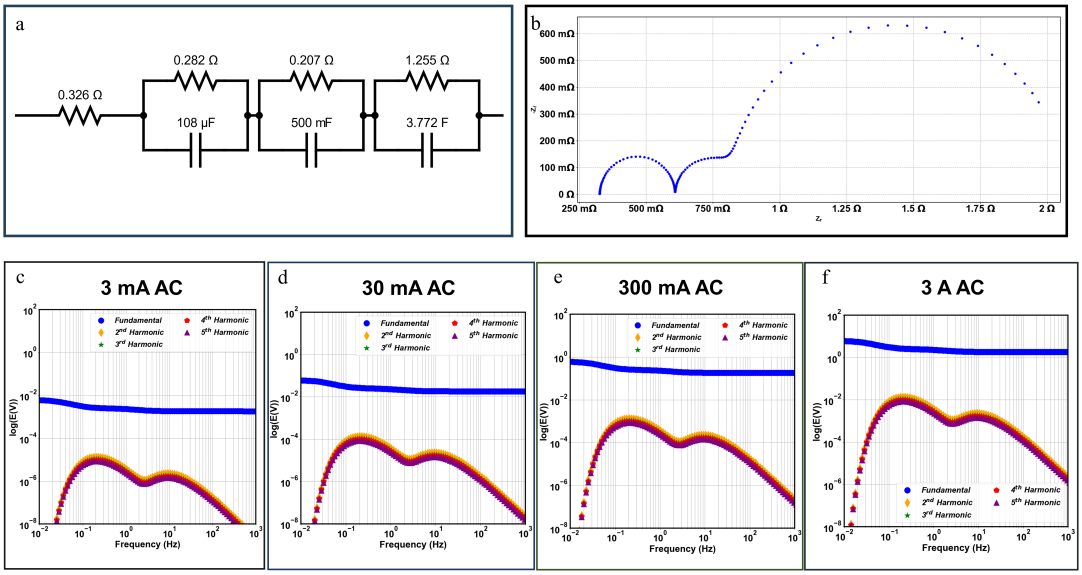

Figure 5.7: The equivalent circuit of a C-size mixture battery (a), simulated Nyquist plot of the same equivalent circuit (b), simulations of NHA with 3 mA (c), 30 mA (d), 300 mA(e), and 3 A (f) AC amplitudes. *This figure is reproduced with permission.*

Additionally, the phase of the excitation signal can have a slight effect on the harmonics. Starting from the maximum value of the excitation signal magnitude (cosine function instead of a sine) can change the amplitude of the harmonics. Simulation results of applying a cosine excitation signal instead of a sine can be seen in Figure 5.8. Regardless of the phase, the harmonics are always present in a similar shape in both scenarios. The peak frequencies exhibit initial transients where the phase of the excitation signal has a minor effect. At the peak frequencies, time-domain data shows drift in voltage response, of which we have studied and published previously[40]. Similarly, the exact position of the harmonics' peak frequency can shift slightly, depending on the signal phase. As demonstrated in

Fig. 5.8, applying a cosine signal shifted both of the peaks to the lower frequencies. Overall, our real-world data and simulated spectra may not overlap due to the excitation signal differences.

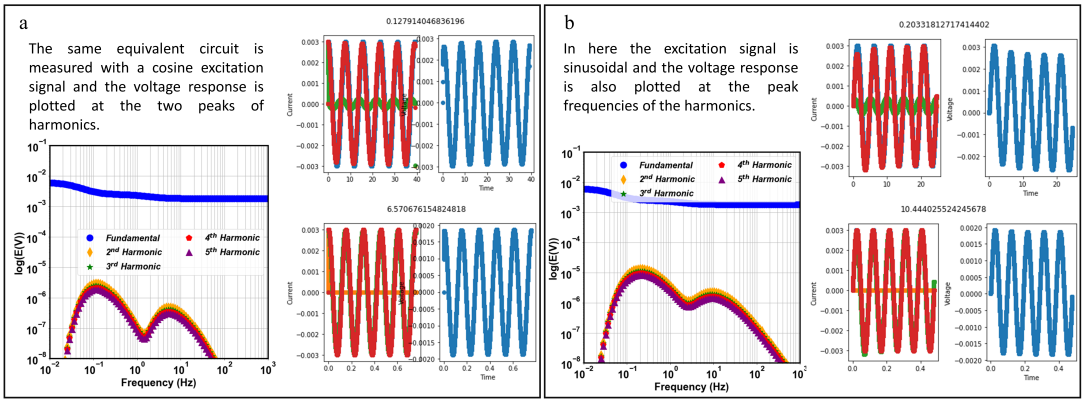

Figure 5.8: Simulation results of the equivalent circuit described in 5.7(a) with a cosine (a) and sine (b) signal. Time-domain data representing the excitation signal and voltage response at the peak frequencies of the harmonics are also plotted alongside the frequency-domain plots. *This figure is reproduced with permission.*

In real-world applications, the battery impedance responses can be complex, and even harmonics may arise from these complex electrochemical processes, interfaces, and interactions. As a result, even harmonics carry information about these secondary or more subtle processes. Additionally, higher-order nonlinearities such as relaxation processes, electrode heterogeneity, or interfacial interactions can be captured by the even harmonics. In EIS applications on batteries, it is a common practice to consider both the even and odd harmonics. However, in some cases with more simple electrochemical systems or weaker even harmonics, only the odd harmonics can be considered. The choice can be made by considering the structure of the electrochemical system and the aim of the investigation.

The KK-compatible results gave high-order harmonics with less than 1% amplitude of the fundamental response. Furthermore, the non-KK-compatible results showed non-linearity (where the order of the harmonics distorted, e.g., the third harmonic has a bigger amplitude than the second one). Similarly, the drift is explained by the significant change in the magnitude of the harmonics as the frequency changes. However, one must be careful with the exact diagnosis since the initial transients have a similar shape in frequent domain data[40].

The battery's state of charge has not directly affected the NHA results. KK-compatible results provided an equal distribution of voltage responses across the frequency range, whereas non-KK-compatible results yielded a larger drift at lower states of charges. However, the higher SoCs yielded a more clearer NHA results. Some step-like shapes can be observed at certain frequencies due to the instrumentation filters and hardware components.

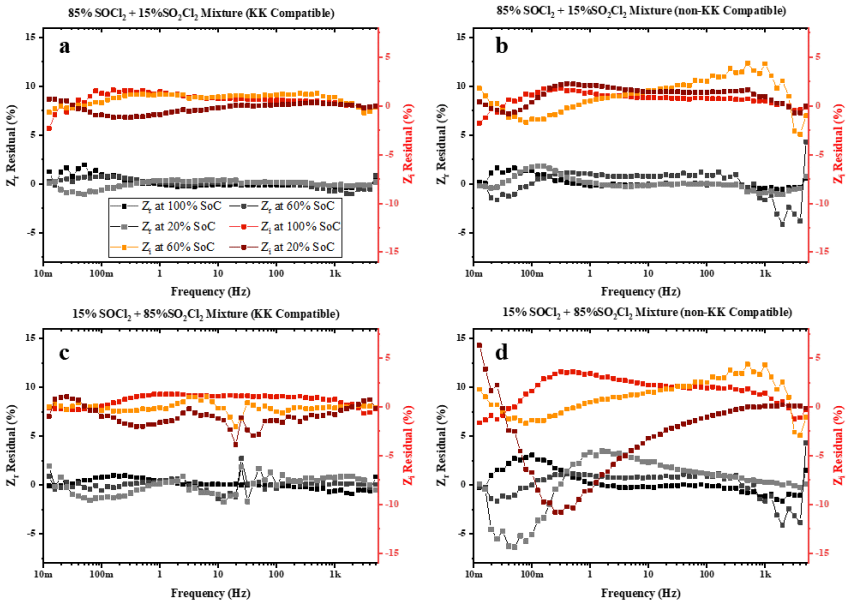

Figure 5.9: Kramers Kronig residuals of batteries with compatible and non-compatible KK fits. *This figure is reproduced with permission.*

In Figure 5.9, we can observe the real and imaginary residuals of the mixture batteries for both KK-compatible and non-compatible measurements. The figure shows that results with less than 1% residual amplitudes are identified as KK-compatible, and 5-10% deviations lead to non-KK-compatible results. These results were obtained with the standard KK fit function (in default/auto mode) of Gamry Echem Analyst software. In Gamry software and many other KK fitting software, the number of Voigt elements (which have their own time constants due to RC structure) is selected using an automated algorithm. The autofit function of the Gamry software finds a balance point in terms of Voigt elements to provide the best fit without overcomplicating the data[32]. Selecting the appropriate Voigt element number is critical for the accurate representation of the system's

behavior. Too few time constants result in higher residuals and reduced accuracy because of not being able to capture the system's complexity. Oversimplified fit can also generate higher residuals near the frequency boundaries where additional elements are necessary to fit. On the other hand, too many time constants yield an overfit of the spectrum and introduce extra complexity into the fit. As a result, unnecessary fitting of noise or introducing artifacts to the fit data leads to unstable and unreliable results. A comparison between the fewer Voigt elements and more Voigt elements than the optimum value is plotted in Figure 5.10. As seen in the figure, fewer elements resulted in residual growth at frequency boundaries. On the contrary, more time constants led to an increase in residuals below a certain frequency. Both of these fits produce unreliable KK results, where the optimum parameters of Voigt elements depend on the specific electrochemical system, the quality of the acquired spectrum, and the frequency range of interest.

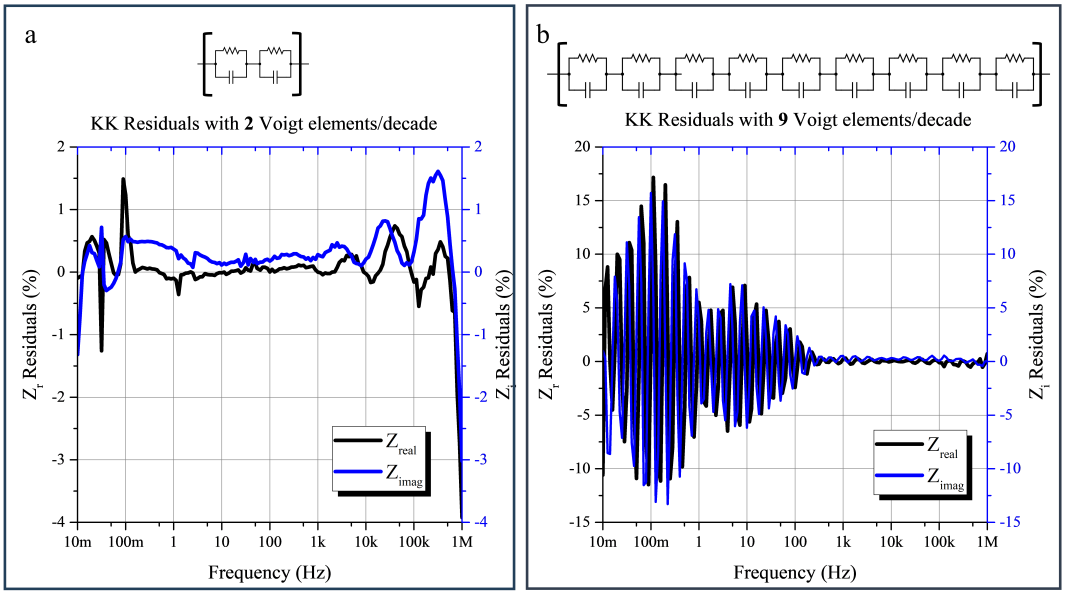

Figure 5.10: Kramers-Kronig residuals with 2 Voigt elements per decade (a) and 9 elements per decade of frequency (b). *This figure is reproduced with permission.*

5.4 Conclusions

In this chapter, the C and D-size bobbin-type batteries are investigated with different ratios of $SOCl_2$ and SO_2Cl_2. First, an experimental method of KK-compatible EIS measurement is proposed, which requires an increase in the DC offset as the battery SoC decreases. The equivalent circuit fit results are presented in the appendix of this thesis. Thereafter, a relationship between the KK and non-linear harmonic analysis is investigated based on this battery composition. The results show that the two methods exhibit parallel behaviors, where a non-KK-compatible EIS spectrum also yields pronounced harmonics or overtones. On the

other hand, a KK-compatible spectrum has no significant harmonic deviations. Thus, these two methods can be used to evaluate the impedance of a complex electrochemical system such as $SOCl_2$ and SO_2Cl_2 chemistries.

Chapter 6

Conclusions

The purpose of this thesis is the utilization of electrochemical impedance spectroscopy (EIS) in battery measurement and modeling. By using the EIS, different electrochemical processes inside various battery systems are investigated via complementary methods such as temperature-dependent EIS and non-linear harmonic analysis (NHA). To understand these methods, detailed derivations and analysis techniques are introduced.

Temperature-dependent EIS has shown that many processes occur inside the batteries, but they are not always detectable at all temperatures. Some processes dominate the overall impedance response, or they can disappear at certain temperatures, and this situation must be studied carefully. To study the processes, different cell architectures with symmetric configurations have been employed. By doing so, the electrode processes are isolated and can be evaluated individually. Thus, the diagnosis of a complete cell or a battery can be performed correctly. For instance, the comparison of spiral and bobbin geometries has shown that these

two cannot be measured and modeled in the same way since the cell construction can affect the impedance response. The experiments and measurements are evaluated using different cell configurations. Thereafter, Arrhenius plots provide the activation energy of each designated process and can determine whether these processes change when temperature changes. These activation energies are investigated with respect to the SoC and cycling counts. The results show that the activation energies are dependent on the electrolyte composition and vary within the cell architecture. Moreover, the symmetric cell configurations are employed to isolate the electrode types and extract the processes individually. Thus, the processes are assigned to the electrochemical processes with respect to their characteristic frequencies and investigated accordingly. Overall, the electrodes affect each other when combined, as the battery configuration and data analysis require the separation of these processes.

Similarly, NHA has been utilized to investigate the non-linear response of an electrochemical system. NHA shows that a system can exhibit non-linear behavior with amplified harmonics at certain frequency ranges. The investigation of these harmonics and their order (*the second, the third* harmonic) can provide further information about the symmetry and the structure of the electrochemical cell. However, NHA investigations have their own complications, such as initial transients. The initial transient can be present with dummy cells made with simple circuit elements as well as a pure simulation based on the dummy cell experiments. Furthermore, different experimental variations are presented, and results conclude that the initial transients are present in every scenario. Similarly, the NHA correlates with the linearity, causality, and stability of the system, which is usually checked with Kramers-Kronig (KK) relations. These two methods are

in good agreement to determine the validity of the acquired spectra. The investigation indicates that a KK-compatible spectrum is also clean in terms of NHA without any amplified harmonics. Similarly, a non-KK-compatible spectrum can yield deviations in the NHA analysis.

6.1 Future Recommendations

In light of the information given above, the experiments and the investigations can further go on with different cell chemistries and geometries in terms of temperature-dependent EIS and NHA analysis. Therefore, the studies of SoC and aging estimations can be performed with different electrolytes and provide information about the electrode kinetics of these processes. Similarly, the effect of architecture can be further expanded with different cell types/chemistries and their EIS measurements. Additionally, the simulations of EIS measurement can be performed to model the electrochemical processes occurring inside the batteries by using the information provided in this thesis.

Appendix

EIS and NHA of Electric Guitar Pickups

Electric guitars rely on their pickups to produce signals[100]. The pickups are the essential components of the guitars and are selected according to the desired tone. Since the emergence of mass-produced electric guitars, two types of magnetic guitar pickups have been used extensively. Historically, single coil pickups were invented first and used in a very popular guitar model called Fender Telecaster[101][102]. After being used excessively, guitar players complained about the humming noise when the strings were not vibrating. Soon after, the solution came from Gibson with reversely wounded, oppositely polarized double coil (humbucker) pickups[100]. Since then, these two types of pickups have become the most popular pickup architectures in the electric guitar industry[103].

In the literature, the study of guitar pickups can be found as the investigation of pickup positions on the instrument[104]. Further investigations regarding the modeling of the magnetic pickups were also reported in another publication[105]. Additionally, guitar pickup behavior was also investigated[106]. Numerical modeling and analysis were done by Lemarquand et al., and Horton et al.[107][108].

Another discussion related to this research is non-linear analysis. The electric guitar pickups were investigated with a physical oscillating string setup in numerous publications[109][110][111].

This chapter uses EIS to measure how single coil and humbucker electric guitar pickups exhibit different impedances at different signal frequencies. The scope is limited to the measurement of the pickup only, where all other external circuit elements found in a real electric guitar are assumed to be frequency agnostic. Additional circuit elements such as potentiometers, capacitors, and resistances have a drastic effect on the output signal of an electric guitar.

Methodology

6.1.1 Measurement Parameters

The EIS measurements were done with Gamry Instruments' Potentiostat/Galvanostat/ZRA Reference 3000. Acquired spectra were then fitted with Gamry Echem Analyst Software(v7.10.0). Additionally, Kramer-Kronig results were calculated using the built-in function of Echem Analyst. The measurements were performed with 500 μV AC and 0 V DC. The measurement mode was adjusted to low noise to get a higher resolution. The frequency range was from 100 kHz to 1 Hz, with 20 points per decade. The duration of the measurement is about 10 minutes, depending on the points per decade and measurement mode settings. As for NHA measurements, the AC amplitude was 10 μA, and the frequency

range was from 1 kHz to 10 mHz. The pickup is placed inside a grounded Faraday Cage to avoid any outside electromagnetic interference. An illustration of the experimental setup can be seen in Figure 6.1. Since a pickup has two cables (ground and signal), the ground cable is connected to the counter and reference connections, while the signal cable is connected to the working and working sense ports of the potentiostat.

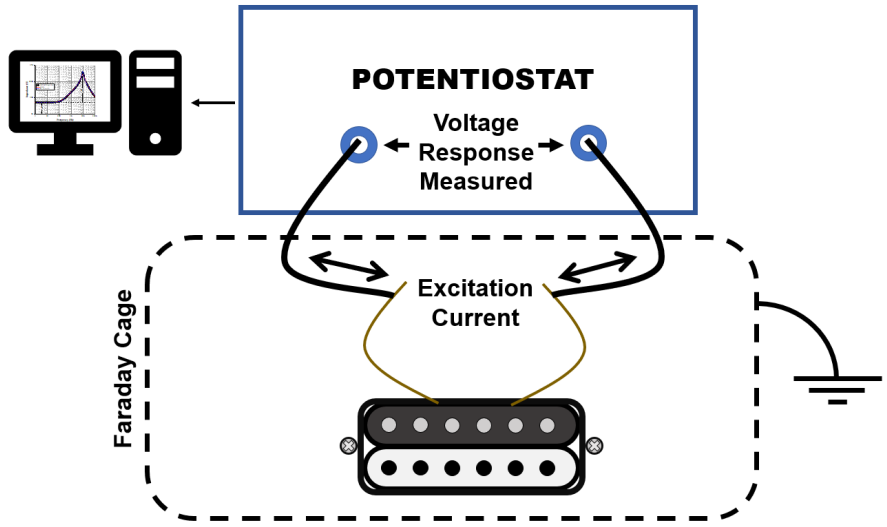

Figure 6.1: The experimental components of this research consist of the pickup, a grounded Faraday Cage, a Potentiostat, and a computer.

Pickup Specifications

The measured pickups have AlNiCo5 magnets and are designed to be used in the neck pickup position. The purpose of this selection was to compare moderate output, the same magnet type including pickups. Magnet material/type determines the characteristics of the pickup and is selected for the musical genre accordingly. AlNiCo5 is one of the most abundant magnet types on the current

market[112][113].

Equivalent Circuit Fits

The acquired spectra were fitted with the following equivalent circuit in Fig. 6.2. R_S corresponds to the series resistance, which is equal to the DC resistance when the pickup is measured with a multimeter. R_{PX} corresponds to the parallel resistance of the related RLC structure. L_X and C_X are inductances and capacitances, respectively. The X corresponds to the index of the respective time constant. The resonance frequencies of these RLC circuit elements can be calculated with Eq. 6.1. This equivalent circuit can be used to fit both of the pickups since both spectra acquired have one large peak and two shoulders at higher and lower frequencies. Those peaks are assigned to the three RLC structures in the equivalent circuit model and overlap the acquired data set. The fit results and their errors are given in the table in the appendix.

$$f_X = \frac{1}{2\pi\sqrt{L_{PX}C_{PX}}} \tag{6.1}$$

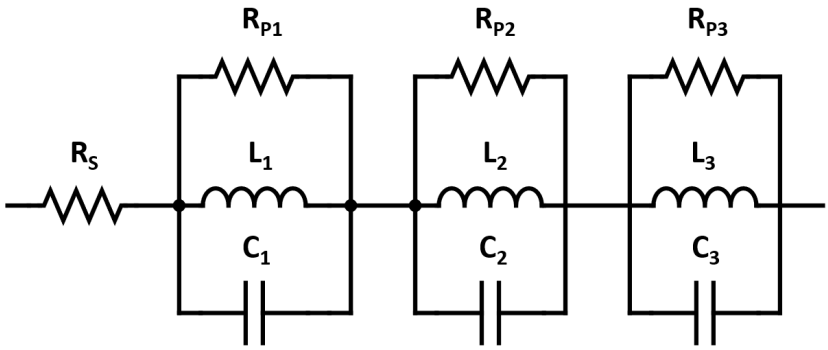

Figure 6.2: Equivalent circuit fit for the single coil and humbucker pickups.

6.2 Results and Discussion

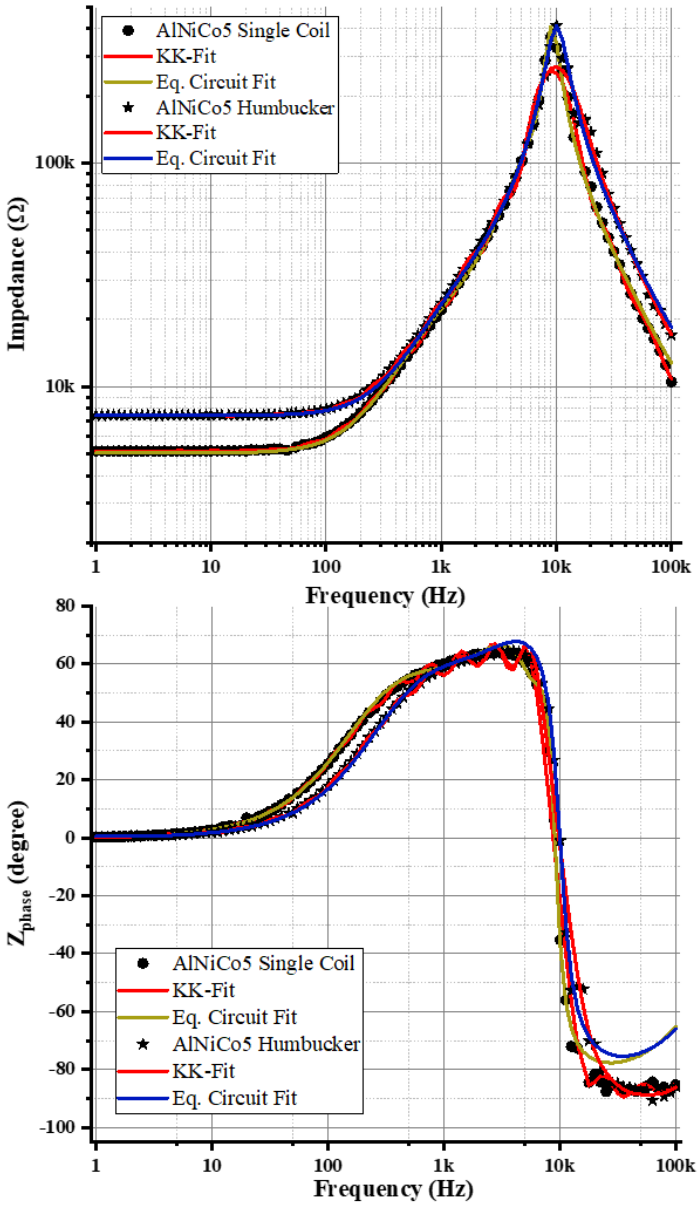

Figure 6.3: Impedance (upper) and phase angle (lower) spectra of single coil and humbucker pickups from 100 kHz to 1Hz.

In Figure 6.3, the impedance responses of the two pickups can be seen. The y-axis (impedance) is calculated from the division of input voltage to current response at the given frequency. In the impedance response, the impedance approaches a certain value at a low frequency. However, after a certain frequency, it shows a steady increase and reaches the apparent resonance frequency. This resonance frequency corresponds to the time constant of the RLC circuit it was designated to, and the y-axis magnitude is equal to the R_P value of the RLC section. The phase angle is the trigonometric degree difference (or the shift in phase) between the applied sinusoidal current signal measured voltage response. At ultrasonic frequencies, the phase angle is close to -90°, which indicates a capacitor-like behavior[114]. Furthermore, the phase angle quickly changes its phase at the resonance frequency, following an in-phase trend at lower frequencies. Overall, the phase angle plot explains the behavioral analysis of the pickups at different frequency regions. Both pickups showed similar phase plots with a slight offset between the 100-300 Hz range. The difference in this region is related to the series resistances (R_S) of the pickups.

The frequency range of electric guitar in music production is between 80 Hz to 15 kHz[115][116]. Of course, depending on the number of strings on the guitar and the tuning of the guitar, this range can have a lower end below 80 Hz. Additionally, depending on the genre of the music being produced, the upper end can also be shifted to lower frequencies. The difference between single coil and humbucker type at lower frequencies (bass) is prominent. The humbucker type has a higher series resistance (R_S) than a single coil. Furthermore, above 80 Hz, the impedance (corresponds to output) of the humbucker is higher than the single coil. Single coil pickups generally produce a bright and snappy sound,

whereas humbucker pickups usually have a warmer and darker sound[117][118]. The difference in the bass region has a direct effect on the sound characteristics of the pickups. Humbucker pickups are frequently used in music genres with distorted or overdriven guitars.

In many pickup catalogs, DC resistance (or R_S) is denoted alongside the magnet type. DC resistance gives an idea about the number of turns on the coil and the general output level of the pickup. The sound characteristics of the pickup can be determined with frequency-based response analysis or EIS in this case. As can be seen in Figure 6.3, the impedance changes drastically in the frequency range of a guitar.

The equivalent circuit fit elements are resistance (R), inductance (L), and capacitance (C). The resistance comes from the length and the diameter of the coil wrapped around the magnets, and the inductance results from the conductor wrapped in the coil. The capacitance results from the conducting wire (usually made of copper) being coated with an insulator to prevent short-circuiting. When two charged parts come across with an insulator between them, a capacitor is formed.

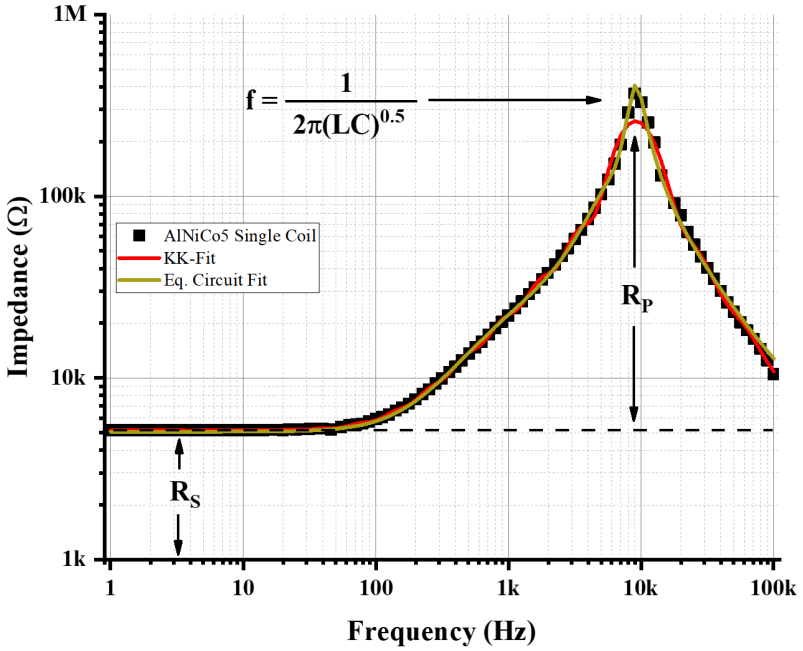

Figure 6.4: The components of the equivalent circuit elements on the impedance response of the most prominent (middle) peak.

The equivalent circuit fit and its corresponding elements can be seen in Figure 6.4. R_S value is equal to the DC resistance value of the pickup. The largest peak around 10 kHz is the resonance frequency. The fact that the equivalent circuit has three RLC sections instead of one is due to the shoulders around 2 kHz and 40 kHz. These shoulders are hard to see at first glance; however, with the equivalent circuit fit values, they can be identified. In a similar fashion, these shoulder peaks have their y-axis magnitude (impedance) by the R_P and frequency by the L and C components of the RLC circuits. To avoid any confusion, only the most apparent peak is implied in Fig. 6.4.

Table 6.1: Equivalent circuit elements used in the model and their values and errors. Abbreviations used in this table are: E.C.E. is Equivalent Circuit Element and its unit.

E.C.E.	Single-Coil	Error	Humbucker	Error
$R_S(\Omega)$	5.01 x 10^3	1.25 x 10^2	7.24 x 10^3	4.25 x 10^2
$R_{P1}(\Omega)$	2.51 x 10^4	1.20 x 10^3	2.51 x 10^4	1.76 x 10^3
$R_{P2}(\Omega)$	3.61 x 10^5	3.50 x 10^4	3.62 x 10^5	2.65 x 10^4
$R_{P3}(\Omega)$	2.20 x 10^4	4.66 x 10^1	3.16 x 10^4	4.51 x 10^3
L_1(H)	1.65	2.34 x 10^{-1}	1.43	5.10 x 10^{-2}
L_2(H)	2.11	4.75 x 10^{-2}	2.14	3.27 x 10^{-2}
L_3(H)	8.32	4.29	1.80	1.60 x 10^5
C_1(F)	5.51 x 10^{-9}	3.17 x 10^{-10}	6.05 x 10^{-9}	7.48 x 10^{-11}
C_2(F)	1.49 x 10^{-10}	3.24 x 10^{-12}	1.15 x 10^{-10}	1.99 x 10^{-12}
C_3(F)	2.53 x 10^{-12}	5.58 x 10^{-6}	6.58 x 10^{-12}	8.11 x 10^2

The equivalent circuit fits were performed on Gamry Echem Analyst Software. The number of components and, therefore, the free parameters is relatively large for a fit. To simplify the fitting process, resistance values of R_S and R_{PX} were kept constant and equal to the values obtained by observation of the data. Fitted values for both humbucker and single coil pickups can be found in Table 6.1 in the appendix section. There are a few parameters that showed a significant error in the table. These are due to the smaller values of capacitance, where accurately measuring can be challenging. However, the model fits the acquired spectra with a low error percentage overall. The number of time constants remains to be three for both pickups, regardless of their architecture.

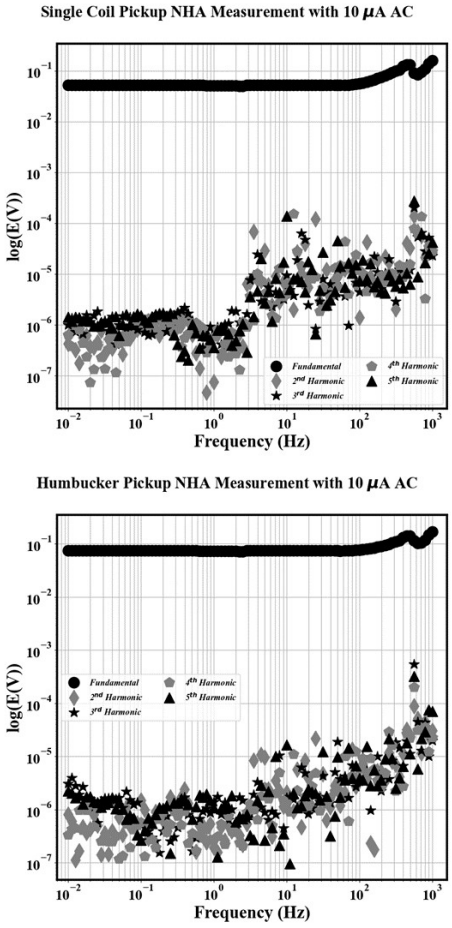

Figure 6.5: Non-linear harmonic analysis of (upper) single coil and (lower) humbucker pickups.

In Figure 6.5, the NHA of two pickups can be seen. The frequency range is lower than the EIS measurements in previous Fig. 6.3, due to the technical instrumentation issues. This figure concludes that guitar pickups only respond to a pure sine wave with a single frequency. The measurements were done in Galvanostatic EIS, where the input current is static (constant) at 10 μA. The voltage during these measurements (fundamental signal in Fig. 6.5) is in mV level. A typical guitar pickup generates similar amplitudes in terms of voltage[119]. The

response voltage is plotted with respect to frequency. The steps on the plots are due to the filters in the device; they are not pickup-related. The harmonics other than the fundamental voltage response are pure noise, implying that the harmonics (overtones) cannot be detected with EIS. Furthermore, the levels of these noises are significantly lower than the fundamental voltage response. On the contrary, the harmonics can be generated with the help of physically oscillating guitar strings. In literature, harmonic generation was done with an oscillating string, and harmonics were measured from the output signal[111][109].

Conclusion

In this study, electrochemical impedance spectroscopy of a single coil and a humbucker pickup (both are neck pickups) has been investigated. Acquired spectra are then fitted with an equivalent circuit model. The impedance response showed similar behaviors; however, the audible difference at lower frequencies is prominent. The offset at bass frequencies contributes to the sound characteristics of these pickups. The non-linear harmonic analysis of the pickups was also done, resulting in only the fundamental response signal (voltage) being observed while the harmonics are observed as noise floors. As a result, EIS cannot detect the harmonics generated by a single excitation signal on a guitar pickup only. An additional guitar-like setup with a physically oscillating string is needed to observe the harmonics. Since measuring the pickups with EIS takes a relatively short time, this method can provide the detailed behavior of the pickups at different frequencies. Therefore, it can be used as a supplementary figure in a guitar pickup datasheet.

Measurement Devices and Protocols

EIS measurements in this thesis were performed with either Gamry Instruments Reference 3000 or Interface 5000E. The software side is Gamry's bundle software v.7.10. Temperature-dependent EIS was performed in a homemade polystyrene chamber controlled with a Peltier cooling system. Furthermore, the spiral and bobbin types of batteries were measured using the Neware Climate Control Chamber.

Potentistat notes/tips: We always use Gamry potentiostats for measuring various electrochemical tests and scripts. We should ground ourselves with the blue grounding bracelets all the time. Especially during the dry winter months and wooly clothes, we are the sources of static electricity, and we can easily damage the cells by touching them without grounding. As a result, we should always ground ourselves with grounded mats and bracelets. First of all, the cells should be placed in a grounded Faraday cage to avoid external electromagnetic interference. It should be either Gamry's case or our temperature control chamber. After that, the cells should be connected with a four-electrode setup to the potentiostats. Initially, we should connect the positive terminal of the battery with thicker current cables inside and voltage measurement cables outside. Then, the negative terminal should be connected with the working and reference sides. When working with small-sized cells, these cables can come too close in contact with the metal sides and cause faulty measurements. Therefore, we must be sure of the connections before each and every measurement.

We have also installed uninterrupted power sources (UPS) for every potentiostat, cycler, and computer in our lab. Unfortunately, we have had some power

cuts from time to time, and we have malfunctioned and interrupted experiments and decided to get the UPS devices. After each power cut, we must check the status and the charge of the UPS devices in our lab to make sure that they are ready for the next power cut.

Spot welder notes/tips: For proper contact with commercial cells, a spot welding device is being used in our labs. Cell holders with springs and additional parts cause problems with the impedance measurements, and the impedance response is highly dependent on the contact impedance of the spring. Therefore, a solid, non-moving connection must be present for the connection to the potentiostats.

In order to perform clean and effective spot welding, we must sand down the oxidized part at the end of the tips with fine-gritted sandpaper. By doing so, we will not have sparks, and the current will pass through the electrodes, nickel tape, and the metal battery container. The oxidized section has a very high resistance compared to the bulk copper and generates sparks during operation. Therefore, before each spot is welded, we must sand down the tips, wipe them with a clean piece of paper, and select the appropriate current and impulse times. For instance, for coin-size cells with a thinner nickel strip, the knobs should be at 50 A welding current and 30 ms pulse time. For larger thionyl chloride batteries with a larger nickel strip, the knobs should show 65 A welding current and 45 ms pulse duration.

Temperature Chamber Notes/Tips: We bought the temperature chamber from Neware in 2023 and have been using it since. The temperature values for the experiments can be found in the old data files. Generally, this device does not require any specific calibration or maintenance since it is a closed system with

many refrigerators. However, due to the fact that it works like an air conditioner, it generates water from the air when it cools down the chamber. This evolved water is gathered in the bottom of the trey and should be cleaned with a clean microfiber cloth after every measurement. The exhaust of this water discharge is at the back, and we have already placed a bucket there to collect the water. Similarly, from time to time, we must discard this water into the sink. Additionally, after each power cut, the device stops working, and the experiments should be started in terms of temperature control. We should enter the fixed operation menu and adjust the temperature as usual. Moreover, we have placed a few silica-filled evaporating plates inside the chamber to avoid precipitation on the batteries, electrodes, etc.

Battery Cycler Notes/Tips: As of 2024, we have a few Neware branded battery cyclers for high and low currents. In all cases, the cycles work the same, and the points written here can be applied to all of them. First of all, we should install the latest compatible software on our PCs, which will be connected to an ethernet cable (RJ45). This software installation may be tedious and should be performed with care due to the installation of some drivers and packages. We should also be aware that this device works 24/7, and the program sometimes freezes and stops working. This usually occurs on older PCs with lower RAMs; however, we should be careful about this situation. In this case, we should restart the PC, open the program, and log in as admin to operate our experiments. Lastly, we have placed grounded mats under each cycler. Before touching the electrodes or the battery, we should place our hands on the mat and ground ourselves. A little shock can be experienced quite often, especially in winter months, but it is perfectly normal. Lastly, we should assign and set each channel to a specific

cycling/process in order to avoid any abnormalities and experimental differences.

The equivalent circuit fit results of $Li/SOCl_2$ batteries

The equivalent circuit fit results of the Tekcell primary $Li/SOCl_2/SO_2Cl_2$ batteries are presented in the following tables. The results are plotted in Chapter 5.

C-size 100% $SOCl_2$ Batteries Fits				
100 SoC	**High Freq.**	**Middle freq.**	**Low Freq.**	
L1	4.294×10^{-8}	1.037×10^{-5}	2.275×10^{-8}	H
R1	2.916×10^{-1}	6.633×10^{-1}	1.035	ohm
Yo1	1.630×10^{-4}	5.701×10^{-4}	3.640	S*s^a
a1	8.294×10^{-1}	7.010×10^{-1}	7.000×10^{-1}	
Ru	3.267×10^{-1}	2.863×10^{-6}	7.446×10^{-1}	ohm
After 850 mAh DCh				
L1	2.021×10^{-14}	1.155×10^{-12}	2.829×10^{-9}	H
R1	1.538×10^{-1}	1.069×10^{-1}	1.166	ohm
Yo1	9.864×10^{-4}	1.763×10^{-1}	2.783	S*s^a
a1	8.323×10^{-1}	7.010×10^{-1}	7.007×10^{-1}	
Ru	3.970×10^{-1}	5.300×10^{-1}	6.581×10^{-1}	ohm
After 1700 mAh DCh				
L1	4.411×10^{-14}	3.141×10^{-12}	3.175×10^{-9}	H
R1	3.050×10^{-1}	3.424×10^{-1}	1.223	ohm
Yo1	6.768×10^{-4}	1.097	2.568	S*s^a
a1	8.812×10^{-1}	7.010×10^{-1}	7.000×10^{-1}	
Ru	4.484×10^{-1}	7.740×10^{-1}	8.714×10^{-1}	ohm
After 2550 mAh DCh				
L1	3.789×10^{-13}	3.335×10^{-11}	7.698×10^{-9}	H
R1	4.263×10^{-1}	3.254×10^{-1}	1.191	ohm
Yo1	1.330×10^{-3}	7.120×10^{-1}	2.335	S*s^a
a1	8.212×10^{-1}	7.010×10^{-1}	7.000×10^{-1}	
Ru	5.303×10^{-1}	9.565×10^{-1}	1.095	ohm

After 3400 mAh DCh				
L1	2.540 x 10^{-11}	1.261 x 10^{-11}	4.291 x 10^{-8}	H
R1	4.297 x 10^{-1}	4.353 x 10^{-1}	1.198	ohm
Yo1	1.706 x 10^{-3}	6.204 x 10^{-1}	2.126	S*s^a
a1	7.978 x 10^{-1}	7.010 x 10^{-1}	7.000 x 10^{-1}	
Ru	5.546 x 10^{-1}	9.888 x 10^{-1}	1.171	ohm
After 4250 mAh DCh				
L1	0.000	2.000 x 10^{-11}	2.153 x 10^{-8}	H
R1	4.398 x 10^{-1}	3.688 x 10^{-1}	1.223	ohm
Yo1	1.089 x 10^{-3}	1.995 x 10^{-1}	1.657	S*s^a
a1	8.389 x 10^{-1}	7.010 x 10^{-1}	7.000 x 10^{-1}	
Ru	7.433 x 10^{-1}	1.153	1.450	ohm
After 5100 mAh DCh				
L1	2.133 x 10^{-11}	3.948 x 10^{-11}	1.469 x 10^{-9}	H
R1	5.070 x 10^{-1}	4.947 x 10^{-1}	1.266	ohm
Yo1	2.297 x 10^{-3}	1.596 x 10^{-1}	1.718	S*s^a
a1	7.428 x 10^{-1}	7.010 x 10^{-1}	7.000 x 10^{-1}	
Ru	7.119 x 10^{-1}	1.308	1.737	ohm
After 5950 mAh DCh				
L1	3.308 x 10^{-11}	6.795 x 10^{-11}	4.752 x 10^{-9}	H
R1	5.658 x 10^{-1}	7.354 x 10^{-1}	1.305	ohm
Yo1	2.752 x 10^{-3}	1.411 x 10^{-1}	1.327	S*s^a
a1	7.133 x 10^{-1}	7.010 x 10^{-1}	7.000 x 10^{-1}	
Ru	8.257 x 10^{-1}	1.726	2.231	ohm
After 6560 mAh DCh				

L1	2.148 x 10^{-11}	3.522 x 10^{-11}	1.436 x 10^{-8}	H
R1	8.903 x 10^{-1}	9.221 x 10^{-1}	1.222	ohm
Yo1	2.007 x 10^{-3}	9.248 x 10^{-2}	1.218	S*s^a
a1	7.000 x 10^{-1}	7.010 x 10^{-1}	7.000 x 10^{-1}	
Ru	8.669 x 10^{-1}	1.632	2.366	ohm

C-size 85% $SOCl_2$ Batteries Fits				
100 SoC	**High Freq.**	**Middle freq.**	**Low Freq.**	
L1	4.557 x 10^{-8}	3.526 x 10^{-15}	1.764 x 10^{-7}	H
R1	1.479 x 10^{-1}	9.850 x 10^{-2}	1.228	ohm
Yo1	1.259 x 10^{-4}	2.695 x 10^{-1}	3.541	S*s^a
a1	8.441 x 10^{-1}	7.000 x 10^{-1}	7.000 x 10^{-1}	
Ru	2.699 x 10^{-1}	4.217 x 10^{-1}	5.373 x 10^{-1}	ohm
After 850 mAh DCh				
L1	3.478 x 10^{-8}	1.144 x 10^{-10}	1.409 x 10^{-9}	H
R1	2.685 x 10^{-1}	1.279 x 10^{-1}	1.436	ohm
Yo1	1.574 x 10^{-4}	9.422 x 10^{-1}	3.516	S*s^a
a1	7.971 x 10^{-1}	7.000 x 10^{-1}	7.002 x 10^{-1}	
Ru	2.901 x 10^{-1}	5.720 x 10^{-1}	6.393 x 10^{-1}	ohm
After 1800 mAh DCh				
L1	4.273 x 10^{-8}	2.461 x 10^{-9}	1.068 x 10^{-6}	H
R1	3.293 x 10^{-1}	3.288 x 10^{-1}	8.748 x 10^{-1}	ohm
Yo1	4.915 x 10^{-4}	1.357	4.801	S*s^a
a1	7.000 x 10^{-1}	7.000 x 10^{-1}	7.472 x 10^{-1}	
Ru	2.114 x 10^{-1}	5.669 x 10^{-1}	6.609 x 10^{-1}	ohm

After 2700 mAh DCh				
L1	2.425 x 10^{-14}	8.953 x 10^{-10}	4.137 x 10^{-8}	H
R1	3.351 x 10^{-1}	3.707 x 10^{-1}	6.688 x 10^{-1}	ohm
Yo1	5.095 x 10^{-4}	1.271	8.168	S*s^a
a1	8.147 x 10^{-1}	7.000 x 10^{-1}	8.379 x 10^{-1}	
Ru	3.078 x 10^{-1}	7.115 x 10^{-1}	8.886 x 10^{-1}	ohm
After 3600 mAh DCh				
L1	1.441 x 10^{-13}	2.429 x 10^{-8}	5.415 x 10^{-7}	H
R1	3.380 x 10^{-1}	3.494 x 10^{-1}	7.086 x 10^{-1}	ohm
Yo1	4.220 x 10^{-4}	9.045 x 10^{-1}	7.414	S*s^a
a1	8.214 x 10^{-1}	7.000 x 10^{-1}	7.639 x 10^{-1}	
Ru	3.450 x 10^{-1}	7.589 x 10^{-1}	9.141 x 10^{-1}	ohm

C-size 15% $SOCl_2$ Batteries Fits				
100 SoC	**High Freq.**	**Middle freq.**	**Low Freq.**	
L1	8.879 x 10^{-8}	6.149 x 10^{-10}	3.181 x 10^{-8}	H
R1	1.001 x 10^{-1}	1.219 x 10^{-1}	1.680	ohm
Yo1	4.961 x 10^{-4}	2.883 x 10^{-1}	3.103	S*s^a
a1	8.784 x 10^{-1}	7.000 x 10^{-1}	7.000 x 10^{-1}	
Ru	3.227 x 10^{-1}	4.194 x 10^{-1}	5.727 x 10^{-1}	ohm
After 850 mAh DCh				
L1	6.518 x 10^{-8}	3.109 x 10^{-12}	3.263 x 10^{-9}	H
R1	1.328 x 10^{-1}	9.447 x 10^{-2}	9.092 x 10^{-1}	ohm
Yo1	4.029 x 10^{-4}	3.024 x 10^{-1}	2.944	S*s^a
a1	8.191 x 10^{-1}	7.006 x 10^{-1}	7.000 x 10^{-1}	

Ru	2.940 x 10^{-1}	4.374 x 10^{-1}	6.074 x 10^{-1}	ohm
After 1700 mAh DCh				
L1	6.062 x 10^{-8}	4.002 x 10^{-7}	2.588 x 10^{-10}	H
R1	2.095 x 10^{-1}	1.038 x 10^{-1}	8.173 x 10^{-1}	ohm
Yo1	3.017 x 10^{-4}	4.097 x 10^{-1}	2.419	S*s^a
a1	8.286 x 10^{-1}	7.000 x 10^{-1}	7.000 x 10^{-1}	
Ru	2.946 x 10^{-1}	5.136 x 10^{-1}	6.006 x 10^{-1}	ohm
After 2550 mAh DCh				
L1	5.742 x 10^{-8}	1.419 x 10^{-7}	2.698 x 10^{-11}	H
R1	2.735 x 10^{-1}	9.786 x 10^{-2}	6.536 x 10^{-1}	ohm
Yo1	2.021 x 10^{-4}	2.616 x 10^{-1}	2.179	S*s^a
a1	8.997 x 10^{-1}	7.313 x 10^{-1}	7.000 x 10^{-1}	
Ru	2.574 x 10^{-1}	5.261 x 10^{-1}	6.220 x 10^{-1}	ohm
After 3400 mAh DCh				
L1	4.768 x 10^{-8}	6.892 x 10^{-11}	1.882 x 10^{-7}	H
R1	3.928 x 10^{-1}	2.459 x 10^{-1}	8.793 x 10^{-1}	ohm
Yo1	1.503 x 10^{-4}	4.503 x 10^{-1}	9.602 x 10^{-1}	S*s^a
a1	8.996 x 10^{-1}	7.000 x 10^{-1}	7.000 x 10^{-1}	
Ru	2.102 x 10^{-1}	6.190 x 10^{-1}	6.782 x 10^{-1}	ohm
After 4250 mAh DCh				
L1	4.694 x 10^{-8}	9.365 x 10^{-10}	3.587 x 10^{-8}	H
R1	3.906 x 10^{-1}	4.452 x 10^{-1}	9.191 x 10^{-1}	ohm
Yo1	1.454 x 10^{-4}	6.319 x 10^{-1}	1.101	S*s^a
a1	9.033 x 10^{-1}	7.000 x 10^{-1}	7.000 x 10^{-1}	
Ru	2.115 x 10^{-1}	6.345 x 10^{-1}	7.117 x 10^{-1}	ohm

After 5100 mAh DCh				
L1	5.789 x 10^{-13}	1.557 x 10^{-10}	1.504 x 10^{-9}	H
R1	4.257 x 10^{-1}	5.857 x 10^{-1}	9.704 x 10^{-1}	ohm
Yo1	3.347 x 10^{-4}	3.048 x 10^{-2}	2.930 x 10^{-1}	S*s^a
a1	8.372 x 10^{-1}	7.000 x 10^{-1}	7.000 x 10^{-1}	
Ru	2.069 x 10^{-1}	5.666 x 10^{-1}	9.721 x 10^{-1}	ohm
After 5950 mAh DCh				
L1	9.150 x 10^{-13}	7.617 x 10^{-11}	1.165 x 10^{-9}	H
R1	1.521	1.630	1.404	ohm
Yo1	3.984 x 10^{-4}	1.216 x 10^{-3}	4.230 x 10^{-2}	S*s^a
a1	7.000 x 10^{-1}	7.000 x 10^{-1}	7.000 x 10^{-1}	
Ru	2.322 x 10^{-1}	7.125 x 10^{-1}	2.204	ohm

D-size 100% $SOCl_2$ Batteries Fits				
100 SoC	High Freq.	Middle freq.	Low Freq.	
L1	1.664 x 10^{-7}	5.296 x 10^{-12}	2.312 x 10^{-8}	H
R1	3.319 x 10^{-1}	1.844 x 10^{-1}	1.419	ohm
Yo1	3.047 x 10^{-4}	3.117 x 10^{-1}	5.870	S*s^a
a1	8.113 x 10^{-1}	7.010 x 10^{-1}	7.000 x 10^{-1}	
Ru	3.447 x 10^{-1}	6.660 x 10^{-1}	8.362 x 10^{-1}	ohm
After 1850 mAh DCh				
L1	1.718 x 10^{-7}	1.859 x 10^{-13}	1.023 x 10^{-9}	H
R1	2.434 x 10^{-1}	6.009 x 10^{-2}	8.192 x 10^{-1}	ohm
Yo1	1.297 x 10^{-3}	2.148 x 10^{-1}	5.141	S*s^a
a1	7.167 x 10^{-1}	7.010 x 10^{-1}	7.000 x 10^{-1}	

Ru	3.429×10^{-1}	5.590×10^{-1}	6.383×10^{-1}	ohm
After 3700 mAh DCh				
L1	9.492×10^{-8}	3.554×10^{-12}	2.707×10^{-10}	H
R1	1.637×10^{-1}	8.479×10^{-2}	8.557×10^{-1}	ohm
Yo1	2.141×10^{-3}	2.383×10^{-1}	4.027	S*s^a
a1	7.608×10^{-1}	7.010×10^{-1}	7.000×10^{-1}	
Ru	4.327×10^{-1}	5.711×10^{-1}	6.596×10^{-1}	ohm
After 5500 mAh DCh				
L1	4.497×10^{-12}	5.111×10^{-12}	1.423×10^{-8}	H
R1	3.122×10^{-1}	2.427×10^{-1}	8.427×10^{-1}	ohm
Yo1	1.477×10^{-3}	1.829	4.741	S*s^a
a1	8.522×10^{-1}	7.010×10^{-1}	7.000×10^{-1}	
Ru	4.502×10^{-1}	7.675×10^{-1}	8.302×10^{-1}	ohm
After 7400 mAh DCh				
L1	1.699×10^{-12}	3.978×10^{-11}	9.655×10^{-10}	H
R1	3.156×10^{-1}	1.787×10^{-1}	8.441×10^{-1}	ohm
Yo1	1.888×10^{-3}	8.131×10^{-1}	4.108	S*s^a
a1	8.318×10^{-1}	7.010×10^{-1}	7.000×10^{-1}	
Ru	4.979×10^{-1}	8.004×10^{-1}	9.076×10^{-1}	ohm
After 9200 mAh DCh				
L1	1.320×10^{-11}	1.897×10^{-11}	7.285×10^{-9}	H
R1	2.943×10^{-1}	1.894×10^{-1}	8.477×10^{-1}	ohm
Yo1	2.079×10^{-3}	5.033×10^{-1}	4.013	S*s^a
a1	8.291×10^{-1}	7.010×10^{-1}	7.000×10^{-1}	
Ru	5.238×10^{-1}	7.941×10^{-1}	9.481×10^{-1}	ohm

After 11100 mAh DCh				
L1	1.012 x 10^{-12}	1.687 x 10^{-11}	4.006 x 10^{-10}	H
R1	3.688 x 10^{-1}	2.580 x 10^{-1}	8.531 x 10^{-1}	ohm
Yo1	2.381 x 10^{-3}	4.456 x 10^{-1}	3.326	S*s^a
a1	8.104 x 10^{-1}	7.010 x 10^{-1}	7.000 x 10^{-1}	
Ru	5.870 x 10^{-1}	9.209 x 10^{-1}	1.100	ohm
After 12900 mAh DCh				
L1	4.532 x 10^{-13}	3.077 x 10^{-11}	2.082 x 10^{-8}	H
R1	3.553 x 10^{-1}	2.965 x 10^{-1}	8.775 x 10^{-1}	ohm
Yo1	2.371 x 10^{-3}	3.582 x 10^{-1}	3.680	S*s^a
a1	7.928 x 10^{-1}	7.010 x 10^{-1}	7.000 x 10^{-1}	
Ru	5.901 x 10^{-1}	9.081 x 10^{-1}	1.166	ohm
After 14800 mAh DCh				
L1	9.640 x 10^{-13}	1.101 x 10^{-11}	1.075 x 10^{-5}	H
R1	4.340 x 10^{-1}	3.836 x 10^{-1}	8.658 x 10^{-1}	ohm
Yo1	2.621 x 10^{-3}	2.571 x 10^{-1}	3.821	S*s^a
a1	7.490 x 10^{-1}	7.010 x 10^{-1}	7.000 x 10^{-1}	
Ru	6.335 x 10^{-1}	1.011	1.358	ohm
After 16600 mAh DCh				
L1	1.058 x 10^{-15}	1.244 x 10^{-11}	1.002 x 10^{-2}	H
R1	7.258 x 10^{-1}	6.945 x 10^{-1}	9.065 x 10^{-1}	ohm
Yo1	2.044 x 10^{-3}	1.534 x 10^{-1}	2.922	S*s^a
a1	7.000 x 10^{-1}	7.010 x 10^{-1}	7.000 x 10^{-1}	
Ru	8.247 x 10^{-1}	1.457	2.069	ohm

D-size 85% $SOCl_2$ Batteries Fits				
100 SoC	High Freq.	Middle freq.	Low Freq.	
L1	0.000	4.005 x 10^{-12}	7.702 x 10^{-9}	H
R1	1.465 x 10^{-1}	9.231 x 10^{-2}	1.149	ohm
Yo1	6.754 x 10^{-5}	8.880 x 10^{-2}	5.625	S*s^a
a1	9.685 x 10^{-1}	7.835 x 10^{-1}	7.000 x 10^{-1}	
Ru	4.693 x 10^{-1}	6.395 x 10^{-1}	7.692 x 10^{-1}	ohm
After 1800 mAh DCh				
L1	1.803 x 10^{-7}	1.560 x 10^{-11}	1.955 x 10^{-9}	H
R1	2.276 x 10^{-1}	6.133 x 10^{-2}	1.115	ohm
Yo1	2.150 x 10^{-4}	2.214 x 10^{-1}	5.957	S*s^a
a1	7.746 x 10^{-1}	7.000 x 10^{-1}	7.000 x 10^{-1}	
Ru	2.922 x 10^{-1}	5.165 x 10^{-1}	6.068 x 10^{-1}	ohm
After 3600 mAh DCh				
L1	1.729 x 10^{-7}	5.176 x 10^{-7}	1.702 x 10^{-9}	H
R1	2.138 x 10^{-1}	5.990 x 10^{-2}	6.832 x 10^{-1}	ohm
Yo1	2.791 x 10^{-4}	1.851 x 10^{-1}	5.679	S*s^a
a1	8.059 x 10^{-1}	7.000 x 10^{-1}	7.000 x 10^{-1}	
Ru	2.858 x 10^{-1}	4.903 x 10^{-1}	6.108 x 10^{-1}	ohm
After 5400 mAh DCh				
L1	8.343 x 10^{-8}	1.500 x 10^{-8}	3.405 x 10^{-2}	H
R1	1.967 x 10^{-1}	2.834 x 10^{-1}	4.811 x 10^{-1}	ohm
Yo1	6.543 x 10^{-4}	2.436	9.994	S*s^a
a1	8.251 x 10^{-1}	7.000 x 10^{-1}	8.663 x 10^{-1}	
Ru	3.026 x 10^{-1}	5.347 x 10^{-1}	6.601 x 10^{-1}	ohm

After 7200 mAh DCh				
L1	1.276 x 10^{-7}	2.378 x 10^{-9}	5.535 x 10^{-3}	H
R1	2.002 x 10^{-1}	2.950 x 10^{-1}	2.933 x 10^{-1}	ohm
Yo1	5.249 x 10^{-4}	1.956	1.904 x 10^{1}	S*s^a
a1	8.229 x 10^{-1}	7.000 x 10^{-1}	1.000	
Ru	3.249 x 10^{-1}	5.650 x 10^{-1}	7.402 x 10^{-1}	ohm
After 9000 mAh DCh				
L1	1.472 x 10^{-7}	1.537 x 10^{-9}	3.808 x 10^{-2}	H
R1	1.789 x 10^{-1}	3.071 x 10^{-1}	3.407 x 10^{-1}	ohm
Yo1	8.453 x 10^{-4}	1.150	1.111 x 10^{1}	S*s^a
a1	8.110 x 10^{-1}	7.000 x 10^{-1}	9.379 x 10^{-1}	
Ru	2.962 x 10^{-1}	5.135 x 10^{-1}	7.308 x 10^{-1}	ohm
After 10800 mAh DCh				
L1	1.841 x 10^{-7}	1.404 x 10^{-8}	7.079 x 10^{-1}	H
R1	1.858 x 10^{-1}	3.602 x 10^{-1}	1.266	ohm
Yo1	1.513 x 10^{-3}	7.679 x 10^{-1}	8.587 x 10^{-1}	S*s^a
a1	7.548 x 10^{-1}	7.000 x 10^{-1}	7.608 x 10^{-1}	
Ru	3.106 x 10^{-1}	5.582 x 10^{-1}	5.399 x 10^{-5}	ohm

D-size 15% $SOCl_2$ Batteries Fits				
100 SoC	High Freq.	Middle freq.	Low Freq.	
L1	1.684 x 10^{-7}	6.759 x 10^{-13}	8.334 x 10^{-9}	H
R1	8.916 x 10^{-2}	1.574 x 10^{-1}	1.543	ohm
Yo1	7.808 x 10^{-4}	4.332 x 10^{-1}	4.873	S*s^a
a1	8.257 x 10^{-1}	7.100 x 10^{-1}	7.000 x 10^{-1}	

Ru	3.776 x 10^{-1}	4.656 x 10^{-1}	6.260 x 10^{-1}	ohm
After 1800 mAh DCh				
L1	1.874 x 10^{-7}	7.749 x 10^{-12}	1.010 x 10^{-9}	H
R1	1.309 x 10^{-1}	1.741 x 10^{-1}	5.589 x 10^{-1}	ohm
Yo1	2.837 x 10^{-4}	1.223	3.258	S*s^a
a1	8.032 x 10^{-1}	7.100 x 10^{-1}	7.000 x 10^{-1}	
Ru	3.775 x 10^{-1}	5.283 x 10^{-1}	5.927 x 10^{-1}	ohm
After 3600 mAh DCh				
L1	1.765 x 10^{-7}	7.331 x 10^{-13}	1.006 x 10^{-10}	H
R1	1.325 x 10^{-1}	7.869 x 10^{-2}	4.465 x 10^{-1}	ohm
Yo1	2.594 x 10^{-4}	9.302 x 10^{-1}	3.250	S*s^a
a1	8.523 x 10^{-1}	7.100 x 10^{-1}	7.005 x 10^{-1}	
Ru	3.036 x 10^{-1}	4.499 x 10^{-1}	4.896 x 10^{-1}	ohm
After 5400 mAh DCh				
L1	1.820 x 10^{-7}	2.061 x 10^{-12}	2.561 x 10^{-8}	H
R1	1.585 x 10^{-1}	1.201 x 10^{-1}	3.479 x 10^{-1}	ohm
Yo1	3.019 x 10^{-4}	1.020	3.916	S*s^a
a1	8.807 x 10^{-1}	7.100 x 10^{-1}	7.963 x 10^{-1}	
Ru	2.629 x 10^{-1}	4.254 x 10^{-1}	5.094 x 10^{-1}	ohm
After 7200 mAh DCh				
L1	1.788 x 10^{-7}	2.414 x 10^{-12}	1.179 x 10^{-9}	H
R1	3.059 x 10^{-1}	1.962 x 10^{-1}	3.734 x 10^{-1}	ohm
Yo1	1.643 x 10^{-4}	1.082	2.286	S*s^a
a1	9.223 x 10^{-1}	7.100 x 10^{-1}	7.000 x 10^{-1}	
Ru	2.403 x 10^{-1}	5.608 x 10^{-1}	6.069 x 10^{-1}	ohm

After 9000 mAh DCh				
L1	1.698×10^{-7}	7.687×10^{-13}	5.934×10^{-10}	H
R1	3.332×10^{-1}	2.204×10^{-1}	4.351×10^{-1}	ohm
Yo1	1.421×10^{-4}	4.491×10^{-1}	1.288	S*s^a
a1	9.175×10^{-1}	7.100×10^{-1}	7.000×10^{-1}	
Ru	2.228×10^{-1}	5.610×10^{-1}	6.443×10^{-1}	ohm
After 10800 mAh DCh				
L1	1.745×10^{-7}	1.030×10^{-12}	2.786×10^{-8}	H
R1	3.429×10^{-1}	2.716×10^{-1}	4.940×10^{-1}	ohm
Yo1	2.067×10^{-4}	2.207×10^{-1}	5.948×10^{-1}	S*s^a
a1	8.975×10^{-1}	7.100×10^{-1}	7.000×10^{-1}	
Ru	2.231×10^{-1}	5.596×10^{-1}	6.376×10^{-1}	ohm
After 12600 mAh DCh				
L1	1.540×10^{-7}	9.658×10^{-13}	6.116×10^{-9}	H
R1	2.681×10^{-1}	4.824×10^{-1}	4.096×10^{-1}	ohm
Yo1	5.878×10^{-4}	2.137×10^{-1}	1.401×10^{1}	S*s^a
a1	8.621×10^{-1}	7.100×10^{-1}	8.988×10^{-1}	
Ru	2.276×10^{-1}	4.957×10^{-1}	1.017	ohm
After 14400 mAh DCh				
L1	1.759×10^{-7}	8.994×10^{-13}	1.679×10^{-9}	H
R1	2.591×10^{-1}	5.222×10^{-1}	5.016×10^{-1}	ohm
Yo1	1.249×10^{-3}	3.436×10^{-2}	2.572×10^{-1}	S*s^a
a1	7.000×10^{-1}	7.100×10^{-1}	7.000×10^{-1}	
Ru	2.141×10^{-1}	4.477×10^{-1}	7.433×10^{-1}	ohm

List of Publications

This thesis includes the following publications of which I was an author:

1. Zabara, Mohammed Ahmed, Gokberk Katirci, and Burak Ulgut. "Operando investigations of the interfacial electrochemical kinetics of metallic lithium anodes via temperature-dependent electrochemical impedance spectroscopy." The Journal of Physical Chemistry C 126.27 (2022): 10968-10976.

2. Zabara, Mohammed Ahmed, Gökberk Katırcı, and Burak Ülgüt. "Nonlinear harmonics in EIS of batteries with lithium anodes: Proper controls and analysis." Electrochimica Acta 429 (2022): 140969.

3. Katırcı, Gökberk, Mohammed Ahmed Zabara, and Burak Ülgüt. "Methods—unexpected effects in galvanostatic EIS of Randles' cells: initial transients and harmonics generated." Journal of the Electrochemical Society 169.3 (2022): 030527.

4. Katırcı, Gökberk, et al. "Electrochemical Impedance Spectroscopy (EIS) and non-linear harmonic analysis (NHA) of Li-SOCl2/SO2Cl2 batteries." Electrochimica Acta (2024): 143984.

5. Zabara, Mohammed A., et al. "Insights into charge transfer dynamics of Li batteries through temperature-dependent electrochemical impedance spectroscopy (EIS) utilizing symmetric cell configuration." Electrochimica Acta 485 (2024): 144080.

Bibliography

[1] D. Linden, "Handbook of batteries," in *Fuel and energy abstracts*, vol. 4, p. 265, 1995.

[2] B. Zhu, X. Wang, P. Yao, J. Li, and J. Zhu, "Towards high energy density lithium battery anodes: silicon and lithium," *Chemical science*, vol. 10, no. 30, pp. 7132–7148, 2019.

[3] J. Besenhard and G. Eichinger, "High energy density lithium cells: Part i. electrolytes and anodes," *Journal of Electroanalytical Chemistry and Interfacial Electrochemistry*, vol. 68, no. 1, pp. 1–18, 1976.

[4] H. Xu, C. Han, W. Li, H. Li, and X. Qiu, "Quantification of lithium dendrite and solid electrolyte interphase (sei) in lithium-ion batteries," *Journal of Power Sources*, vol. 529, p. 231219, 2022.

[5] X. Han, Y. Gong, K. Fu, X. He, G. T. Hitz, J. Dai, A. Pearse, B. Liu, H. Wang, G. Rubloff, *et al.*, "Negating interfacial impedance in garnet-based solid-state li metal batteries," *Nature materials*, vol. 16, no. 5, pp. 572–579, 2017.

[6] B. M. Wiers, M.-L. Foo, N. P. Balsara, and J. R. Long, "A solid lithium electrolyte via addition of lithium isopropoxide to a metal–organic framework with open metal sites," *Journal of the American Chemical Society*, vol. 133, no. 37, pp. 14522–14525, 2011.

[7] L. Suo, Y.-S. Hu, H. Li, M. Armand, and L. Chen, "A new class of solvent-in-salt electrolyte for high-energy rechargeable metallic lithium batteries," *Nature communications*, vol. 4, no. 1, p. 1481, 2013.

[8] K. Doblhoff-Dier and M. T. Koper, "Modeling the gouy–chapman diffuse capacitance with attractive ion–surface interaction," *The Journal of Physical Chemistry C*, vol. 125, no. 30, pp. 16664–16673, 2021.

[9] A. J. Bard, L. R. Faulkner, *et al.*, "Fundamentals and applications," *Electrochemical methods*, vol. 2, no. 482, pp. 580–632, 2001.

[10] A. Ivanishchev and I. Ivanishcheva, "Ion transport in lithium electrochemical systems: problems and solutions," *Russian Journal of Electrochemistry*, vol. 56, pp. 907–928, 2020.

[11] K.-H. Chen, K. N. Wood, E. Kazyak, W. S. LePage, A. L. Davis, A. J. Sanchez, and N. P. Dasgupta, "Dead lithium: mass transport effects on voltage, capacity, and failure of lithium metal anodes," *Journal of Materials Chemistry A*, vol. 5, no. 23, pp. 11671–11681, 2017.

[12] F. F. Caserio, G. E. Dennis, R. H. DeWolfe, and W. G. Young, "The reaction of thionyl chloride with allylic alcohols1a," *Journal of the American Chemical Society*, vol. 77, no. 15, pp. 4182–4183, 1955.

[13] I. A. El-Sakka and N. A. Hassan, "Synthetic uses of thionyl chloride," *Journal of Sulfur Chemistry*, vol. 26, no. 1, pp. 33–97, 2005.

[14] D. D. Wirth, "Thionyl chloride," *Encyclopedia of Reagents for Organic Synthesis*, 2001.

[15] C. S. Yeung, P. L. Ng, X. Guan, and D. L. Phillips, "Water-assisted dehalogenation of thionyl chloride in the presence of water molecules," *The Journal of Physical Chemistry A*, vol. 114, no. 12, pp. 4123–4130, 2010.

[16] H. North and A. Hageman, "The action of thionyl chloride on metals and metalloids.," *Journal of the American Chemical Society*, vol. 34, no. 7, pp. 890–894, 1912.

[17] E. Markevich, G. Salitra, F. Chesneau, M. Schmidt, and D. Aurbach, "Very stable lithium metal stripping–plating at a high rate and high areal capacity in fluoroethylene carbonate-based organic electrolyte solution," *ACS Energy Letters*, vol. 2, no. 6, pp. 1321–1326, 2017.

[18] D. Aurbach, E. Zinigrad, Y. Cohen, and H. Teller, "A short review of failure mechanisms of lithium metal and lithiated graphite anodes in liquid electrolyte solutions," *Solid state ionics*, vol. 148, no. 3-4, pp. 405–416, 2002.

[19] P. Verma, P. Maire, and P. Novák, "A review of the features and analyses of the solid electrolyte interphase in li-ion batteries," *Electrochimica Acta*, vol. 55, no. 22, pp. 6332–6341, 2010.

[20] A. Wang, S. Kadam, H. Li, S. Shi, and Y. Qi, "Review on modeling of the anode solid electrolyte interphase (sei) for lithium-ion batteries," *npj Computational Materials*, vol. 4, no. 1, pp. 1–26, 2018.

[21] D. Aurbach, "Review of selected electrode–solution interactions which determine the performance of li and li ion batteries," *Journal of Power Sources*, vol. 89, no. 2, pp. 206–218, 2000.

[22] M. E. Orazem and B. Tribollet, *Electrochemical Impedance Spectroscopy, Second Edition*. Wiley, 2017.

[23] A. C. Lazanas and M. I. Prodromidis, "Electrochemical impedance spectroscopy: A tutorial," *ACS Measurement Science Au*, 2023.

[24] M. T. Koper, "Stability study and categorization of electrochemical oscillators by impedance spectroscopy," *Journal of Electroanalytical Chemistry*, vol. 409, no. 1-2, pp. 175–182, 1996.

[25] P. Agarwal, M. E. Orazem, and L. H. Garcia-Rubio, "Application of measurement models to impedance spectroscopy: Iii. evaluation of consistency with the kramers-kronig relations," *Journal of the Electrochemical Society*, vol. 142, no. 12, p. 4159, 1995.

[26] M. Durbha, M. E. Orazem, and L. H. García-Rubio, "Spectroscopy applications of the kramers-kronig transforms: Implications for error structure identification," *Journal of the Electrochemical Society*, vol. 144, no. 1, p. 48, 1997.

[27] M. E. Orazem, P. Agarwal, and L. H. Garcia-Rubio, "Critical issues associated with interpretation of impedance spectra," *Journal of Electroanalytical Chemistry*, vol. 378, no. 1-2, pp. 51–62, 1994.

[28] H. Liao, W. Watson, A. Dizon, B. Tribollet, V. Vivier, and M. E. Orazem, "Physical properties obtained from measurement model analysis of impedance measurements," *Electrochimica Acta*, vol. 354, p. 136747, 2020.

[29] M. E. Orazem, "Measurement model for analysis of electrochemical impedance data," *Journal of Solid State Electrochemistry*, vol. 28, no. 3, pp. 1273–1289, 2024.

[30] W. Watson and M. E. Orazem, "Eis: measurement model program," 2020.

[31] M. E. Orazem, P. Shukla, and M. A. Membrino, "Extension of the measurement model approach for deconvolution of underlying distributions for impedance measurements," *Electrochimica Acta*, vol. 47, no. 13-14, pp. 2027–2034, 2002.

[32] B. A. Boukamp, "A linear kronig-kramers transform test for immittance data validation," *Journal of the electrochemical society*, vol. 142, no. 6, p. 1885, 1995.

[33] J. E. B. Randles, "Kinetics of rapid electrode reactions," *Discussions of the faraday society*, vol. 1, pp. 11–19, 1947.

[34] M. E. Orazem and B. Ulgut, "On the proper use of a warburg impedance," *Journal of The Electrochemical Society*, 2024.

[35] B. Hirschorn, M. E. Orazem, B. Tribollet, V. Vivier, I. Frateur, and M. Musiani, "Constant-phase-element behavior caused by resistivity distributions in films," *ECS Transactions*, vol. 28, no. 24, p. 77, 2010.

[36] M. Martin and A. Lasia, "Influence of experimental factors on the constant phase element behavior of pt electrodes," *Electrochimica Acta*, vol. 56, no. 23, pp. 8058–8068, 2011.

[37] A. Lasia, "The origin of the constant phase element," *The Journal of Physical Chemistry Letters*, vol. 13, no. 2, pp. 580–589, 2022.

[38] Y. B. Amor, E. Sutter, H. Takenouti, M. E. Orazem, and B. Tribollet, "Interpretation of electrochemical impedance for corrosion of a coated silver film in terms of a pore-in-pore model," *Journal of The Electrochemical Society*, vol. 161, no. 14, p. C573, 2014.

[39] J. Huang, Z. Li, B. Y. Liaw, and J. Zhang, "Graphical analysis of electrochemical impedance spectroscopy data in bode and nyquist representations," *Journal of Power Sources*, vol. 309, pp. 82–98, 2016.

[40] G. Katırcı, M. A. Zabara, and B. Ulgut, "Methods—unexpected effects in galvanostatic eis of randles' cells: Initial transients and harmonics generated," *Journal of The Electrochemical Society*, 2022.

[41] M. A. Zabara, G. Katırcı, F. E. Civan, A. Yürüm, S. A. Gürsel, and B. Ülgüt, "Insights into charge transfer dynamics of li batteries through temperature-dependent electrochemical impedance spectroscopy (eis) utilizing symmetric cell configuration," *Electrochimica Acta*, p. 144080, 2024.

[42] B. Hirschorn, M. E. Orazem, B. Tribollet, V. Vivier, I. Frateur, and M. Musiani, "Determination of effective capacitance and film thickness from constant-phase-element parameters," *Electrochimica acta*, vol. 55, no. 21, pp. 6218–6227, 2010.

[43] G. Brug, A. L. van den Eeden, M. Sluyters-Rehbach, and J. H. Sluyters, "The analysis of electrode impedances complicated by the presence of a constant phase element," *Journal of electroanalytical chemistry and interfacial electrochemistry*, vol. 176, no. 1-2, pp. 275–295, 1984.

[44] M. E. Orazem, I. Frateur, B. Tribollet, V. Vivier, S. Marcelin, N. Pébère, A. L. Bunge, E. A. White, D. P. Riemer, and M. Musiani, "Dielectric

properties of materials showing constant-phase-element (cpe) impedance response," *Journal of The Electrochemical Society*, vol. 160, no. 6, p. C215, 2013.

[45] E. Van Gheem, R. Pintelon, J. Vereecken, J. Schoukens, A. Hubin, P. Verboven, and O. Blajiev, "Electrochemical impedance spectroscopy in the presence of non-linear distortions and non-stationary behaviour: Part i: Theory and validation," *Electrochimica Acta*, vol. 49, no. 26, pp. 4753–4762, 2004.

[46] F. Fasmin and R. Srinivasan, "Nonlinear electrochemical impedance spectroscopy," *Journal of The Electrochemical Society*, vol. 164, no. 7, p. H443, 2017.

[47] M. A. Zabara, C. B. Uzundal, and B. Ulgut, "Linear and nonlinear electrochemical impedance spectroscopy studies of li/socl2 batteries," *Journal of The Electrochemical Society*, vol. 166, no. 6, p. A811, 2019.

[48] M. Kiel, O. Bohlen, and D. Sauer, "Harmonic analysis for identification of nonlinearities in impedance spectroscopy," *Electrochimica Acta*, vol. 53, no. 25, pp. 7367–7374, 2008.

[49] R. Vedalakshmi, S. Manoharan, H.-W. Song, and N. Palaniswamy, "Application of harmonic analysis in measuring the corrosion rate of rebar in concrete," *Corrosion Science*, vol. 51, no. 11, pp. 2777–2789, 2009.

[50] T. Kadyk, R. Hanke-Rauschenbach, and K. Sundmacher, "Nonlinear frequency response analysis of pem fuel cells for diagnosis of dehydration, flooding and co-poisoning," *Journal of Electroanalytical Chemistry*, vol. 630, no. 1-2, pp. 19–27, 2009.

[51] C. R. Harris, K. J. Millman, S. J. van der Walt, R. Gommers, P. Virtanen, D. Cournapeau, E. Wieser, J. Taylor, S. Berg, N. J. Smith, *et al.*, "Array programming with numpy," *Nature*, vol. 585, no. 7825, pp. 357–362, 2020.

[52] J. D. Hunter, "Matplotlib: A 2d graphics environment," *Computing in science & engineering*, vol. 9, no. 03, pp. 90–95, 2007.

[53] P. Virtanen, R. Gommers, T. E. Oliphant, M. Haberland, T. Reddy, D. Cournapeau, E. Burovski, P. Peterson, W. Weckesser, J. Bright, *et al.*, "Scipy 1.0: fundamental algorithms for scientific computing in python," *Nature methods*, vol. 17, no. 3, pp. 261–272, 2020.

[54] T. Vidaković-Koch, T. Miličić, L. A. Živković, H. S. Chan, U. Krewer, and M. Petkovska, "Nonlinear frequency response analysis: a recent review and perspectives," *Current Opinion in Electrochemistry*, vol. 30, p. 100851, 2021.

[55] M. D. Murbach, V. W. Hu, and D. T. Schwartz, "Nonlinear electrochemical impedance spectroscopy of lithium-ion batteries: experimental approach, analysis, and initial findings," *Journal of the Electrochemical Society*, vol. 165, no. 11, p. A2758, 2018.

[56] N. Harting, N. Wolff, F. Röder, and U. Krewer, "Nonlinear frequency response analysis (nfra) of lithium-ion batteries," *Electrochimica Acta*, vol. 248, pp. 133–139, 2017.

[57] N. Harting, N. Wolff, and U. Krewer, "Identification of lithium plating in lithium-ion batteries using nonlinear frequency response analysis (nfra)," *Electrochimica Acta*, vol. 281, pp. 378–385, 2018.

[58] N. Wolff, N. Harting, M. Heinrich, F. Röder, and U. Krewer, "Nonlinear frequency response analysis on lithium-ion batteries: a model-based assessment," *Electrochimica Acta*, vol. 260, pp. 614–622, 2018.

[59] B. Liebhart, M. Satzke, L. Komsiyska, and C. Endisch, "Application of nonlinear impedance spectroscopy for the diagnosis of lithium-ion battery cells under various operating conditions," *Journal of Power Sources*, vol. 480, p. 228673, 2020.

[60] M. A. Zabara, G. Katırcı, and B. Ulgut, "Operando investigations of the interfacial electrochemical kinetics of metallic lithium anodes via temperature-dependent electrochemical impedance spectroscopy," *The Journal of Physical Chemistry C*, vol. 126, no. 27, pp. 10968–10976, 2022.

[61] T. Abe, H. Fukuda, Y. Iriyama, and Z. Ogumi, "Solvated li-ion transfer at interface between graphite and electrolyte," *Journal of the Electrochemical Society*, vol. 151, no. 8, p. A1120, 2004.

[62] N.-W. Li, Y.-X. Yin, C.-P. Yang, and Y.-G. Guo, "An artificial solid electrolyte interphase layer for stable lithium metal anodes," *Advanced materials*, vol. 28, no. 9, pp. 1853–1858, 2016.

[63] S. K. Heiskanen, J. Kim, and B. L. Lucht, "Generation and evolution of the solid electrolyte interphase of lithium-ion batteries," *Joule*, vol. 3, no. 10, pp. 2322–2333, 2019.

[64] T. Krauskopf, R. Dippel, H. Hartmann, K. Peppler, B. Mogwitz, F. H. Richter, W. G. Zeier, and J. Janek, "Lithium-metal growth kinetics on llzo garnet-type solid electrolytes," *Joule*, vol. 3, no. 8, pp. 2030–2049, 2019.

[65] W. Choi, H.-C. Shin, J. M. Kim, J.-Y. Choi, and W.-S. Yoon, "Modeling and applications of electrochemical impedance spectroscopy (eis) for lithium-ion batteries," *Journal of Electrochemical Science and Technology*, vol. 11, no. 1, pp. 1–13, 2020.

[66] S. E. Li, B. Wang, H. Peng, and X. Hu, "An electrochemistry-based impedance model for lithium-ion batteries," *Journal of Power Sources*, vol. 258, pp. 9–18, 2014.

[67] X. Zhou, J. Huang, Z. Pan, and M. Ouyang, "Impedance characterization of lithium-ion batteries aging under high-temperature cycling: Importance of electrolyte-phase diffusion," *Journal of Power Sources*, vol. 426, pp. 216–222, 2019.

[68] T. Osaka, T. Momma, D. Mukoyama, and H. Nara, "Proposal of novel equivalent circuit for electrochemical impedance analysis of commercially available lithium ion battery," *Journal of Power Sources*, vol. 205, pp. 483–486, 2012.

[69] Q.-C. Zhuang, T. Wei, L.-L. Du, Y.-L. Cui, L. Fang, and S.-G. Sun, "An electrochemical impedance spectroscopic study of the electronic and ionic transport properties of spinel limn2o4," *The Journal of Physical Chemistry C*, vol. 114, no. 18, pp. 8614–8621, 2010.

[70] F. Croce, F. Nobili, A. Deptula, W. Lada, R. Tossici, A. D'epifanio, B. Scrosati, and R. Marassi, "An electrochemical impedance spectroscopic study of the transport properties of lini0. 75co0. 25o2," *Electrochemistry communications*, vol. 1, no. 12, pp. 605–608, 1999.

[71] F. Langer, M. S. Palagonia, I. Bardenhagen, J. Glenneberg, F. La Mantia, and R. Kun, "Impedance spectroscopy analysis of the lithium ion transport through the li7la3zr2o12/p (eo) 20li interface," *Journal of The Electrochemical Society*, vol. 164, no. 12, p. A2298, 2017.

[72] B. T. Habte and F. Jiang, "Effect of microstructure morphology on li-ion battery graphite anode performance: Electrochemical impedance spectroscopy modeling and analysis," *Solid State Ionics*, vol. 314, pp. 81–91, 2018.

[73] A. R. Bredar, A. L. Chown, A. R. Burton, and B. H. Farnum, "Electrochemical impedance spectroscopy of metal oxide electrodes for energy applications," *ACS Applied Energy Materials*, vol. 3, no. 1, pp. 66–98, 2020.

[74] R. Tatara, P. Karayaylali, Y. Yu, Y. Zhang, L. Giordano, F. Maglia, R. Jung, J. P. Schmidt, I. Lund, and Y. Shao-Horn, "The effect of electrode-electrolyte interface on the electrochemical impedance spectra for positive electrode in li-ion battery," *Journal of The Electrochemical Society*, vol. 166, no. 3, pp. A5090–A5098, 2019.

[75] L. Wang, J. Zhao, X. He, J. Gao, J. Li, C. Wan, and C. Jiang, "Electrochemical impedance spectroscopy (eis) study of lini1/3co1/3mn1/3o2 for li-ion batteries," *Int. J. Electrochem. Sci*, vol. 7, no. 1, pp. 345–353, 2012.

[76] J. Landesfeind and H. A. Gasteiger, "Temperature and concentration dependence of the ionic transport properties of lithium-ion battery electrolytes," *Journal of The Electrochemical Society*, vol. 166, no. 14, pp. A3079–A3097, 2019.

[77] M. A. Zabara, H. Göçmez, A. Karabatak, and B. Ulgut, "Characterization of different electrolyte composition lithium thionyl chloride reserve battery by electrochemical impedance spectroscopy," *Journal of The Electrochemical Society*, vol. 168, no. 5, p. 050529, 2021.

[78] N. Schweikert, H. Hahn, and S. Indris, "Cycling behaviour of li/li 4 ti 5 o 12 cells studied by electrochemical impedance spectroscopy," *Physical Chemistry Chemical Physics*, vol. 13, no. 13, pp. 6234–6240, 2011.

[79] J. Song, H. Lee, Y. Wang, and C. Wan, "Two-and three-electrode impedance spectroscopy of lithium-ion batteries," *Journal of Power Sources*, vol. 111, no. 2, pp. 255–267, 2002.

[80] I. J. Gordon, S. Genies, G. S. Larbi, A. Boulineau, L. Daniel, and M. Alias, "Original implementation of electrochemical impedance spectroscopy (eis) in symmetric cells: Evaluation of post-mortem protocols applied to characterize electrode materials for li-ion batteries," *Journal of Power Sources*, vol. 307, pp. 788–795, 2016.

[81] D. Aurbach, M. D. Levi, E. Levi, H. Teller, B. Markovsky, G. Salitra, U. Heider, and L. Heider, "Common electroanalytical behavior of li intercalation processes into graphite and transition metal oxides," *Journal of the Electrochemical Society*, vol. 145, no. 9, p. 3024, 1998.

[82] T. Ong and H. Yang, "Symmetrical cell for electrochemical ac impedance studies of lithium intercalation into graphite," *Electrochemical and Solid-State Letters*, vol. 4, no. 7, p. A89, 2001.

[83] Y. Xia, Y. Zhou, and M. Yoshio, "Capacity fading on cycling of 4 v li/limn2 o 4 cells," *Journal of The Electrochemical Society*, vol. 144, no. 8, p. 2593, 1997.

[84] Q. Li, Z. Cao, W. Wahyudi, G. Liu, G.-T. Park, L. Cavallo, T. D. Anthopoulos, L. Wang, Y.-K. Sun, H. N. Alshareef, *et al.*, "Unraveling the new role of an ethylene carbonate solvation shell in rechargeable metal ion batteries," *ACS Energy Letters*, vol. 6, no. 1, pp. 69–78, 2020.

[85] A. Andersson, D. Abraham, R. Haasch, S. MacLaren, J. Liu, and K. Amine, "Surface characterization of electrodes from high power lithium-ion batteries," *Journal of The Electrochemical Society*, vol. 149, no. 10, p. A1358, 2002.

[86] S. Zhang, T. Jow, K. Amine, and G. Henriksen, "Lipf6–ec–emc electrolyte for li-ion battery," *Journal of Power Sources*, vol. 107, no. 1, pp. 18–23, 2002.

[87] S. S. Zhang, K. Xu, and T. Jow, "Understanding formation of solid electrolyte interface film on limn2 o 4 electrode," *Journal of The Electrochemical Society*, vol. 149, no. 12, p. A1521, 2002.

[88] L. Wang, J. Qiu, X. Wang, L. Chen, G. Cao, J. Wang, H. Zhang, and X. He, "Insights for understanding multiscale degradation of lifepo4 cathodes," *EScience*, vol. 2, no. 2, pp. 125–137, 2022.

[89] T. B. Reddy and D. Linden, "Linden's handbook of batteries," *(No Title)*, 2011.

[90] M. A. Zabara and B. Ulgut, "Electrochemical impedance spectroscopy based voltage modeling of lithium thionyl chloride (li\ socl2) primary battery at arbitrary discharge," *Electrochimica Acta*, vol. 334, p. 135584, 2020.

[91] M. A. M. Zabara, *Electrochemical impedance spectroscopy based characterization and modeling of electrochemical energy storage systems*. PhD thesis, Bilkent University, 2021.

[92] M. B. Mogensen and E. Hennesø, "Properties and structure of the licl-films on lithium anodes in liquid cathodes," *Acta Chimica Slovenica*, vol. 63, no. 3, pp. 519–534, 2016.

[93] C.-H. Kim and S.-I. Pyun, "Growth kinetics of lithium chloride layer formed on porous carbon cathodes during discharge of li socl2 batteries," *Journal of the Electrochemical Society*, vol. 150, no. 9, p. A1176, 2003.

[94] D. Eder and R. Kramer, "Electric impedance spectroscopy of titania: Influence of gas treatment and of surface area," *The Journal of Physical Chemistry B*, vol. 108, no. 39, pp. 14823–14829, 2004.

[95] G. Katırcı, F. E. Civan, S. Jung, C. B. Lee, and B. Ülgüt, "Electrochemical impedance spectroscopy (eis) and non-linear harmonic analysis (nha) of li-socl2/so2cl2 batteries," *Electrochimica Acta*, p. 143984, 2024.

[96] Y.-H. Chiang, W.-Y. Sean, and J.-C. Ke, "Online estimation of internal resistance and open-circuit voltage of lithium-ion batteries in electric vehicles," *Journal of Power Sources*, vol. 196, no. 8, pp. 3921–3932, 2011.

[97] M. A. Zabara, G. Katırcı, and B. Ülgüt, "Non-linear harmonics in eis of batteries with lithium anodes: Proper controls and analysis," *Electrochimica Acta*, vol. 429, p. 140969, 2022.

[98] M. D. Murbach and D. T. Schwartz, "Extending newman's pseudo-two-dimensional lithium-ion battery impedance simulation approach to include the nonlinear harmonic response," *Journal of The Electrochemical Society*, vol. 164, no. 11, p. E3311, 2017.

[99] T. L. Kirk, A. Lewis-Douglas, D. Howey, C. P. Please, and S. J. Chapman, "Nonlinear electrochemical impedance spectroscopy for lithium-ion battery model parameterization," *Journal of The Electrochemical Society*, vol. 170, no. 1, p. 010514, 2023.

[100] R. M. French, *Engineering the guitar: theory and practice*. Springer, 2009.

[101] A. R. Duchossoir, *The Fender Telecaster: The Detailed Story of America's Senior Solid Body Electric Guitar*. Hal Leonard Corporation, 1991.

[102] D. Hunter, *The Fender Telecaster: The Life and Times of the Electric Guitar That Changed the World*. Voyageur Press (MN), 2012.

[103] P. Atkinson, *Amplified: A Design History of the Electric Guitar*. Reaktion Books, 2020.

[104] C. Gough, "Electric guitar and violin," *The science of string instruments*, pp. 393–415, 2010.

[105] R. C. Paiva, J. Pakarinen, and V. Välimäki, "Acoustics and modeling of pickups," *Journal of the Audio Engineering Society*, vol. 60, no. 10, pp. 768–782, 2012.

[106] T. Jungmann, "Theoretical and practical studies on the behavior of electric guitar pick-ups," *Helsinki University of Technology, Helsinki, Finland (1994 Nov.)*, 1994.

[107] G. Lemarquand and V. Lemarquand, "Calculation method of permanent-magnet pickups for electric guitars," *IEEE Transactions on Magnetics*, vol. 43, no. 9, pp. 3573–3578, 2007.

[108] N. G. Horton and T. R. Moore, "Modeling the magnetic pickup of an electric guitar," *American journal of physics*, vol. 77, no. 2, pp. 144–150, 2009.

[109] L. Guadagnin, B. Lihoreau, P. Lotton, and E. Brasseur, "Analytical modeling and experimental characterization of a magnetic pickup for electric guitar," *Journal of the Audio Engineering Society*, vol. 65, no. 9, pp. 711–721, 2017.

[110] M. Mustonen, D. Kartofelev, A. Stulov, and V. Välimäki, "Experimental verification of pickup nonlinearity," in *Proceedings International Symposium on Musical Acoustics (ISMA 2014), Le Mans, France*, vol. 1, 2014.

[111] A. Novak, B. Lihoreau, E. Brasseur, P. Lotton, and L. Simon, "Guitar pickup: Measurement of its two-dimensional nonlinear function," *Journal of the Audio Engineering Society*, vol. 68, no. 3, pp. 184–192, 2020.

[112] A. S. Rao, "Alnico permanent magnets an overview," in *Proceedings of Electrical/Electronics Insulation Conference*, pp. 373–383, IEEE, 1993.

[113] L. Ferraris, F. Franchini, and E. Pošković, "Hybrid magnetic composite (hmc) materials for sensor applications," in *2016 IEEE Sensors Applications Symposium (SAS)*, pp. 1–6, IEEE, 2016.

[114] M. E. Orazem and B. Tribollet, "Electrochemical impedance spectroscopy," *New Jersey*, pp. 383–389, 2008.

[115] D. M. Huber and R. Runstein, *Modern recording techniques*. Routledge, 2013.

[116] U. Önen, *Ses kayıt ve Müzik Teknolojileri*. Çitlembik, 2008.

[117] D. Brosnac, *Guitar electronics for musicians*. Music Sales Amer, 1983.

[118] R. Denyer, I. Guillory, A. M. Crawford, and R. Fripp, *The guitar handbook*. Pan books, 1992.

[119] A. Novak, L. Guadagnin, B. Lihoreau, P. Lotton, E. Brasseur, and L. Simon, "Non-linear identification of an electric guitar pickup," in *Proceedings of the 19th International Conference on Digital Audio Effects (DAFx-16), Brno, Czech Republic*, pp. 5–9, 2016.

RightsLink

Electrochemical Impedance Spectroscopy (EIS) and non-linear harmonic analysis (NHA) of Li-SOCl 2 /SO 2 Cl 2 batteries

Author: Gökberk Katırcı,Fazlı Eren Civan,Sunghoon Jung,Chae Bong Lee,Burak Ülgüt

Publication: Electrochimica Acta

Publisher: Elsevier

Date: 20 March 2024

© 2024 Elsevier Ltd. All rights reserved.

Journal Author Rights

Please note that, as the author of this Elsevier article, you retain the right to include it in a thesis or dissertation, provided it is not published commercially. Permission is not required, but please ensure that you reference the journal as the original source. For more information on this and on your other retained rights, please visit: https://www.elsevier.com/about/our-business/policies/copyright#Author-rights

BACK CLOSE WINDOW

© 2024 Copyright - All Rights Reserved | Copyright Clearance Center, Inc. | Privacy statement | Data Security and Privacy | For California Residents | Terms and ConditionsComments? We would like to hear from you. E-mail us at customercare@copyright.com

CCC Marketplace

Order Confirmation

Thank you, your order has been placed. An email confirmation has been sent to you. Your order license details and printable licenses will be available within 24 hours. Please access Manage Account for final order details.

This is not an invoice. Please go to manage account to access your order history and invoices.

CUSTOMER INFORMATION

Payment by invoice: You can cancel your order until the invoice is generated by contacting customer service.

Billing Address

Gökberk Katırcı
Bilkent University Chemistry DEpartment
Ankara
Turkey

+90 (505)8312511
gokberk.katirci@gmail.com

Customer Location

Gökberk Katırcı
Bilkent University Chemistry DEpartment
Ankara
Turkey

PO Number (optional)

N/A

Payment options

Invoice

PENDING ORDER CONFIRMATION

Confirmation Number: Pending

Order Date: 11-May-2024

1. Journal of the Electrochemical Society

0.00 USD

Order License ID	Pending	Publisher	IOP Publishing
ISSN	1945-7111	Portion	Chart/graph/table/figure
Type of Use	Republish in a thesis/ dissertation		

LICENSED CONTENT

Publication Title	Journal of the Electrochemical Society	Country	United States of America
Author/Editor	Electrochemical Society.	Rightsholder	IOP Publishing, Ltd
Date	01/01/1948	Publication Type	e-Journal
Language	English	URL	http://www.scitation.org/JES

REQUEST DETAILS

Portion Type	Chart/graph/table/figure	Distribution	Other territories and/or countries
Number of Charts / Graphs / Tables / Figures Requested	4	Enter Territories/Countries	Turkey
Format (select all that apply)	Print, Electronic	Translation	Original language of publication
Who Will Republish the Content?	Author of requested content	Copies for the Disabled?	No
Duration of Use	Life of current edition	Minor Editing Privileges?	No
Lifetime Unit Quantity	Up to 499	Incidental Promotional Use?	No
Rights Requested	Main product	Currency	USD

NEW WORK DETAILS

Title	TEMPERATURE-DEPENDENT ELECTROCHEMICAL IMPEDANCE SPECTROSCOPY (EIS) OF LITHIUM THIONYL CHLORIDE AND LI-ION BATTERIES	Institution Name	Bilkent University
		Expected Presentation Date	2024-05-22
Instructor Name	Burak Ülgüt		

ADDITIONAL DETAILS

Order Reference Number	N/A	The Requesting Person / Organization to Appear on the License	Gökberk Katırcı/Bilkent University

REQUESTED CONTENT DETAILS

Title, Description or Numeric Reference of the Portion(s)	Journal of the Electrochemical Society	Title of the Article / Chapter the Portion Is From	Methods—Unexpected Effects in Galvanostatic EIS of Randles' Cells: Initial Transients and Harmonics Generated
Editor of Portion(s)	N/A	Author of Portion(s)	Electrochemical Society.
Volume / Edition	169	Issue, if Republishing an Article From a Serial	N/A
Page or Page Range of Portion	030527	Publication Date of Portion	2022-03-17

RIGHTSHOLDER TERMS AND CONDITIONS

These special terms and conditions are in addition to the standard terms and conditions for CCC's Republication Service and, together with those standard terms and conditions, govern the use of the Works. As the User you will make all reasonable efforts to contact the author(s) of the article which the Work is to be reused from, to seek consent for your intended use. Contacting one author who is acting expressly as authorised agent for their co-author(s) is acceptable. User will reproduce the following wording prominently alongside the Work: the source of the Work, including author, article title, title of journal, volume number, issue number (if relevant), page range (or first page if this is the only information available) and date of first publication; and a link back to the article (via DOI); and if practicable, and IN ALL CASES for new works published under any of the Creative Commons licences, the words "© The Electrochemical Society. Reproduced by permission of IOP Publishing Ltd. All rights reserved" Without the express permission of the author(s) and the Rightsholder of the article from which the Work is to be reused, User shall not use it in any way which, in the opinion of IOP Publishing Ltd, could: (i) distort or alter the author(s)' original intention(s) and meaning; (ii) be prejudicial to the honour or reputation of the author(s); and/or (iii) imply endorsement by the author(s) and/or the Rightsholder and/or IOP Publishing Ltd. This licence does not apply to any article which is credited to another source and which does not have the copyright line '© The Electrochemical Society'. User must check the copyright line of the article from which the Work is to be reused to check that the Electrochemical Society and IOP Publishing Ltd has all the necessary rights to be able to grant permission. User is solely responsible for identifying and obtaining separate licences and permissions from the copyright owner for reuse of any such third party material/figures which the Rightsholder is not the copyright owner of. The Rightsholder shall not reimburse any fees which User pays for a republication license for such third party content. This licence does not apply to any material/figure which is credited to another source in the Rightsholder's publication or has been obtained from a third party. User must check the Version of Record of the article from which the Work is to be reused, to check whether any of the material in the Work is third party material. Third party citations and/or copyright notices and/or permissions statements may not be included in any other version of the article from which the Work is to be reused and so cannot be relied upon by the User. User is solely responsible for identifying and obtaining separate licences and permissions from the copyright owner for reuse of any such third party material/figures where the Rightsholder is not the copyright owner. The Rightsholder shall not reimburse any fees which User pays for a republication license for such third party content. User and CCC acknowledge that IOP Publishing Ltd and/or the Rightsholder may, from time to time, make changes or additions to these special terms and conditions without express notification, provided that these shall not apply to permissions already secured and paid for by User prior to such change or addition. User acknowledges that the Rightsholder and IOP Publishing Ltd (which includes companies within its group and third parties for whom it publishes its titles) may make use of personal data collected through the service in the course of their business. If User is the author of the Work, User may automatically have the right to reuse it under the rights granted back when User transferred the copyright in the article to the Rightsholder. User should check the copyright form and the relevant author rights policy to check whether permission is required. If User is the author of the Work and does require permission for proposed reuse of the Work, User should select 'Author of requested content' as the Requestor Type. The Rightsholder shall not reimburse any fees which User pays for a republication license. If User is the author of the article which User wishes to reuse in User's thesis or dissertation, the republication licence covers the right to include the Version of Record of the article, provided it is not then published commercially. User must include citation details and, for online use, a link to the Version of Record of the article on the IOPscience website. User may need to obtain separate permission for any third party content included within the article. User must check this with the copyright owner of such third party content. User may not include the article in a thesis or dissertation which is published by ProQuest. Any other commercial use of User's thesis or dissertation containing the article would also need to be expressly notified in writing to the Rightsholder at the time of request and would require separate written permission from the Rightsholder. As well as CCC, the Rightsholder and IOP Publishing Ltd shall have the right to bring any legal action that they deem necessary to enforce their rights should they consider that the Work infringes those rights in any way. For content reuse requests that qualify for permission under the STM Permissions Guidelines, which may be updated from time to time, the STM Permissions Guidelines supplement the terms and conditions contained in this license.
If you are producing a new book or article to be published by another STM Signatory publisher, please choose "Reuse in a book under STM Guidelines" or "Reuse in a journal under STM Guidelines." You can consult the STM Guidelines website to see whether your new publisher is a signatory to the STM Permissions Guidelines.

Total Items: 1 **Total Due: 0.00 USD**

Accepted: Marketplace Permissions General Terms and Conditions and any applicable Publisher Terms and Conditions